Institut für Festkörperphysik

FRIEDRICH-SCHILLER-UNIVERSITÄT JENA

Tieftemperaturphysik Prof. Dr. P. Seidel Prof. Dr. F. Schmidl	**Angewandte Physik /Festkörperphysik** Prof. Dr. T. Fritz
Experimentelle Festkörperphysik Prof. Dr. C. Ronning	**Ionenstrahlphysik** Prof. Dr. E. Wendler
Photovoltaik Prof. Dr. C. Ronning Dr. U. Reislöhner	**Laborastrophysik und Clusterphysik** Dr. C. Jäger

Annual Report 2014

Institut für Festkörperphysik

Friedrich-Schiller-Universität Jena

Annual Report 2014

Editor: Prof. Dr. Torsten Fritz

Institut für Festkörperphysik
Friedrich-Schiller-Universität Jena
Helmholtzweg 3/5
D-07743 JENA

home page: http://www.ifk.uni-jena.de/

Prof. Dr. Torsten Fritz (director)	Tel.:	+49 (0) 3641 / 947400, 947411
	Fax:	+49 (0) 3641 / 947412
	e-mail:	torsten.fritz@uni-jena.de
	home page:	http://www.organics.uni-jena.de
Prof. Dr. Carsten Ronning	Tel.:	+49 (0) 3641 / 947300, 947301
	Fax:	+49 (0) 3641 / 947302
	e-mail:	carsten.ronning@uni-jena.de
	home page:	http://www.nano.uni-jena.de
		http://www.photovoltaik.uni-jena.de
Prof. Dr. Paul Seidel	Tel.:	+49 (0) 3641 / 947410, 947411
	Fax:	+49 (0) 3641 / 947412
	e-mail:	paul.seidel@uni-jena.de
	home page:	http://www.tieftemperaturphysik.uni-jena.de/
Prof. Dr. Frank Schmidl	Tel.:	+49 (0) 3641 / 947429, 947411
	Fax:	+49 (0) 3641 / 947412
	e-mail:	frank.schmidl@uni-jena.de
	home page:	http://www.tieftemperaturphysik.uni-jena.de/
Prof. Dr. Elke Wendler	Tel.:	+49 (0) 3641 / 947333
	Fax:	+49 (0) 3641 / 947302
	e-mail:	elke.wendler@uni-jena.de
	home page:	http://www.ionenstrahlphysik.uni-jena.de/
Dr. Cornelia Jäger	Tel.:	+49 (0) 3641 / 947354
	Fax:	+49 (0) 3641 / 947308
	e-mail:	cornelia.jaeger@uni-jena.de
	home page:	http://www.astrolab.uni-jena.de/

Preface

I am pleased to introduce this Annual Report because 2014 was a rather successful year for the Institute of Solid State Physics at the Friedrich-Schiller-University Jena. Among other highlights, our colleague Dr. E. Wendler was bestowed the title *apl.-Prof.* which we celebrated in a special seminar on April 25.

Without doubt, knowledge creation, being the defining role of any great universities since times of Alexander Humboldt, remains the central mission of 21st century research universities. But the way in which we conduct education and research undergoes currently major changes which do not render it always easy to cope with. Especially the declining of the number of talented (sic) students of physics and the generally inclining social acceptance of natural sciences presents some major challenge for the entire faculty. So I'm especially pleased to announce that we succeeded in 2014 in establishing a special children's lab in our institute, which was finally opened in February 2015.

I would also like to thank all colleagues and coworkers sincerely for the huge efforts they spent again in ensuring a very high quality of academic education. I feel it might be safe to state that our institute contributes to it in an outstanding manner, despite our rather limited human resources.

We like to take this annual report 2014 as an opportunity to thank a lot of people and organizations for their manifold support for our research. We also like to thank all our colleagues at other universities and institutes all over the world which were or still are collaborating with us, but where the collaborative work has not been presented in the research articles of this report.

Last but not least, we are very grateful for the work of our very motivated secretaries, technicians, and the people in the mechanical and electrical workshops. All of them have contributed to our research in an outstanding way and, thus, to this report.

Let's altogether keep up the good work in 2015 and beyond!

Prof. Dr. Torsten Fritz
(director)

Content

1. Scientific Groups of the Institute (Portraits)

Applied Physics / Solid State Physics

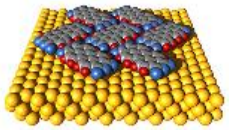

Prof. Dr. Torsten Fritz

- Preparation of highly ordered thin films of organic molecules by UHV-deposition (OMBE)
- Chemical vapor deposition and characterization of carbon nanotubes
- Epitaxial graphene
- Organic-organic heteroepitaxy
- K-doped organic superconductors
- Organic-inorganic hybrid solar cells
- *In situ* optical spectroscopy (DRS and PL) on ultrathin molecular layers
- Analyses of surfaces, layers and nanostructures using AES, XPS, LEED, RHEED, XPD, STM, AFM, and SEM

The group ***Applied Physics / Solid State Physics*** at the Institute of Solid State Physics is engaged in the research on nanostructures, solid surfaces and thin films of both organic and inorganic semiconductor materials.

Our main research interest lays in the discovery of structure-property-relations of structurally well defined ultrathin epitaxial layers, organic quantum wells, K-doped organic super conductors, and carbon nanotubes. The main target of our research is the development of basic principles for the use of nano materials in prospective devices.

For the analyses of the chemical composition and bonding at surfaces and in thin films we use surface analysis methods like photoelectron spectroscopy (XPS, UPS) and Auger electron spectroscopy (AES). The crystalline structure can be determined by electron diffraction (LEED, RHEED, XPD, and electron channeling). Scanning tunneling microscopy (STM), atomic force microscopy (AFM) and scanning electron microscopy (SEM) are used for high-resolution imaging of nanostructures and surfaces.

Our *in situ* optical spectroscopy, namely differential reflectance spectroscopy (DRS) is used to study organic (sub-)monolayers and heterostructures in terms of absorption spectroscopy to analyse the optical interaction between either the molecules itself, organic adsorbates and inorganic substrates, or molecules and dopants.

Experimental Physics / Solid State Physics

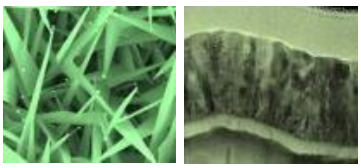

Prof. Dr. Carsten Ronning

- Synthesis, doping and functionization of semiconductor nanowires
- Photovoltaics
- Atomic structure and band-gap of complex semiconductors
- Modification and functionaization of phase change materials
- Growth and functionalization of diamond-like materials
- Semiconductor physics: doping using ion beams

Recent work of the research group ***Experimental Physics / Solid State Physics*** in the field of semiconductor nanowires focuses both on the growth of desired nanostructures as well as on the modification of semiconductor nanowires using ion beams for the use as photonic and electronic devices. This includes the realization of light-emitting diodes, single photon emitters, sensors for bio and chemical applications, and the observation of laser oscillations within single nanowires. Another scientific area of the group is the investigation and manipulation of phase change materials and devices using ion beams. Furthermore, the group works on the investigation of hard/soft interfaces in terms of biocompatibility. Here, the accelerator systems Mr. JIM Stringer and LEILA are used for the growth of diamond-like materials as well as for nanostructuring of surfaces (ripples).

The research on photovoltaics is mainly directed to the synthesis and analysis of $Cu(In,Ga)(Se,S)_2$ based thin film solar cells (CIGS). The research aims at a better understanding of the materials science of the CIGS chalcopyrite semiconductors and the improvement of existing cell concepts. To this end, a complete baseline on a form factor of 10x10 cm^2 is available at the institute. Most important, we developed a high expertise in a comprehensive characterization of the structural, electrical and optical properties of CIGS solar cells. Besides standard tools, such as XRD, PL, CL, IV, we also use sophisticated synchrotron based characterization methods (EXAFS, XRF) or advanced electrical instruments (TAS, DLTS, etc.).

Low Temperature Physics

Prof. Dr. Paul Seidel

- Superconductivity within thin layers and layer systems
- Josephson effects, proximity effect, and tunnel effects in superconducting devices
- DC-SQUID's and their application in measurements, e.g. CCC, MRX
- cryogenic measurements of mechanical quality factor and optical properties
- Dynamics of superconducting Josephson arrays
- cryogenic engineering (cryocoolers, cryogenic storage, cryostates)

The ***Low Temperature Physics*** group works on the following fields:

- preparation, characterization, modelling and application of Josephson junctions and SQUIDs (high precision and magneto-relaxation measurements with LTS SQUIDs, development of HTS SQUIDs, intrinsic Josephson junctions and Josephson junctions with iron based superconductors)
- low temperature physics and cryogenic engineering (development of new kinds of pulse tube cryocoolers, low lost cryostats and cryogenic storage, cryogenic current comparator CCC for particle accelerator beam analysis)
- experimental work within the SFB/TR7 on cryogenic measurements of the Q-factor and of optical properties of components for future gravitational wave detectors like the Einstein Telescope
- thin film technologies for insulators and other materials
- alternative preparation and properties of crystalline gold nanoclusters

The research is carried out in cooperation with other research groups in Thuringia (TU Ilmenau, Leibniz Institute IPHT Jena, SUPRACON Jena, Innovent e.V. Jena, Helmholtz Institute Jena). Within common activities the group works together with the Gesellschaft für Schwerionenforschung (GSI) Darmstadt, DESY Hamburg, MPI Heidelberg, IFW Dresden and the DLR Bremen.

Several research activities exist with industrial partners e.g. with the TransMIT center for adaptive cryotechniques Gießen. A long tradition of cooperation with the the Universities of Moscow (Russia), Bratislava (Slovak Republic), Kharkov and Donetsk (Ukraine), Glasgow (U.K.), Poznan (Poland), Padua, Torino and Florence (Italy), Twente (Netherlands) and the Universities of Osaka, Tokyo and Nagoya (Japan) is also remarkable.

Ion Beam Physics

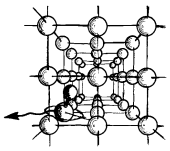

Prof. Dr. Elke Wendler

- Modification of solids by ion implantation and
- succeeding processes
- Ion beam analysis (RBS, PIXE, ERD, NRA)
- Ion beam synthesis of buried nanostructures
- Investigation of the effect of high electronic excitation on structural
- modification of crystalline and amorphous semiconductors

The ***Ion Beam Physics*** group deals with modification of solids and synthesis of buried nanostructures using ion beams and combined secondary processes. The studies cover fundamental processes of ion-beam induced structural modification in semiconductors and insulators being relevant for future electronic, optoelectronic and photonic device technologies.

Silver nanoclusters were successfully formed in LiNbO3 by ion beam synthesis and subsequent annealing and absorption due to plasmon resonance was experimentally proven. To optimise patterning of LiNbO3 by ion beam enhanced etching of this material, damage formation by nuclear and electronic energy deposition of the implanted ions continued to be investigated in collaboration with the Institute of Applied Physics. Here especially the built-up of strain was studied and related to the detected amount of structural damage. Primary effects of damage formation were also studied in crystalline semiconductors. For SiC this work was done in collaboration with the University of Pretoria in South Africa and it could be shown that at elevated temperatures the volume introduced by the implanted ions is decisive for the occurring processes. In collaboration with the University Minsk in Belarus we continued our work on ion beam synthesis of III-V compound nanoclusters in silicon.

Beside these activities on materials modification utilizing ion beams with conventional energies (several 10 keV to several MeV), the effect of high electronic excitation due to swift heavy ion irradiation (several 100 MeV) on plastic deformation and on the formation of voids and porous structures in amorphous Ge were studied in collaboration with the Australian National University Canberra in Australia.

Laboratory Astrophysics / Cluster Physics

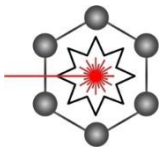

Dr. Cornelia Jäger

- Electronic spectroscopy of neutral and ionized polycyclic aromatic hydrocarbons (PAHs) in supersonic jets and cryogenic matrices
- Study of astrochemically relevant reactions in liquid helium nanodroplets
- Condensation and growth of cosmic dust at low temperature and pressure
- Gas-phase condensation processes of cosmic dust nanoparticles at high temperatures in circumstellar environments
- Study of chemical and structural processing of cosmic dust grains and astrophysically relevant molecules by UV photons and ion bombardment
- Chemical reactions and processing at the interface between dust and molecular ices

The ***Laboratory Astrophysics and Cluster Physics Group*** at the Institute of Solid State Physics results from a cooperation between the Max Planck Institute for Astronomy, Heidelberg, and the Friedrich Schiller University, Jena. Inaugurated in February 2003, it is now conducted by Prof. Dr. Thomas Henning and Dr. Corne-lia Jäger.

The research of our group is devoted to fundamental astrophysical questions that can be answered by laboratory experiments, with particular emphasis on spectroscopy. The electromagnetic radiation reaching us from stellar objects is modified in a characteristic manner by interstellar molecules and dust particles. Many of these "fingerprints" are still far from being understood. In order to determine the species causing the modification of the electromagnetic signals detected by telescopes and satellites, and to understand global cosmic processes, comprehensive laboratory studies are urgently needed.

In our laboratory, we study the condensation, processing, and spectral properties of carbonaceous and siliceous dust grains and astrophysically relevant molecules that may play a role as progenitors of grain formation. Laboratory astrophysics is an interdisciplinary field whose research profits from sophisticated experimental facilities. We are able to simulate astrophysically relevant processes such as gas-phase condensation of grains and molecules by laser-induced pyrolysis of hydrocarbons or laser ablation of solids in the laboratory. Interesting molecules, clusters, and nanoparticles are prepared in vacuum chambers under conditions coming close to those in interstellar or circumstellar environments (low pressures and definite temperature ranges from around 10 K up to more than 2000 K). Sophisticated analytical tools comprising optical and IR spectroscopy, mass spectrometry, chromatography, and electron microscopy help us to characterise the composition and structure of the laboratory analogs of dust and complex molecules.

2. Current Research Projects

2.1 Research Areas and Important Results

The research group of **Prof. Dr. Torsten Fritz** is engaged in the research on nanostructures, surfaces of solids, and thin films of both organic and inorganic semiconductor materials.

Our main research interest lays in the discovery of structure-property-relations of structurally well-defined ultrathin epitaxial layers, organic quantum wells, K-doped organic super conductors, and carbon nanotubes. The main target of our research is the development of basic principles for the use of nano materials in prospective devices. For the analyses of the chemical composition and bonding at surfaces and in thin films we use surface analysis methods like photoelectron spectroscopy (XPS, UPS) and Auger electron spectroscopy (AES). The crystalline structure can be determined by electron diffraction (LEED, RHEED, XPD, and electron channeling). Scanning tunneling microscopy (STM) and atomic force microscopy (AFM) at ultra-low temperatures (T = 1.1 K) are used for high-resolution imaging of nanostructures and surfaces.

Our *in situ* optical spectroscopy, namely differential reflectance spectroscopy (DRS) is used to study organic (sub-)monolayers and heterostructures in terms of absorption spectroscopy to analyze the optical interaction between either the molecules itself, organic adsorbates and inorganic substrates, or molecules and dopants.

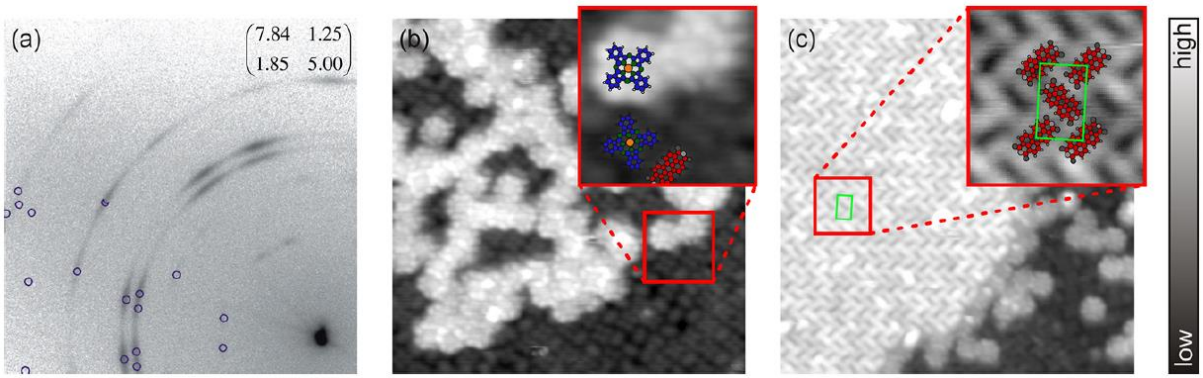

Figure 1: (a) SPA-LEED pattern of 0.70 ML PTCDA on CuPc/Ag(111) recorded at room temperature (E_{kin} = 27.2 eV). In the lower left part of the diffraction image, simulated diffraction spots are shown as blue circles. The corresponding superstructure matrix is also given in the upper right corner. Panels (b) and (c) show LT-STM images of 0.6 ML PTCDA deposited onto 0.9 ML CuPc on Ag(111), V_s = 1.5 V, I_t = 1.5 pA. (b) 16.5 × 16.5 nm^2 scan with CuPc molecules floating on top of the first layer composed of CuPc with PTCDA inclusions in a disordered arrangement. (c) 20.6 × 20.6 nm^2 scan with CuPc and PTCDA molecules in the second layer, the latter forming the typical herringbone pattern. Both insets depict selected areas measuring 3.2 × 3.2 nm^2 superimposed by structural models of the molecules. PTCDA appears dark in the center with bright lobes on either side of the aromatic framework's long axis. The green rectangle denotes the PTCDA unit cell derived from LEED.

Important results obtained in 2014:

- Discovery of the molecular exchange in a heteromolecular PTCDA/CuPc bilayer film on Ag(111)
- Elucidation of the complex polymorphism and thermodynamic behavior of naphthalene on Cu(111)
- Implementation of a new STM technique: the Scanning Tunneling Hydrogen Microscopy (STHM)
- Direct imaging of dopant atoms in a potassium doped organic thin film
- Detailed optical investigation of ultrathin DBP films on a variety of substrates

The focus areas of the research of the solid state physics group of **Prof. Dr. Carsten Ronning** are:

- Synthesis, doping, characterization, and functionalization of semiconductor nanowires
- Structural analysis of complex semiconductors in relation to their electronic properties
- Modification and characterization of phase change materials
- Synthesis of diamond-like materials for bio-medical applications
- Semiconductor physics: optical, electrical, and magnetic doping via ion implantation
- Synthesis and characterization of CIGS and CdTe thin film solar cells
- Ion beam synthesis of nanoclusters

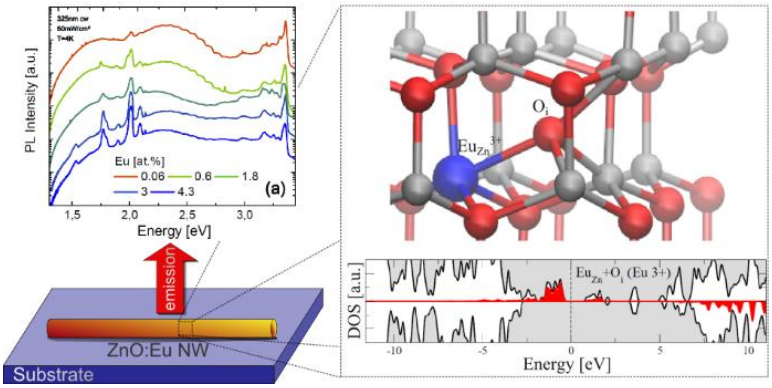

Figure 2: Successful doping and excellent optical activation of Eu^{3+} ions in ZnO nanowires were achieved by ion implantation. We identified and assigned the origin of the intra-4f luminescence of Eu^{3+} ions in ZnO by first-principles calculations to Eu–Oi complexes, which are formed during the non-equilibrium ion implantation process and subsequent annealing at 700 °C in air. Our targeted defect engineering resulted in intense intrashell luminescence of single ZnO:Eu nanowires dominating the photoluminescence spectrum even at room temperature. The high intensity enabled us to study the luminescence of single ZnO nanowires in detail, their behavior as a function of excitation power, waveguiding properties, and the decay time of the transition.

Important results obtained in 2014:

- Development of ultrafast plasmonic nanowire lasers near the surface plasmon frequency
- Observation of intense intra-shell luminescence of Eu-doped single ZnO nanowires at room Temperature by ion implantation created Eu-O_i complexes
- Realization of phonon-assisted lasing in ZnO microwires at room temperature
- Observation of the amphoteric nature of Sn in CdS nanowires

- Realization of local ion irradiation-induced resistive threshold and memory switching in Nb_2O_5/NbO_x films
- Investigation of the local and global electronic properties of chalcopyrite alloys by X-ray absorption spectroscopy and ab initio calculations

The **Low Temperature Physics** group (Prof. Dr. Paul Seidel) focusses on the following topics:

- Modelling, fabrication, characterization and application of Josephson junctions and superconducting quantum interference devices (SQUIDs) including novel superconductors such as pnictides
- Cryogenic engineering and low temperature physics (e.g. design and optimization of cryostats)
- Experimental aspects of gravitational wave detection including the study of mechanical losses in crystalline and amorphous materials, modelling of thermal noise processes in precision instrumentation, study of thermo-mechanical and thermo-optical properties of matter at low temperatures
- Instrumentation for particle accelerators (e.g. cryogenic current comparators)
- Thin film physics and their applications in optical and electronic components

Important results obtained in 2014:

- Modelling of a new noise process occurring in silicon if used as transmissive optical component based on the correlation between refractive index and density of free carriers
- Different kinds of Josephson junctions with one or two pnictide electrodes in thin film technology as well as using a pnictide single crystal for basis electrode
- Modification of structural and superconducting properties of thin high-T_c films with selforganised grown Au-nanoparticles

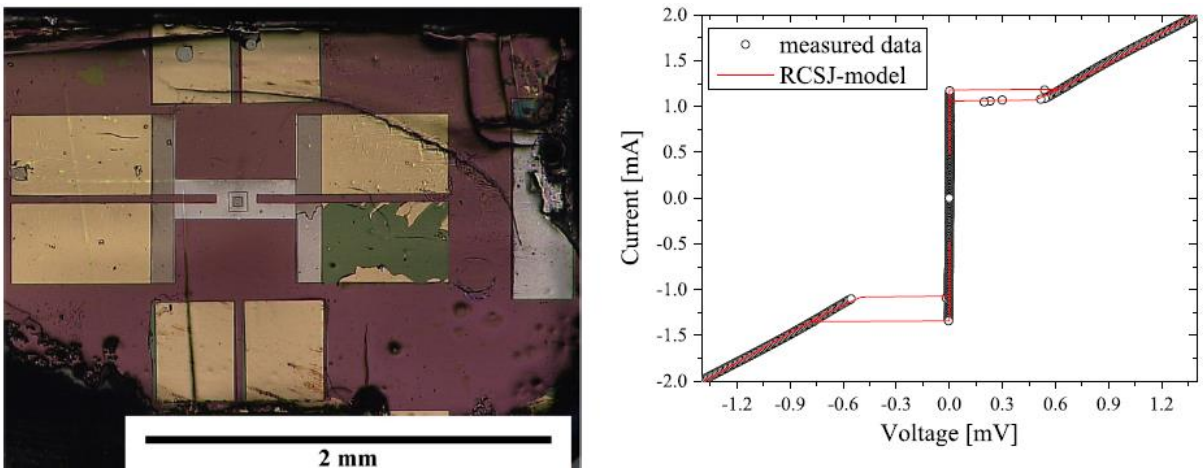

Figure 3: Left: Optical micrograph of a Josephson junction on a pnictide single crystal with a lead counterelectrode and an Au/TiOx barrier. Right: Measured I–V characteristic of such a Josephson junction at T = 4.2 K compared to a fit within the RCSJ model demonstrating a remarkable high I_cR_n product [Superconductor Science and Technology 27 (2014) 085003].

The **Ion Beam Physics group** of Prof. Dr. Elke Wendler applies ion beams for analyzing and modifying solids. The main fields of work are:

- Ion-beam induced damage formation in covalent-ionic crystals
- Formation of nano-crystals by high-fluence ion implantation and annealing
- Combination of various ion-beam techniques for compositional analysis of solids and thin films
- Defect analysis in covalent-ionic crystals by ion channeling
- Investigation of relations between structure and physical properties in defective crystals

Important results obtained in 2014:

- Prove of validity of empirical formula of damage formation in ion implanted III-V compounds for ion implanted SiC
- Evidence of crucial role of atomic species for defect formation in ion implanted ZnO
- Formation of GaN nanocrystals in SiO_2
- Simultaneous profiling of fluorine and heavy elements in doped SiO_2 glasses by ion beam analysis

The working group ***Laboratory Astrophysics and Cluster Physics*** (Dr. Cornelia Jäger and Prof. Dr. Thomas Henning, MPIA Heidelberg) dealt with the following priority projects in the year 2014:

- High-temperature, gas-phase condensation experiments of carbonaceous and siliceous cosmic dust analogs and their morphological, structural, and spectral characterization from the VUV to the IR spectral range
- Experimental studies on astrophysically relevant processing of carbonaceous solids and silicates by UV photons, ion bombardment, and X-ray irradiation
- Laboratory experiments to study the formation of astrophysically important molecules such as H_2, CO, und CO_2 on dust grain surfaces
- Stability studies of polycyclic aromatic hydrocarbons (PAHs) under astrophysical conditions
- Chemical reactions of atoms and molecules in He clusters at low temperatures
- Experimental studies on the condensation and growth of astrophysically relevant dust particles at low temperature and pressure in the interstellar medium and identification of the molecular precursors for the low-temperature formation and growth of cosmic dust particles in the ISM by matrix-isolation spectroscopy
- Interaction of fullerenes with PAHs

Outstanding results 2014:

- We have experimentally demonstrated that complex magnesium iron silicates can be efficiently formed at temperatures prevailing in the dense interstellar medium. This has been shown by in situ IR spectroscopy of the formed silicates at temperatures around 10 K. The formed silicates show a good agreement with the spectral signature of interstellar

silicates in the IR range. In addition, the formation of carbonaceous solids at temperatures of around 10 K without an energy barrier has also been confirmed. The experimental results have a strong impact on the understanding of dust formation and growth processes in dense molecular clouds.

- The reaction of atomic carbon with benzene molecules has been investigated in liquid helium droplets at ultra-low temperature. The reaction between the two species was found to have no barrier in the entrance channel. Such barrierless reaction between benzene molecules and atomic carbon, which belongs to the four most abundant species in the ISM, is of great interest for the discussion of the stability and formation of PAH molecules in the ISM.

2.2 Third Party Grants

DFG projects

Dotierte aromatische Dünnfilme mit supraleitenden Eigenschaften
(FO 770/2-1)
Time span: 09/14 – 08/17

Optische Spektroskopie an ultradünnen Molekülschichten
(FR 875/9-3)
Time span: 02/12 – 02/15

Großgeräteantrag UHV-Analysesystem für XPS/UPS/AES
(INST 275/267-1)
Time span: 06/12 – 05/14

Formation and shaping of magnetic nanoclusters in oxides, using ion implantation
Time span: 03/11 – 02/15

Wiring quantum dots – phase separation inducing new functionality
Time span: 08/11 – 07/14

Dynamics and Interactions of Semiconductor Nanowires for Optoelectronics
Time span: 03/12 – 06/15

Teilprojekt P4: Light-matter interaction in optically doped nanowire LEDs and nano lasers
Time span: 03/12 – 11/15

Gütemessungen bei kryogenen Temperaturen
Project C4 within the Collaborative Research Center SFB/TR7
„Gravitationswellenastronomie“
Time span: 01/03 – 12/14

Optische Eigenschaften siliziumbasierter Testmassen
Project C9 within the Collaborative Research Center SFB/TR 7
„Gravitationswellenastronomie“
Time span: 01/11 – 12/14

Josephson effects at iron pnicides - phase-sensivitve experiments
Time span: 10/13 – 09/16

Experimental and theoretical studies of charge transport in heterostructures based on two-band superconductors and/or ferromagnetic metals
Time span: 11/13 – 06/15

Experimental studies of the low-temperature condensation of cosmic dust in the interstellar medium
(HE 1935/26-1) (1. Tranche of the SPP 1378) (financial management by the MPIA)
Time span: 02/12 – 01/15

Experimental studies of the low-temperature condensation of cosmic dust in the interstellar medium
(JA 2107/2-2) (2. Tranche of the SPP 1378)
Time span: 10/14 – 09/17

Kohlenwasserstoff-Chemie bei ultratiefen Temperaturen in flüssigen Helium-Tröpfchen
(HU 474/22-3)
Time span: 05/12 – 05/15

BMBF-, BMU- and BMWi-projects

Spitzenforschung und Innovation in den Neuen Ländern – PhoNa: Photonische Nanomaterialien
Time span: 12/09 – 11/14

Verbundvorhaben: Grenzflächen und Defekte – Rechnerunterstützte Optimierung des Wirkungsgrades von CIGS Dünnschichtsolarzellen in der industriellen Umsetzung
Teilvorhaben: Ermittlung von Struktur-Eigenschaftsbeziehungen und ihre Beeinflussung durch Variation der Prozessparameter
Time span: 08/12 – 07/15

Neuartige Verbundmaterialien u. Fertigungstechnologien für Kryostate zur see- u. luftgestützten Rohstoff- und Umwelterkundung (MAKSEL)
Time span: 09/14 – 12/17

Microwave response of intrinsic Josephson junctions and SQUIDs (Heisenberg-Landau Programm)
Time span: 01/14 – 12/14

ET R&D – Networking and R&D for the Einstein Telescope (3rd common ASPERA call)
Time span: 03/13 – 02/16

Other projects

Nanoscale Interfaces for Organic Electronics (DAAD PaJaKo Project Japan, ID 56264880)
Time span: 01/13 – 12/15

Marie-Curie ITN network "Nanowiring" (EU Projekt)
Time span: 11/10 – 10/14

Virtuelles Institut „MEMRIOX" (HZDR Dresden-Rossendorf)
Memory Effects in Resistive Ion-beam Modified Oxides
Time span: 10/11 – 09/16

GaN Nanokristalle dotiert mit seltenen Erden (DAAD/PPP Griechenland)
Time span: 01/13 – 12/14

Switchable and tunable infrared devices by controlled manipulation of the insulator-to-metal transition in Vanadium dioxide (DAAD/PPP USA)
Time span: 01/14 – 12/15

Schwingungsdynamik in komplexen Verbindungshalbleitern (ProChance, FSU Jena)
Time span: 03/13 – 03/16

IRON-SEA - Establishing the basic science and technology for Iron-based superconducting electronics applications (EU Projekt)
Time span: 10/11 – 09/14

FP7-PEOPLE-IRSES Scientist Exchange Program „ELiTES"
Time span: 03/12 – 02/16

3. Publications, Invited Talks, and Theses

3.1 Publications in Scientific Journals

Molecular exchange in a heteromolecular PTCDA/CuPc bilayer film on Ag(111),
B. Stadtmüller, M. Gruenewald, J. Peuker, R. Forker, T. Fritz, and C. Kumpf,
J. Phys. Chem. C **118**, 28592 (2014).

The complex polymorphism and thermodynamic behavior of a seemingly simple system: naphthalene on Cu(111),
R. Forker, J. Peuker, M. Meissner, F. Sojka, T. Ueba, T. Yamada, H. S. Kato, T. Munakata, and T. Fritz,
Langmuir **30**, 14163 (2014).

Principal processes of organic-inorganic hybrid solar cells using the example of ZnPc with ZnO,
M. Kozlik, R. Forker, and T. Fritz,
Phys. Status Solidi A: Applications and Materials Science, *accepted* (2014).
DOI 10.1002/pssa.201431545.

Phonon-assisted lasing in ZnO microwires at room temperature
T. Michalsky, M. Wille, C. P. Dietrich, R. Röder, C. Ronning, R. Schmidt-Grund, M. Grundmann
Appl. Phys. Lett. **105**, 211106 (2014).

Structural order in single Co-implanted ZnO nanowires
M.H. Chu, G. Martínez-Criado, J. Segura-Ruiz, S. Geburt, C. Ronning
physica status solidi (a) **211**, 483 (2014).

Highly Efficient Visible-Light Driven Photocatalysts: A Case on Zinc Stannate Based Nanocrystal Assemblies
C.H. Liu, R. Röder, H. Chen, Z. Ren, Z. Zhang, C. Ronning, P.X. Gao
Journal of Materials Chemistry **A 2**, 4157 (2014).

Persistent Photoconductivity in ZnO Nanowires in different Atmospheres
D. Cammi, C. Ronning
Advances in Condensed Matter Physics **2014**, 184120 (2014).

Amphoteric Nature of Sn in CdS Nanowires
M. Zhang, M. Wille, R. Röder, S. Heedt, L. Huang, Z. Zhu, S, Geburt, D. Grützmacher, T. Schaepers, C. Ronning, J.G. Lu
Nano Letters **14**, 518 (2014).

Utilizing dynamic annealing during ion implantation: synthesis of silver nanoparticles in crystalline lithium niobate
S. Wolf, J. Rensberg, H. Stöcker, B. Abendroth, W. Wesch, C. Ronning
Nanotechnology **25**, 135611 (2014).

Defect studies on Ar-implanted ZnO thin films
F. Schmidt, S. Muller, R. Pickenhain, H. von Wenckstern, S. Geburt, C. Ronning, M. Grundmann
physica status solidi B **251**, 937 (2014).

Magnetoresistance in Mn ion-implanted GaAs:Zn nanowires
W. Paschoal Jr, S. Kumar, D. Jacobsson, A. Johannes, V. Jain, C. M. Canali, A. Pertsova, C. Ronning, K. A. Dick, L. Samuelson, H. Pettersson
Applied Physics Letters **104**, 153112 (2014).

Single step integration of ZnO nano- and microneedles in Si trenches by novel flame transport approach: Whispering gallery modes and photocatalytic properties
T. Reimer, I. Paulowicz, R. Röder, S. Kaps, O. Lupan, S. Chemnitz, W. Benecke, C. Ronning, R. Adelung, Y. K. Mishra
ACS Applied Materials & Interfaces **6**, 7806 (2014).

Enhanced sputtering and incorporation of Mn in implanted GaAs and ZnO nanowires
A. Johannes, S. Noack, W. Paschoal, S. Kumar, D. Jacobsson, K. Dick, H. Pettersson, L. Samuelson, G. Martines-Criado, M. Burghammer, C. Ronning
Journal of Physics D: Applied Physics **47**, 394003 (2014).

Functional ZnO/polymer core-shell nanowires fabricated by oxidative vapour deposition (oCVD)
J.-P. Richter, A. Dev, C. Ronning, J. Gutowski, T. Voss
Journal of Physics D: Applied Physics **47**, 394004 (2014).

Flash Sintering of Nanocrystalline Zinc Oxide and its Influence on Microstructure and Defect Formation
C. Schmerbauch, J. Gonzales-Julian, R. Röder, C. Ronning, O. Guillon
Journal of the American Ceramic Society **97**, 1728 (2014).

Deep-level emission in ZnO nanowires and bulk crystals: excitation-intensity dependence versus crystalline quality
D. Hou, T. Voss, C. Ronning, A. Menzel, M. Zacharias
Journal of Applied Physics **115**, 233516 (2014).

Nano-X-ray diffraction study of single Co-implanted ZnO nanowires
M.H. Chu, G. Martínez-Criado, J. Segura-Ruiz, S. Geburt, C. Ronning
physica status solidi (a) **211**, 2523 (2014).

Gate modulation of below-band-gap photoconductivity in ZnO Nanowire Field-Effect-Transistors
D. Cammi, R. Röder, C. Ronning
Journal of Physics D: Applied Physics **47**, 394014 (2014).

Polarization features of optically pumped CdS nanowire lasers
R. Röder, D. Ploss, A. Kriesch, R. Buschlinger, S. Geburt, U. Peschel, C. Ronning
Journal of Physics D: Applied Physics **47**, 394012 (2014).

Intense Intrashell Luminescence of Eu-Doped Single ZnO Nanowires at Room Temperature by Implantation Created Eu-O_i Complexes
S. Geburt, M. Lorke, A. L. da Rosa, T. Frauenheim, R. Röder, T. Voss, U. Kaiser, W. Heimbrodt, C. Ronning
Nano Letters **14**, 4523 (2014).

Structural properties of zinc oxide deposited using atmospheric pressure combustion chemical vapour deposition
I. Zunke, S. Wolf, A. Heft, S. Schimanski, B. Grünler, C. Ronning, P. Seidel
Thin Solid Films **565**, 45 (2014).

Improving the optical properties of self-catalyzed GaN microrods towards whispering gallery mode lasing
C. Tessarek, R. Röder, T. Michalsky, S. Geburt, H. Franke, R. Schmidt-Grund, M. Heilmann, B. Hoffmann, C. Ronning, M. Grundmann, S. Christiansen
ACS Photonics **1**, 990 (2014).

Ultrafast plasmonic nanowire lasers near the surface plasmon frequency
T.P.H. Sidiropoulos, R. Röder, S. Geburt, O. Hess, S.A. Maier, C. Ronning, R.F. Oulton
Nature Physics **10**, 870 (2014).

Temperature and bias-voltage dependence of atomic-layer-deposited HfO_2-based magnetic tunnel junctions
S. Fabretti, R. Zierold, K. Nielsch, C. Voigt, C. Ronning, P. Peretzki, M. Seibt, A. Thomas
Applied Physics Letters **105**, 132405 (2014).

Local ion irradiation-induced resistive threshold and memory switching in Nb_2O_5/NbO_x films
H. Wylezich, H. Mähne, J. Rensberg, C. Ronning, P. Zahn, S. Slesazeck, T. Mikolajick
ACS Applied Materials & Interfaces **6**, 17474 (2014).

Hot-Electron Injection in Au Nanorod-ZnO Nanowire Hybrid Device for Near-Infrared Photodetection
A. Pescaglini, A. Martín, D. Cammi, G. Juska, C. Ronning, E. Pelucchi, D. Iacopino
Nano Letters **14**, 6202 (2014).

High lateral resolution energy dispersive X-ray spectroscopy and cathodolumniescence on lamellae of CIGSe solar cells
S. Schönherr, A. Tille, P. Schöppe, M. Oertel, U. Reislöhner, C. Ronning
IEEE Photovoltaic Specialist Conference **1699** (2014).

Electron-Beam-Induced Current at Absorber Back Surfaces of $Cu(In,Ga)Se_2$ Thin-Film Solar Cells
J. Kavalakkatt, D. Abou-Ras, J. Haarstrich, C. Ronning, M. Nichterwitz, R. Caballero, T. Rissom, T. Unold, R. Scheer, H.W. Schock
Journal of Applied Physics **115**, 014504 (2014).

Local versus global electronic properties of chalcopyrite alloys: X-ray absorption spectroscopy and ab initio calculations
R. Sarmiento-Pérez, S. Botti, C. S. Schnohr, I. Lauermann, A. Rubio, B. Johnson
Journal of Applied Physics **116**, 093703 (2014).

Fast atom diffraction from a ß-Ga_2O_3(100) surface
M. Busch, E. Meyer, K. Irmscher, Z. Galazka, K. Gärtner, H. Winter
Applied Physics Letters **105**, 051603 (2014).

Crucial role of implanted atoms on dynamic defect annealing in ZnO
A. Yu. Azarov, E. Wendler, A. Yu. Kuznetsov, B. G. Svensson
Applied Physics Letters **104**, 052101 (2014).

Influence of radiation damage on xenon diffusion in silicon carbide
E. Friedland, K. Gärtner, T. T. Hlatshwayo, N. G. van der Berg, T. T. Thabethe
Nucl. Instr. Meth B **332**, 415 (2014).

Meyer-Neldel rule for Cu (I) diffusion in In2S3 layers
A. Juma, H. Wafula, E. Wendler, T. Dittrich
Journal of Applied Physics **115**, 053703 (2014).

Formation of inorganic nanocomposites by filling TiO2 nanopores with indium and antimony sulfide precursor aerosols
A. Juma, A. Azarpira, Ch.-H. Fischer, E. Wendler, T. Dittrich
Thin Solid Films **566**, 19 (2014).

Nano-porosity in GaSb induced by swift heavy iron irradiation
P. Kluth, J. Sullivan, W. Li, R. Weed, C.S. Schnohr, R. Guilian, L. Araujo, W. Lei, M. D. Rodriguez, B. Afra, T. Bierschenk, R. C. Ewing, M. C. Ridgway
Applied Physics Letters **104**, 023105 (2014).

Structural and Luminescent Properties of Sn-Doped SiO Layers
F. Komarov, L. Vlasukova, O. Milchanin, M. A. Makhavikou, I. Parkhomenko, E. Wendler, W. Wesch, A. Mudryi, G. A. Ismailova
Journal of Applied Spectroscopy **80**, 855 (2014).

Light Emitting Single-Crystalline Silicon Wafers Implanted with V and III Groups Ions
F. Komarov, L. Vlasukova, O. Milchanin, M. Greben, I. Parkhomenko, A. Mudryi, E. Wendler, P. Zukowski
Acta Physics Polonica **125**, 1288 (2014).

Near-surface recrystallization of the amorphous implanted layer of ion implanted 6H-SiC
R. J. Kuhudzai, N. G. van der Berg, J. B. Malherbe, T. T. Hlatshwayo, C. C. Theron, A. V. Buys, A. J. Botha, E. Wendler, W. Wesch
Nucl. Instr. Meth. B **332**, 251 (2014).

Ion-beam-induced thin film stress in lithium niobate
E. Schmidt, T. Steinbach, W. Wesch
Journal of Physics D: Applied Physics **47**, 265302 (2014).

Temperature-Dependent Second Shell Interference in the First Shell Analysis of Crystalline InP X-ray Absorption Spectroscopy Data
C. S. Schnohr, L. Araujo, M. C. Ridgway
Journal of the Physical Society of Japan **83**(9), 094602-1-6 (2014).

Composition-dependent nanostructure of Cu(In,Ga)Se2 powders and thin films
C. S. Schnohr, H. Kämmer, T. Steinbach, M. Gnauck, T. Rissom, C. A. Kaufmann, C. Stephan, S. Schorr
Thin Solid Films (2014).

X-Ray Absorption Spectroscopy of Semiconductors
C. S. Schnohr, M. C. Ridgway
ISBN: 978-3-662-44361-3.

Swift heavy ion irradiation of crystalline CdTe
T. Steinbach, T. Bierschenk, S. Milz, M. C. Ridgway, W. Wesch
Journal of Physics D: Applied Physics **47**, 065301 (2014).

Porous structure formation in ion irradiated germanium
T. Steinbach, W. Wesch
Nucl. Instr. Meth. B **319**, 112 (2014).

Threshold and criterion for ion track etching in SiO2 layers grown on Si
L. Vlasukova, F. Komarov, V. N. Yuvchenko, W. Wesch, E. Wendler, A. Yu. Didyk, V. A. Skuratov, S. B. Kislitsin
Vacuum **105**, 107 (2014).

Low-temperature damage formation in ion-implanted SiC and its correlation with primary energy depostion
E. Wendler, M. Schilling, L. Wendler
Vacuum **105**, 102 (2014).

Silicon mirror suspensions for gravitational wave detectors
A. V. Cumming, L. Cunningham, G. D. Hammond, K. Haughian, J. Hough, S. Kroker, R. Nawrodt, S. Rowan, C. Schwarz, A. A. van Veggel
Class. Quantum Grav. **31**, 025017 (2014).

Modifications of the Meissner screening profile in $YBa_2Cu_3O_{7-\delta}$ thin films by gold nanoparticles
E. Stilp, A. Suter, T. Prokscha, Z. Salman, E. Morenzoni, H. Keller, C. Katzer, F. Schmidl, M. Döbeli
Phys. Rev. B **89**, 020510(R) (2014).

Low temperature mechanical dissipation of an ion-beam sputtered silica film
I. W. Martin, R. Nawrodt, C. Craig, C. Schwarz, R. Bassiri, G. Harry, J. Hough, S. Penn, S. Reid, R. Robie, S. Rowan
Class. Quantum Grav. **31**, 035019 (2014).

Investigation of TiO x barriers for their use in hybrid Josephson and tunneling junctions based on pnictide thin films
S. Döring, M. Monecke, S. Schmidt, F. Schmidl, V. Tympel, J. Engelmann, F. Kurth, K. Iida, S. Haindl, I. Mönch, B. Holzapfel, and P. Seidel:
J. Appl. Phys. **115**, 083901 (2014).

The influence of external separate heating on the synchronization of Josephson junctions
A. Grib, P. Seidel
Phys. Status Solidi B **251**, 1040–1044 (2014).

The Resonant Interaction of Intrinsic Josephson Junctions with Standing Waves ***(invited paper)***
A. Grib, M. Mans, M. Büenfeld, J. Scherbel, F. Schmidl, H. Schneidewind, P. Seidel
IEEE Trans. Appl. Supercond. **24**, 1800205 (2014).

Evaluation of heat extraction through sapphire fibres for the GW observatory KAGRA
A. Khalaidovski, G. Hofmann, D. Chen, J. Komma, C. Schwarz, C. Tokoku, N. Kimura, T. Suzuki, A. Scheie, E. Majorana, R. Nawrodt, K. Yamamoto
Class. Quantum Grav. **31**, 105004 (2014).

Coherent emission of intrinsic Josephson junctions
A. Grib, P. Seidel
Journal of Physics: Conference Series **507**, 042038 (2014).

Bicrystalline Grain Boundary Junctions of Co-doped and P-doped Ba-122 Thin Films
S. Schmidt, S. Döring, F. Schmidl, F. Kurth, K. Iida, B. Holzapfel, T. Kawaguchi, Y. Mori, H. Ikuta, P. Seidel
Journal of Physics: Conference Series **507**, 012046 (2014).

Influence of the spreading resistance on the conductance spectrum of planar hybrid thin film SNS' junctions based on iron pnictides
S. Döring, S. Schmidt, S. Gottwals, .F Schmidl, V. Tympel, I. Mönch, F. Kurth, K. Iida, B. Holzapfel P. Seidel
Journal of Physics: Conference Series **507**, 012008 (2014).

Realization of arbitrary patterns in high temperature superconducting $YBa_2Cu_3O_{7-X}$ thin films
C. Katzer, C. Stahl, P. Michalowski, S. Treiber, M. Westerhausen, R. Diener, F. Schmidl, P. Seidel, G. Schütz, J. Albrecht
Journal of Physics: Conference Series **507**, 012024 (2014).

Grain boundary engineering with gold nanoparticles
F. Schmidl, C. Katzer, P. Michalowski, S. Koch, V. Tympel
Journal of Physics: Conference Series **507**, 042037 (2014).

The Einstein Telescope
S. Kroker, R. Nawrodt
IEEE Metrology for Aerospace (MetroAeroSpace), 288-292 (2014).

Fluctuation Dissipation at Work: Thermal Noise in Reflective Optical Coatings for GW Detectors
D. Heinert, G. Hofmann, R. Nawrodt
IEEE Metrology for Aerospace (MetroAeroSpace), 293-298 (2014).

Mechanical Loss Characterization at Cryogenic Temperature of a Tungsten Wire: an Automated Measurement System
D. Chen, P. Daponte, D. Grimaldi, G. Hofmann, J. Komma, F. Lamonaca, A. Nastro, R. Nawrodt, F. Picariello, G. Polimene, M. Riccio, C. Schwarz, K. Yamamoto
IEEE Metrology for Aerospace (MetroAeroSpace), 479-483 (2014).

Thermal noise of folding mirrors
D. Heinert, K. Craig, H. Grote, S. Hild, H. Lück, R. Nawrodt, D. A. Simakov, D. V. Vasilyev, S. P. Vyatchanin, H. Wittel
Phys. Rev. D **90**, 042001 (2014).

Measurement of the optical absorption of bulk silicon at cryogenic temperature and the implication for the Einstein Telescope
J. Degallaix, J. Komma, D. Forest, G. Hofmann, M. Granata, D. Heinert, C. Schwarz, R. Nawrodt, L. Pinard, C. Michel, R. Flaminio, G. Cagnoli
Class. Quantum Grav. **31** 185010 (2014).

Preparation of hybrid Josephson junctions on Co-doped Ba-122 single crystals
D. Reifert, N. Hasan, S. Döring, S. Schmidt, M. Monecke, M. Feltz, F. Schmidl, V. Tympel, W. Wisniewski, I. Mönch, T. Wolf, P. Seidel
Supercond. Sci. Technol. **27** 085003 (2014).

Transition from Coulomb blockade to resonant transmission regime in superconducting tunnel
junctions with W-doped Si barriers
V. Shaternik, A. Shapovalov, M. Belogolovskii, O. Suvorov, S. Döring, S. Schmidt, P. Seidel
Materials Research Express **1** 026001 (2014).

Hybrid Josephson Junctions with Iron-based and Conventional Superconductor Electrodes
S. Döring, S. Schmidt , D. Reifert , M. Feltz, M. Monecke, N. Hasan · V. Tympel , F. Schmidl, J. Engelmann, F. Kurth, K. Iida, I. Mönch, B. Holzapfel , P. Seidel
J. Supercond. Nov. Magn.

Phase dynamics of two parallel stacks of coupled Josephson junctions
Yu. M. Shukrinov, I. R. Rahmonov, A. Plecenik, P. Seidel, E. Il'ichev, W. Nawrocki
Supercond. Sci. Technol. **27** 124007 (9pp) (2014).

Ultra-low-temperature reactions of $C(^3P_0)$ atoms with benzene molecules in helium droplets,
S. A. Krasnokutski and F. Huisken,
J. Chem. Phys. **141**, 214306/1-214306/5 (2014).

A simple and clean source of low-energy atomic carbon,
S. A. Krasnokutski and F. Huisken,
Appl. Phys. Lett. **105**, 113506/1-113506/4 (2014).

A straightforward method for vacuum-ultraviolet flux measurements: The case of the hydrogen discharge lamp and implications for solid-phase actinometry,
D. Fulvio, A. C. Brieva, S. H. Cuylle, H. Linnartz, C. Jäger, and Th. Henning,
Appl. Phys. Lett. **105**, 014105/1-014105/4 (2014).

Reactivity of iron atoms at low temperature,
S. A. Krasnokutski and F. Huisken,
J. Phys. Chem. A **118**, 2612-2617 (2014).

Cosmic Dust VI,
H. Kimura, L. Kolokolova, A. Li, A. K. Inoue, and C. Jäger,
Planet. Space Sci. **100**, 1-5 (2014).

Cosmic dust formation at cryogenic temperatures, in: The Life Cycle of Dust in the Universe: Observations, Theory, and Laboratory Experiments,
G. Rouillé, S. A. Krasnokutski, M. Krebsz, C. Jäger, F. Huisken, and Th. Henning: edited by A. Andersen, M. Baes, H. Gomez, C. Kemper, and D. Watson, PoS (LCDU 2013).

Cold condensation of dust in the ISM,
G. Rouillé, C. Jäger, S. A. Krasnokutski, M. Krebsz, and Th. Henning,
Faraday Discuss. 168, 449-460 (2014).

Diffuse Banden im All,
F. Huisken and C. Jäger,
Physik Journal **13**, 29-34 (2014).

Formation of silicon oxide grains at low temperature,
S. A. Krasnokutski, G. Rouillé, C. Jäger, F. Huisken, S. Zhukovska, and Th. Henning,
Astrophys. J. **782**, 15/1-15/10 (2014).

The formation of molecular hydrogen on silicate dust analogs: The rotational distribution,
L. Gavilan, J. L. Lemaire, G. Vidali, T. Sabri, and C. Jaeger,
Astrophys. J. **781**, 79/1-79/13 (2014).

Interstellar silicate analogs for grain-surface reaction experiments: Gas-phase condensation and characterization of the silicate dust grains,
T. Sabri, L. Gavilan, C. Jäger, J. L. Lemaire, G. Vidali, H. Mutschke, F. Huisken, and Th. Henning, Astrophys. J. **780**, 180/1-180/8 (2014).

3.2 Invited Talks at Conferences and Colloquia

T. Fritz:

Epitaxial Organic Thin Films of Large Aromatic Hydrocarbons - Structure and Physical Properties, (2 Lectures),
PCAM – Physics and Chemistry of Advanced Materials; European Doctorate,
Mailand (Italy), 14.-15.10.2014.

Epitaxial Organic Thin Films of Large Aromatic Hydrocarbons - Structure and Physical Properties,
Department of Photo-Molecular Science, Institute of Molecular Science,Okazaki (Japan),
12.09.2014.

Epitaxial Organic Thin Films of Large Aromatic Hydrocarbons - Structure and Physical Properties – Recent Results,
Department of Chemistry, Kyoto University, Kyoto (Japan), 04.09.2014.

Recent Results on Organic-Organic Heterostructures and on Doping of Molecular Films,
Department of Chemistry, Osaka University, Osaka (Japan), 02.09.2014.

Epitaxial Organic Thin Films of Large Aromatic Hydrocarbons - Structure and Physical Properties",
Department of Electronics and Mechanical Engineering, Chiba University, Chiba (Japan), 26.08.2014.

Epitaxial Organic Thin Films of Large Aromatic Hydrocarbons - Structure and Physical Properties,
Kolloquium am Institut für Physik, Technische Universität Ilmenau, Ilmenau, 29.04.2014.

Structure and Physical Properties of Epitaxial Molecular Layers - The Influence of K-Doping,
Kolloquium am Institute of Solid State Physics, Graz University of Technology, Graz (Österreich), 23.04.2014.

Epitaxial Organic Thin Films of Large Aromatic Hydrocarbons - Structure and Physical Properties,
SPERC Seminar, King Abdullah University of Science and Technology, Thuwal (Saudi Arabien), 12.03.2014.

C. Ronning:

Ion beam doping of semiconductor nanowires
Inter. Conf. on Ion beam Modification of Materials (IBMM) 2014, Leuven, Belgium, 19.09.2014

Semiconductor nanowire photonics
Nanowire back2back workshop, Eindhoven, Netherlands, 28.08.2014

Ion beam doping of ZnO nanowires
CECAM workshop “Nanostructured ZnO and related materials”, Bremen, 24.06.2014

Ion beam doping of GaN and related nanostructures
E-MRS spring meeting, Lille, France, 29.06.2014

Lasing in Semiconductor nanowires
Physics Colloquium, University of KwaZulu-Natal, Durban, South Africa, 27.02.2014

Lasing in Semiconductor nanowires
Physics Colloquium, University of Stellenbosch, South Africa, 20.02.2014

P. Seidel:

Present Status of Research Projects on Iron-based Superconductors in Germany
ISS'2014, Tokio, Japan, November 25-27, 2014

Modelling different kinds of Josephson junctions an circuits for interpretation of their electrical characteristics
9th Int Symp Intrinsic Josephson Effects and THz Plasma Oscillations in High-Tc superconductors, Kyoto, Japan, November 30 - December 3, 2014

E. Wendler:

Application of ion beams in material science
Master Program at School of Physics, Aristotle University of Thessaloniki, Greece, 08.12.2014

C.S. Schnohr:

Irradiation effects in compound semiconductors studied by X-ray absorption spectroscopy
MRS spring meeting, San Francisco, USA, 23.04.2014

Chalcopyrite semiconductors: Atomic-scale structure and band gap bowing
DPG spring meeting, Dresden, Germany, 01.04.2014

R. Nawrodt:

Materials for the Einstein Telescope – Overview
6th Einstein Telescope Symposium Lyon, France, November 19-20, 2014

C. Jäger:

Cold condensation of dust in the ISM
Faraday Discussion 168 − Astrochemistry of Dust, Ice and Gas, Leiden, 7-9 April 2014

Cosmic dust in the laboratory: From Molecules to Solids
International Workshop on Astromineralogy II, Research Center for Astronomy and Earth Sciences,
Budapest, 29 -30 September 2014

Synthesis of cosmic dust analogs and *Processing of grains*
Tutorial at the summer school ''Laboratory Astrophysics'', Tabarz, 13 – 16 October

Processing of grains
Tutorial at the summer school ''Laboratory Astrophysics'', Tabarz, 13 – 16 October

Ion-induced erosion of carbon grains: Astrochemistry at the interface grains/ice in molecular clouds and protoplanetary disks
Planet and star-formation workshop of the Max Planck Institute for Astronomy, Kloster Schöntal,
Germany, 12-14 November 2014

G. Rouillé:

Formation of silicates in the interstellar medium: Laboratory experiments
Seminaires du Laboratoire d'Astrophysique de Bordeaux, Observatoire de Bordeaux, France, April 30, 2014

Molecules and UV/vis Photons - From the ISM to the Laboratory
Tutorial at the summer school ‘‘Laboratory Astrophysics’’, Tabarz, 13 – 16 October

Growth of silicate grains in the ISM: An experimental study
Planet and Star Formation Workshop 2014, Kloster Schöntal, Germany, 12-14 November 2014

S. Krasnkokutski:

Cryochemistry in the Inert and Interstellar Media
Tutorial at the summer school ‘‘Laboratory Astrophysics’’, Tabarz, 13 – 16 October

Reactions in He clusters
Planet and star-formation workshop of the Max Planck Institute for Astronomy, Kloster Schöntal,
Germany, 12-14 November 2014

D. Fulvio:

Radiation-Induced Processing at the Interface Ice/Dust Grains
Tutorial at the summer school ‘‘Laboratory Astrophysics’’, Tabarz, 13 – 16 October, 2014
The conundrum of the missing silicon carbide (SiC)
Invited Talk at the Laboratory for Experimental Astrophysics Group in Catania, INAF - OACT, Italy, 3 Sept. 2014

A straightforward method for VUV flux measurements: The case of the H_2 discharge lamp and implications for solid-phase actinometry
Invited Talk at the Laboratory for Experimental Astrophysics Group in Catania, INAF - OACT, Italy, 1 Sept. 2014;

Radiation-Induced Processing at the Interface Ice/Dust Grains
Tutorial at the summer school ‘‘Laboratory Astrophysics’’, Tabarz, 13 – 16 October

3.3 Theses

(A) Bachelor Theses and Studienarbeiten

Andreas Masek	*Optische Spektroskopie und LEED an Blei-Phthalocyanin auf Graphen*
Josua Kottke	*Gradientensublimation und Quadrupol-Massenspektroskopie*
Susanne Fuchs	*Schalten von Molekülen in einer SnPc/PTCDA-Heterostruktur*
Tino Morgenroth	*Strukturbestimmung von hoch geordneten DBP Filmen auf Au(111)*

Sascha Creutzburg	*Untersuchung der elektrischen Eigenschaften von funktionalisierten ZnO-Nanodrähten*
Maximilian Zapf	*Oberflächenmodifikation von ZnO-Halbleiternanodrähten für sensorische Anwendungen und die UV-Photodetektion*
Kevin Murray	*UV-VIS Spektroskopie an ZnO Nanodrähten*
Torsten Lindemann	*Kathodo- und Photolumineszenz-Untersuchungen an CIGSe-Hochtemperaturabsorbern*
Walter Dickmann	*Elektrische Charakterisierung von CIGS-Solarzellen*
Julia Baldauf	*Charakterisierung von Struktur und Eigenschaften von ß-Ga_2O_3 Einkristallen*
Philipp Lorenz	*Gallium-, Stickstoff- und Europium-Ionenimplantation zur optischen Dotierung von SiO_2*
Florian Wittkämper	*Ionometrische Untersuchungen an homoepitaktischen ZnO-Schichten*
Jari Domke	*Nachweis von Fremdatomen in Glas mittels RBS*
Leonie Kaczmarek	*Transmissionselektronenmikroskopie von Siliziumkarbid nach Ionenimplantation bei 625 K*
Malte Per Siems	*Bestimmung der Absorption in Silizium bei 1550 nm*
Brian Seyfarth	*Messungen der thermo-optischen Koeffizienten von Saphir von 10 bis 410 K*
Christian Hopf	*Charakterisierung eines Großhub-SQUID mit intrinsischer Rückkopplung*
Jessica Golm	*Messverfahren zur Bestimmung supraleitender Materialparameter*
Sabine Stück	*Modifikation von YBCO-Schichten mit Au-Nanopartikeln*

(B) Diploma, Master Theses, and State Examination Theses

Christian Zwick	*Dotierung hochgeordneter, ultradünner Schichten organischer Moleküle - Das System PTCDA+nK/Ag(111)*
Julia Peuker	*Epitaktisches Wachstum von organisch-organischen Heterosystemen*
Tino Kirchhubel	*Wachstum und Dotierung ultradünner DBP-Schichten auf Metalleinkristallen und Glimmer*
Tobias Hümpfner	*Wachstum und Dotierung von Coronen*
Tesfaye Belete	*Thinning of thin-film Cu(In,Ga)Se_2 solar cell absorber layer*
Martin Salge	*Herstellung und elektrische Charakterisierung von dotierten CdTe-Dünnschichtsolarzellen*
Martin Krauße	*Elektrooptische Untersuchungen an ionenimplantierten InS-Dünnschichten*

Alexander Kusch	*Elektrische und strukturelle Untersuchungen an sequenziell prozessierten Cu(In,Ga)Se2-Solarzellen*
Marcel Hopfe	*Ionenimplantation und thermische Ausheilung von Vanadiumdioxid-Dünnschichten*
Alexander von Müller	*Investigations of ion beam induced nanoscale ripple patterns and their effect on protein-surface adsorption*
Sebastian Vatterodt	*Elektrische und optische Charakterisierung von undotierten und dotierten Vanadium (IV)-oxid-Dünnschichten*
Stefan Noack	*Sputter effects of silicon nanowires under ion bombardement*
Romina Diener	*Modifikation der supraleitenden Schichteigenschaften von YBCO durch Nanopartikelwachstum*
Falk Wyrwa	*Strukturelle Untersuchungen an dünnen YBCO-Schichten mit Au Nanopartikeln*
Bastian Walter	*Verlustuntersuchungen an dielektrischen Materialien*
Robert Müller	*Entwicklung und Realisierung reaktive Multischichtsysteme für laserinduzierte Bondverfahren*
David Reifert	*Elektrische Untersuchungen an Pniktid-Einkristallen*

(C) PhD Theses

Michael Kozlik	*Hybrid Solar Cells*
Jana Sommerfeld	*Ion beam modification of surfaces for biomedical applications*
Ivo Zunke	*Erzeugung von halbleitenden transparenten Zinkoxid-Nanoschichten unter Atmosphärendruckverhältnissen durch flammenpyrolytische Abscheidung*

4. Cooperations, Visiting Scientists, and Colloquia at the IFK

4.1 Cooperations

The Institute of Solid State Physics collaborates with a large number of Institutes and Universities in Germany and around the world and has also close connections with several companies. In the framework of these wide spread contacts a large number of scientists from various countries visited our Institute in 2014 to perform experiments, discuss scientific results obtained within joint projects and to give talks in the colloquium of the Institute of Solid State Physics.

The Surface Science group of **Prof. Dr. T. Fritz** strengthened their international cooperations in 2014. While the ongoing collaboration with the group of Prof. Dr. T. Munakata (University of Osaka) was continued and even intensified by numerous exchange visits (founded via a PaJaKo project of the DAAD) between German and Japanese Scientist new collaborations were started with the groups of Prof. Dr. N. Ueno (University of Chiba) and Prof. Dr. S. Kera (Institute of Molecular Science, Okazaki). In the USA we cooperate with the group of Prof. Dr. O. Monti (University of Arizona). Within Europe we have intensive collaborations with the theory groups of Prof. Dr. E. Zojer (Graz University of Technology) and Prof. Dr. G.-P. Brivio (Universita` di Milano-Bicocca). In Germany our collaborations included the group of Prof. Dr. C. Kumpf (Forschungszentrum Jülich GmbH) and Prof. Dr. J. Kröger (TU Ilmenau).

The group of **Prof. Dr. C. Ronning** collaborated in 2014 with various international groups. Special situations have been established with the groups of Prof. Dr. F. Capasso (U Harvard), Prof. A. Lugstein (TU Vienna), Prof. A. Fontcuberta i Moral (EPF Lausanne), and Prof. K. Bharuth-Ram (iThemba Labs, South Africa), which have been founded either by the DAAD or DFG. Further collaborations have been conducted with the groups at the University of Lund (Sweden, Prof. L. Samuelson), Australian National University Canberra (Australia, Prof. M. Ridgway), University of Southern California (USA, Prof. J.G. Lu), University of Florence (Italy, Dr. F. di Benedetto), University of the Basque Country (Spain, Prof. A. Rubio), Institute of Light and Matter (France, Dr. S. Botti), ERSF Grenoble (France, Dr. G. Martinez-Criado & Dr. F. d'Acapito) and Imperial College (UK, Dr. R. Oulton & Prof. O. Hess). National collaborations involve partners from Bremen, Duisburg, Mainz, Leipzig, Braunschweig, and Erlangen within the frame of the DFG research unit FOR1616. However, collaborations have been also established to groups at the HZ Berlin, FHI Berlin and ZSW Stuttgart on photovoltaics.

The ***Low Temperature Physics*** group of Prof. Dr. Paul Seidel is collaborating with Thuringian research institutions (TU Ilmenau, IPHT Jena, SUPRACON Jena, Innovent e.V. Jena, Helmholtzinstitut Jena, Universitätsklinikum Jena). Within funded research projects joint research is carried out with the IFW Dresden, the GSI Darmstadt, the DESY Hamburg, the MPI Heidelberg and the CERN Genf. Long-term collaborations exist to the Karlsruhe Institute of Technology KIT and the research groups at the universities in Erlangen-Nürnberg, Hannover, Dresden, Gießen, Heidelberg, Tübingen as well as the Universities of Applied Science in Aalen and Jena.

Within the German Collaborative Research Center (SFB TR7) scientific results have been obtained in close collaboration with national (Hannover, Tübingen, Golm, Garching) as well as international partners, such as the universities of Glasgow, Padova, Lyon, Tokyo, Pisa, Salerno, Roma, Moscow and others. Additional international partners in the field of superconducting materials and its application are the universities of Bratislava, Poznan, Twente, Donetsk, Kharkov, Osaka, Nagoya and Tokyo.

The **Ion Beam Physics group** cooperated in 2014 with Prof. Dr. Fadei F. Komarov (BGU Minsk), Prof. Dr. Maria Katsikini (U Thessaloniki), Dr. Katharina Lorenz (IST, U Lissabon), Prof. Dr. Johan B. Malberbe (U Pretoria), Dr. Alexander Yu. Azarov (U Oslo) and Dr. Albert Juma (now U Gaborone, Botswana). National cooperations exist with Dr. Klaus Ellmer and Dr. Thomas Dittrich (HZ Berlin), Dr. Jürgen Vogt (U Leipzig), Dr. Stefan Grimm (IPHT Jena) and Robert Hanf (j-fiber Jena).

The working group **Laboratory Astrophysics and Cluster *Physics*** collaborates with a number of institutes both at home and abroad. Experimental studies of molecular hydrogen formation on the surface of silicate dust grains under astrophysical conditions have been performed in collaboration with Prof. J.-L. Lemaire and Prof. Dr.Gianni Vidali from the Observatoire de Paris and Université de Cergy-Pontoise). In the field of UV-induced reactions of astrophysically relevant molecules in cryogenic matrices, close collaborations exist with Prof. Harold Linnartz from the Raymond and Beverly Sackler Laboratory for Astrophysics, Leiden Observatory (Netherlands), and Prof. Stephen Price at the Chemistry Department of the University College London. The formation of molecules in interstellar ices and the erosion of carbonaceous solids in the dense interstellar medium by proton bombardment are the topics of a joint project with the Laboratory Astrophysics Group at INAF–Osservatorio Astrofisico di Catania, Italy. These scientific connections were mainly built during the Marie Curie ITN network "LASSIE- Laboratory Astrophysics Surface Science in Europe'' that was working between 2010 and 2014. Intensive collaboration with Dr. Akos Keszturi and Prof. Peter Abraham, Research Centre for Astronomy and Earth Sciences, Budapest, Hungary, has been established in the last years. Here, we focus on joint laboratory work including condensation experiments and spectroscopy of condensates at low temperature. With Prof. Stephan Schlemmer, Cologne Laboratory Astrophysics Group, Prof. Thomas Giesen, Laboratory Astrophysics Group at the University Kassel, and Dr. Holger Kreckel, Max Planck Institute for Nuclear Physics in Heidelberg, long-standing collaborations in the field of laboratory astrophysics, structure, dynamic, and properties of molecules and dust grains in astrophysical environments have been existing for more than 10 years.

4.2 Visiting Scientists

Prof. Dr. Puxian Gao	U Connecticut, USA – **Humboldt-Professor for 1 year**
Prof. Dr. T. Munakata	Osaka University, Japan
Prof. Dr. H. Kato	Osaka University, Japan
MSc N. Kawakita	Osaka University, Japan
Prof. Dr. K. Baruth-Ram	iThemba Labs, Cape Town, South Africa

Prof. Dr. J. Grace Lu	University of Southern California, USA
M. Glaser	TU Wien, Austria
Dr. G. Martinez-Criado	ESRF Grenoble, France
M. Geelen	U Hasselt, Belgium
Prof. Dr. M. Katsikini	Aristotle U Thessaloniki, Greece
Prof. Dr. J. B. Malherbe	U Pretoria, South Africa
Prof. Dr. K. Somiya	Tokyo Institute of Technology
Prof. Dr. T. Tomaru	KEK Tsukuba
Dr. M. Belogolovskii	Donetsk Institute for Physics and Engineering
Dr. K. Kulikov	Joint Institute for Nuclear Research Dubna
Dr. A. Bell	University of Glasgow
T. Kawaguchi	Nagoya University
R. Douglas	University of Glasgow
D. Chen	University of Tokyo
Dr. A. Gucsik	Konkoly Thege Miklos Astronomical Institute, Astrophysical and Geochemical Laboratory, Budapest, Hungary and Department of Geology, University of Johannesburg
S. Gobi	Konkoly Thege Miklos Astronomical Institute, Astrophysical and Geochemical Laboratory, Budapest, Hungary
S. Cuylle	Raymond and Beverly Sackler Laboratory for Astrophysics, Leiden
H. Kimber	Department of Chemistry, University College London, UK
A. Nanni	Astrophysics, University of Keele, Staffordshire, UK

4.3 Colloquia at the Institute of Solid State Physics

Prof. Dr. Jörg Kröger (TU Ilmenau), 11.04.2014
Exploring surface physics and chemistry with a scanning tunnelling microscope

Prof. Dr. Jörg K.N. Lindner (U Paderborn), 25.04.2014
Nanostrukturierte Oberflächen - nicht nur zum Spass.
Ehrenkolloquium zur Verleihung des apl. Prof. an Elke Wendler

Prof. Dr. Rolf Möller (Universität Duisburg-Essen), 09.05.2014
Scanning Tunneling Microscopy on Molecules analyzing Ballistic Transport and Current Noise

Dr. Selina Olthof (Universität Köln), 23.05.2014
Trap passivation in organic semiconductors by ultra low molecular doping and the application in organic field effect transistors

Dr. Lutz Geelhaar (PDI Berlin), 06.06.2014
Towards optoelectronic applications based on III-As and III-N nanowires on Si substrates

Dr. Silvia Haindl (Eberhard-Karls-Universität Tübingen), 04.07.2014
Fe-based superconducting thin films - an overview

Mini symposium "*Surface Sensitive Optical Spectroscopies*", 11.07.2014
Prof. Dr. Moritz Sokolowski (Universität Bonn)
Fluorescence spectroscopy of PTCDA on KCl and NaCl surfaces
Prof. Dr. Lindong Sun (Universität Linz)
Organic thin film growth studied by reflectance difference spectroscopy

Prof. Dr. Hiroyuki Kato (Osaka University), 07.11.2014
Arrangement and Electronic State Properties of Self-Assembled Molecules on Surfaces

Prof. Dr. Thomas Hannappel (TU Ilmenau), 28.11.2014
Solarenergiekonversion in hocheffizienten Tandemstrukturen

Prof. Dr. Stefan Mannsfeld (cfaed TU Dresden), 12.12.2014
Engineering of Plastic Electronics

Prof. Dr. Geppo Cagnoli (University of Glasgow), 09.01.2015
Modern Coatings for Advanced and Future Gravitational Wave Detectors

Prof. Dr. Sibylle Gemming (TU Chemnitz / HZDR), 23.01.2015
Silicon Nanocrystals produced by Solid Phase Crystallisation for Photovoltaic Applications

Prof. Dr. Christian Loppacher (IM2NP - UMR CNRS), 30.01.2015
Spectroscopic Investigation of Unoccupied Molecular States at the Nano- and Macroscopic Scale

5. Personnel

Professors

Prof. Dr. habil. Torsten Fritz (director)
Prof. Dr. habil. Carsten Ronning
Prof. Dr. habil. Paul Seidel
apl. Prof. Dr. habil. Elke Wendler
apl. Prof. Dr. habil. Frank Schmidl

Scientific Staff

Dr. Abel Brieva (till 03/2014)
Dr. Roman Forker
Dr. Daniele Fulvio
Dr. Ernst Glaser
Dr. Daniel Heinert
Dr. Cornelia Jäger
Dr. Sergiy Krasnokutski
Dr. Ronny Nawrodt
Dr. Michael Oertel
Dr. Udo Reislöhner
Dr. Gael Rouillé
Dr. Jana Sommerfeld
Dr. Bernd Schröter
Dr. Claudia Schnohr
Dr.-Ing. Christian Schwarz
Dr.-Ing. Volker Tympel

PhD Students

Davide Cammi
Sebastian Döring
Stefanie Eckner
Martin Gnauck
Marco Grünewald
Yaser Haj-Hmeidi
Christoph Heisler
Gerd Hofmann
Henry Holland-Moritz
Tobias Hümpfner (since 10/2014)
Andreas Johannes
Christian Katzer
Tino Kirchhübel (since 10/2014)
Julius Komma
Matthias Meissner
Ali Hasan Noor
Karsten Potrick
Robert Röder
Tolou Sabri
Emanuel Schmidt
Matthias Schmidt
Stefan Schmidt
Philipp Schöppe
Sven Schönherr
Falko Sojka
Jura Rensberg
Christian Udhardt
Steffen Wolf
Christian Zwick (since 10/2014)

Extern PhD Students

Constantin Csato	FH Jena
Martin Kommer	fem Schwäbisch Gmünd
Florian Krippendorf	FH Jena
Gregor Oeslner	IPHT Jena
Matthias Rost	Bosch Solar EnergySolarworld, Arnstadt
Thomas Schönau	IPHT Jena
Charlotte Weiss	Frauenhofer ISE, Freiberg

Ivo Zunke — Innovent Jena

Diploma and Master Students

Adebowale Ephraim Anthony
Tim Barth
Sven Bauer
Gregor Becker
Tesfeye Belete
Ellen Butz
Romina Diener
Felix Felgenträger
Jonas Gronemann
Erik Haubold
Marcel Hopfe
Tobias Hümpfner
Tino Kirchhübel
Alexander Kusch
Martin Krause
Robert Müller
Alexander von Müller
Stefan Noack
Julia Peuker
Felix Otto
David Reifert
Max Riediger
Konrad Ritter
Benjamin Rößler
Lisa Schade
Markus Schwiderke
Alexander Tille
Lukas Trefflich
Enrico Treiber
Bastian Walter
Marcel Wille
Falk Wyrwa
Christian Zwick

External Diploma and Master Students

Michelle Geleen (U Hasselt, Belgium)
Claudia Schnitter (U Linköping, Sweden)
Marcus Junghanns (IPHT Jena)

Technical Staff

Ulrich Barth
Marie Boxhammer
Uwe Eberhardt
Tobias Eißmann
Lutz Föllmer
Silke Frunzke
Kristina Garlipp
Frank Jehn
Patrick Hoffmann
Holger Mühlig
Anja Mittelstädt
Ralf Neubert
Stefan Prass
Helga Rudolph
Sylvia Stender
Matthias Thürk
Carmen Voigt

6. Technical Reports and Equipment

6.1 Operation of the Ion-Accelerator JULIA and the Ion-Implanter ROMEO

U. Barth, P. Hoffmann, F. Jehn, C. Ronning

The 3 MV high current tandetron accelerator **JULIA** (***J***ena ***U***niversity ***L***aboratory for ***I***on ***A***cceleration) went in operation end of 1996. Since the beginning of the routine-operation in 1997 it has been used for different types of experiments requiring a broad spectrum of ion-beams. With the exception of helium, where the duoplasmatron ion-source followed by a lithium exchange channel was used, all ions were extracted from a sputter-type ion-source.

Table 1: Ion beams accelerated until 2014. The currents given are measured at the Q-Snout-Faraday-cup after the low-energy mass separator (JULIA) and at the target position (ROMEO), respectively.

Period	Element	Julia	Romeo
1	Hydrogen (H)	1 µA	4 µA
	Helium (He)	0,1 µA	4 µA
2	Lithium (Li)	2 µA	-
	Boron (B)	0,1 µA	5 µA
	Carbon (C)	3 µA	1 µA
	Nitrogen (N)	0,4 µA	4 µA
	Oxygen (O)	2 µA	2 µA
	Flourine (F)	-	2 µA
	Neon (Ne)	-	5 µA
3	Sodium (Na)	-	6 µA
	Magnesium (Mg)	-	5 µA
	Aluminium (Al)	-	4 µA
	Silicon (Si)	16 µA	4 µA
	Phosphorus (P)	1 µA	4 µA
	Sulfur (S)	1 µA	-
	Chlorine (Cl)	-	2 µA
	Argon (Ar)	-	20 µA
4	Potassium (K)	-	3 µA
	Calcium (Ca)	-	5 µA
	Titanium (Ti)	0,7 µA	-
	Vanadium (V)	0,2 µA	1 µA
	Manganese (Mn)	0,02 µA	5 µA
	Chromium (Cr)	0,2 µA	3 µA
	Iron (^{56}Fe)	0,8 µA	2 µA
	Iron (^{57}Fe)		0,015 µA
	Cobalt (Co)	-	3 µA
	Nickel (Ni)	-	6 µA
	Copper (Cu)	0,5 µA	1 µA
	Zinc (Zn)	0,05 µA	6 µA
	Gallium (Ga)	-	3 µA
	Germanium (Ge)	1,6 µA	4 µA
	Arsenic (As)	0,4 µA	1 µA
	Selenium (Se)	0,5 µA	1,5 µA

Period	Element	Julia	Romeo
4	Bromine (Br)	10 µA	8 µA
	Krypton (Kr)	-	10 µA
5	Rubidium (Rb)	0,07 µA	1 µA
	Strontium (Sr)	-	3 µA
	Yttrium (Y)	-	4 µA
	Zirconium (Zr)	0,3 µA	1,5 µA
	Rhodium (Rh)	0,2 µA	-
	Palladium (Pd)	0,09 µA	1 µA
	Silver (Ag)	1,6 µA	10 µA
	Cadmium (Cd)	-	0,8 µA
	Indium (In)	0,5 µA	8 µA
	Tin (Sn)	1,0 µA	3 µA
	Antimony (Sb)	0,6 µA	4 µA
	Tellurium (Te)	-	2 µA
	Iodine (I)	3 µA	-
	Xenon (Xe)	-	10 µA
6	Caesium (Cs)	-	4 µA
	Barium (Ba)	-	1 µA
	Praseodymium (Pr)	-	1 µA
	Neodymium (Nd)	-	0,5 µA
	Samarium (Sm)	0,01 µA	1,5 µA
	Europium (Eu)	0,03 µA	2 µA
	Erbium (Er)	0,04 µA	2 µA
	Thulium (Tm)	-	1 µA
	Tantalum (Ta)	0,2 µA	2 µA
	Tungsten (W)	0,3 µA	0,01µA
	Osmium (Os)	0,05 µA	-
	Iridium (Ir)	0,3 µA	6 µA
	Platinum (Pt)	0,2 µA	-
	Gold (Au)	2,8 µA	20µA
	Lead (Pb)	0,03 µA	15µA
	Bismuth (Bi)	-	3µA

The beam-on-target-time of 1200 h was about 30% lower than in 2013. The 400 kV ion-accelerator **ROMEO** is in routine operation since 1998, here the beam-on-target-time of 850 h was also 30 % lower as in the preceding years. The cause for this shorter period of time was a long failure of cooling water. Both accelerators can be operated separately or in combination. The ion-beams produced until 2013 are summarized in table 1. The ion-beam currents quoted are typical values of the ion source currents used for the experiments. The maximum currents available are significantly higher for most ions.

The computer control of the accelerator Julia was modernized in this year. The hardware was changed to a modern control system, as shown in figure 1. The data transmitting to the accelerator is now serially coded via light guides.

One can now use the new software for many more applications. For example overview control on one panel, automatic shut downs, duoplasma gas control, ion tables, or parameter calculations. Furthermore, the operational safety has been significantly increased by this upgrading.

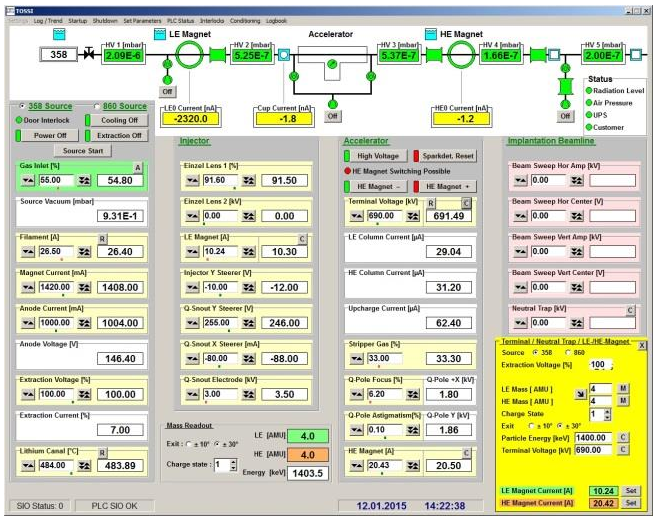

Figure 1: The new Tandetron Operating System called "Tossi".

As in the preceding years the ion-beam facility was used also by external research groups:

3MV-Tandetron „JULIA"

- HZ Berlin für Materialien und Energie
  Dr. A. Juma
- Universität Stuttgart
  Dipl. Phys Widmann
- Fachhochschule Jena
  Prof. Rüb
- IPHT Jena
  Dr. Diegel

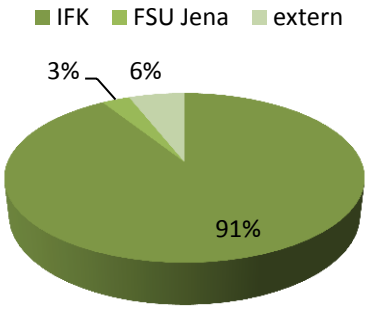

400kV Implanter „ROMEO"

- University of Conneticut, USA
  Prof. Puxian Gao
- iThemba Labs, Kapstadt-Südafrika
  Prof. K. Bharuth-Ram
- University of Pretoria, Südafrika
  Prof. Malherbe
- IAP Jena
  Dr. F. Schrempel

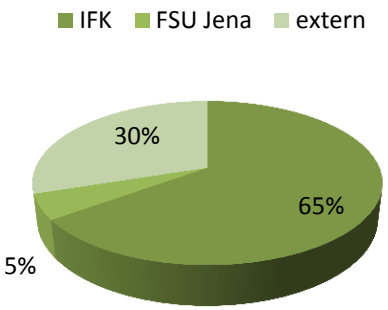

6.2 Cryogenic Services (TTS)

M. Thürk

All in-house customers of cryogenic liquids, which are all faculties of natural sciences, the university medical division including several hospitals, and other external scientific institutes (e.g. Leibniz Institute for Photonic Technology Jena, Leibniz Institute Hans-Knöll Jena) as well as some private customers like the Innovent e.V. Jena and some medical practices, were provided with liquid helium (LHe), with high purity gases (He, N_2), and with cryogenic gases like liquid nitrogen (LN_2) and liquid argon (LAr) by the Cryogenic Services. Roughly 123,000 litres of LN_2 were delivered by the cryogenic services in 2014. The total delivery has increased last years due to additional demands of inert gas in the IAAC-institute and the new installed ZAF site.

As illustrated in Figure 1, the output of liquid helium (LHe) has levelled off in 2014. Roughly 36,000 litres of LHe were delivered which calls for an annual gross refrigeration value of just 42,600 litres which corresponds to an annual all round price of € 0.43 million. Last three years we had to face a worldwide shortage in helium supplies which leads generally to increased costs with enduring fluctuations of the competitive market price over the year. On the crest of the wave the costs for short term LHe-orders have increased by a fivefold. In addition the long-term delivery contracts with fixed prices weren't fulfilled by the suppliers relating due to the delivered quantity. Therefore the financial weakness and supply shortfall have caused a strong reduction in LHe-use since 2012. Fortunately the relation between the produced amount of LHe to the bought quantity was a good deal bigger than the years before 2012. This was possible due to the increased efforts of the LHe-users to decrease He-losses. In spite of the lower production rate the rising market prices increased the gross financial benefits of the internal helium liquefaction for all users noticeably.

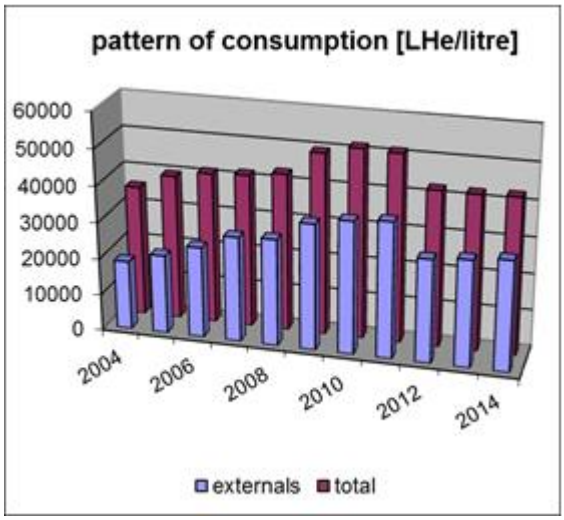

Figure 1: Liquid helium output

The TTS-staff executed design, installation control and commissioning of two new pure argon storage tanks at the Helmholtzweg 4 site and the ZAF site, as well as the new LAr logistics at the Lessingstraße 5. The project "helium- recovery" for the Max-Wien-Platz 1 site is under way.

Ground instabilities due to the ongoing rotting of cavities below the earth's surface endangered the LN_2-supply carried out by heavy trucks. The necessary reconstruction in the basement was put into practice by the department of construction engineering of the Friedrich-Schiller University. The extensive constructions works caused no limitations for the LN_2 supply at all. This fact is very appreciated by the TTS.

6.3 Equipment

Preparation of Thin Films and Devices

- HV evaporation facilities for thermal and electron beam evaporation
- UHV evaporation facilities, including electron gun and in situ RHEED system
- Equipment for laser deposition of thin crystalline films and material systems, especially high temperature superconductors (KrF excimer laser, $\lambda = 248$ nm)
- Molecular Beam Epitaxy (MBE) facilities: MBE for silicon carbide (RIBER EVA 32 R&D)
- Organic Molecular Beam Epitaxy (OMBE) facilities including surface analysis techniques (MCP-LEED, UHV STM/AFM, RHEED) and *in situ* optical spectroscopy (PL and DRS)
- dc and rf sputtering systems for metallic (Au, Ti) and oxidic (SiO_2, Ta_2O_5) thin films and multilayers
- Ion beam etching with Ar ions at sample temperatures down to 80 K in vacuum
- Chamber for ion- and reactive etching up to 4" wafer
- Reactive ion beam etching with sample diameters up to 6 cm
- Ultrasonic wire bonder
- Equipment for photolithographic patterning
- MBE system NEBULA for $Cu(In,Ga)S_2$ layers on 4'' substrates including RHEED setup
- Two HV systems for closed-space sublimation (CSS) for deposition of CdTe layers
- RF reactive sputtering system for transparent conducting oxides (TCO's) and molybdenum
- DC sputtering system for copper and indium
- UHV system ULS400 for $Cu(In,Ga)(Se,S)_2$ on (100x100) mm^2 substrates
- Wet chemical processing and chemical bath deposition of photoactive layers

Surface Analysis Systems

- LT-STM/AFM (1.1 K) with 3 Tesla magnet, QMS (1000 amu), MCP-LEED, DRS
- Surface analysis systems SPECS and UNISPEC with XPS, UPS, AES, LEED, STM
- AUGER electron spectrometer
- Atomic force microscopes (AFM and Microstructure Measuring Device VERITEKT 3 with needle sensor)
- Surface profilometer DEKTAK 100
- Scanning electron microscopes
- Several UHV-scanning probe devices (STM, AFM)

Electrical Measurement Techniques

- Electrical transport measurements (resistance, critical current density, point contact and tunneling spectroscopy)
- Hall-effect and Four-point probe equipment
- Current-voltage characteristics ($2\ K < T < 300\ K$, $B \leq 5\ T$)
- Current-voltage characteristics by microwave irradiation ($2\ GHz < f < 300\ GHz$)
- Noise measurements (frequency range 60 µHz - 100 kHz) at low temperatures
- LTS-SQUID characterization at 4.2 K (current-voltage, flux-voltage, noise, screening properties)
- HTS-SQUID characterization up to 100 K (current-voltage, flux-voltage, noise)
- 2 Deep level transient fourier spectrometers (temperature range 80 K - 690 K, 30 K - 330 K)

- 3 Admittance spectrometers (frequency range 40 Hz - 100 kHz, 20 Hz - 2 MHz and 75 kHz - 30 MHz, temperature range 30 K - 690 K)
- Microwave signal generator (frequency range 1 - 20 GHz, resolution: 1 kHz)
- Electrical and optical characterization of high power diode laser arrays

Equipment for Optical Characterization

- UV-VIS spectrometer
- FTIR spectrometer
- Cathodoluminescence at SEM, equipped for IR - UV
- Micro-Photoluminescence, IR-UV, time-resolution ~ 1ns
- Photoluminescnce excitation (PLE)
- Optical cryostats (2…300 K) for optical absorption, photoluminescence and Raman spectroscopy
- Excitation lasers in a wide range from 405-1550 nm (fiber, gas, solid state and diode lasers)
- Optical microscopes
- Magnetrelaxation of ferrofluids (MORFF) for characterization of magnetic nanoparticles

Equipment for Electro-Optical (Solar) Characterization

- Solar simulator (AM 1.5) with Current-Voltage measurement
- Illumiated Current-Voltage measurements for 10 K to RT
- Quantum efficiency (EQE) measurements of solar cells

Equipment for Thermal Treatment

- Furnace for conventional thermal treatment in inert gas atmosphere or vacuum (temperatures up to 2050 K)
- RTA apparatus (double graphite strip heater) for short time annealing (annealing time in the order of seconds, temperature range 1000 K to 1950 K, temperature rise rate 100 K s^{-1})

Electron Microscopy

- Scanning electron microscope JEOL JSM-6490 with LaB_6-cathode
- FEI field-emission electron microscope connected with FIB system

Ion Beam Techniques

3 MV Tandetron accelerator "JULIA", equipped with

- Sputter ion source and Duoplasmatron source
- Universal beam line for ion implantation and ion beam analysis
- Second beam line for ion beam analysis, combined with implantation chamber of 400 kV implanter
- Irradiation chamber with cooled and heated sample holder and four axis goniometer

Application:

- Ion implantation: energy range 500 keV - 12 MeV, temperature range 15 K - 1500 K
- Ion beam analysis: RBS and PIXE in combination with channeling, ERDA, NRA

400 kV implanter "ROMEO", equipped with

- Hot filament, hollow cathode ion source
- Irradiation chamber with cooled and heated sample holder and four axis goniometer, combined with beam line of 3 MV Tandetron accelerator

Application:

- Ion implantation: energy range 20 keV - 400 keV, temperature range 15 K - 1500 K
- Ion implantation at low temperatures and subsequent RBS analysis using H- or He-ions from 3 MV Tandetron accelerator

Low Energy implanter "LEILA", equipped with

- Colutron Ion source 100-Q
- Colutron Ion Gun System G-2-D
- Irradiation chamber with heated sample holder

Application:

- Irradiation of surfaces: energy range sub-keV, temperature range 300 K - 750 K

Low Energy implanter "Mr. JIM Stringer", equipped with

- Hot filament, hollow cathode ion source
- Irradiation and deposition chamber

Application:

- Deposition of diamond-like thin films: energy range 100eV – 30 keV, RT

Focused Ion Beam system FEI NanoLab Helios 600i

- Liquid ion source, E = 500 eV – 30 keV
- Electron microscope, E = 350 eV – 30 keV

Application:

- TEM-lamella preparation, etc.

Low Temperature Measuring Equipment

- LT STM/AFM down to 1.1 K. 3 Tesla magnet available
- He-4 cryostats for temperatures down to 4.2 K
- He-4 refrigerator for the temperature range 1.3 K - 4.2 K
- Helium 3 refrigerator for temperatures range 4,2K - 300 mK with superconducting magnet to 2 T
- He-3/He-4 dilution refrigerator for temperatures range 4,2 K - 6 mK with superconducting magnet to 10 T
- He-3/He-4 dilution refrigerator with a base temperature of 35 mK
- Electronic equipment for characterization of cryoelectronic devices
- SQUID sensor systems for magnetic measurements under unshielded conditions
- SQUID sensor system for spatially resolved magnetorelaxometry
- Cryostats (2 K < T < 300 K; optical window; magnetic field)
- Cryocoolers (Gifford-McMahon and Stirling)
- Pulse tube refrigerators (for sensor cooling)

7. Scientific Reports

Potassium-chloride thin-films as decoupling layer for coronene on Ag(100)

Tobias Huempfner, Falko Sojka, Roman Forker, and Torsten Fritz

Coronene, $C_{24}H_{12}$, regained special interest after Kubozono *et al.* investigated superconductive properties among potassium intercalated coronene samples [1]. Though this research was done in the bulk, we want to study the properties of those systems in ultra-thin films. For that reason we searched for a proper substrate that allows us to perform structural investigations while the electronic influence of the substrate on these films is negligible. Insulating films like KCl on Ag(100) are known for their decoupling capabilities of molecular states from the metal surface. Müller *et al.* reported highly ordered growth of KCl on Ag(100) that does not depend on the structural quality of the underlying metal substrate [2]. We investigate here the influence of the KCl thin-film as decoupling layer on the growth of coronene adlayers.

Thin films of coronene and KCl were grown in ultra-high vacuum ($p \approx 10^{-9}$ mbar) on a sputter-cleaned, annealed Ag(100) surface using molecular beam epitaxy. During the growth of KCl the metal single crystal was heated to about 425 K, while it was cooled with liquid nitrogen during the deposition of coronene on KCl and kept at room temperature for the deposition of coronene on the bare metal surface. The structure of the grown adlayers was investigated via LEED and STM.

At a coverage of slightly more than 1 ML coronene directly on Ag(100) the LEED pattern in Fig. 1(a) shows defined spots that occur due to a highly ordered structure of the molecules. The analysis of

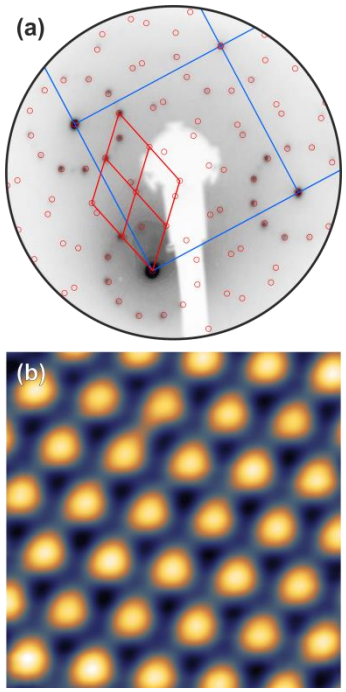

Fig. 1: *Structural analysis of 1 ML coronene on Ag(100). (a) LEED at 300 K, E = 57.1 eV, tilted off-normal by 11°. (b) STM at 1.1 K, 6.3 x 6.3 nm², V_t =1.0 V, I_s = 60 pA.*

that image leads to the following epitaxy matrix:

$$\begin{pmatrix}\vec{c}_1\\ \vec{c}_2\end{pmatrix} = \begin{pmatrix}4.00 \pm 0.02 & 1.00 \pm 0.02\\ -3.01 \pm 0.01 & 3.01 \pm 0.01\end{pmatrix}\begin{pmatrix}\vec{a}_1\\ \vec{a}_2\end{pmatrix}.$$

This matrix suggests a commensurate growth of the coronene adlayer on the Ag(100) surface within the experimental errors. As opposed to coronene adlayers on hexagonal surfaces, e.g., on Ag(111) [3], the molecular arrangement on Ag(100) differs slightly from a perfect hexagonal unit cell due to the quadratic lattice of this silver surface. In detail, the first lattice vector $|\vec{c}_1| = (11.92 \pm 0.05)$ Å is smaller than the second one $|\vec{c}_2| = (12.29 \pm 0.03)$ Å by about 3%. The angle between the vectors is $\sphericalangle(\vec{c}_1, \vec{c}_2) = (121.03 \pm 0.26)°$ which also differs significantly from 120°. Additionally, the first unit cell

vector is rotated w.r.t. the substrate by $\sphericalangle(\vec{a}_1, \vec{c}_2) = (13.97 \pm 0.25)°$. The associated STM measurements show this nearly hexagonal structure in large domains all over the sample as can be seen in Fig. 1(b). From the fact that the coronene itself exhibits a D_{6h} symmetry one may expect a preference of hexagonal molecular arrangements. We conclude that the energy gain resulting from the interaction with the substrate is higher than that resulting from mere intermolecular interaction. It is noteworthy that the commensurate structure does not appear until the surface is densely covered by coronene molecules.

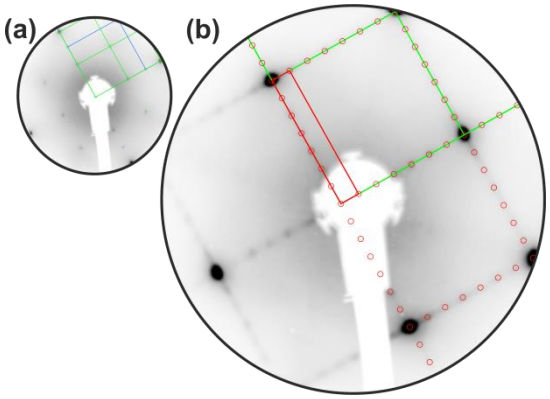

Fig. 2: *LEED of (a) KCl/Ag(100) at 300 K and E = 104.5 eV, with a structural simulation comparable to Ref. [2]; and (b) coronene on KCl/Ag(100) at ca. 80 K and E = 45.5 eV (blue: Ag(100), green: KCl, red: coronene).*

The LEED pattern of KCl/Ag(100) is shown in Fig. 2(a) and compares favorably with the results of Müller *et al.* [2]. The resulting LEED pattern shown in Fig. 2(b) was recorded after the deposition of coronene on KCl/Ag(100) while the sample was kept at ca. 80 K. The spots in this image can be explained by a rectangular structure taking into account all rotational domains arising from the quadratic structure of the substrate. We determine the following epitaxy matrix:

$$\begin{pmatrix} \vec{c}_1' \\ \vec{c}_2' \end{pmatrix} = \begin{pmatrix} 7.00 \pm 0.01 & 0.00 \pm 0.01 \\ 0.00 \pm 0.01 & 1.00 \pm 0.01 \end{pmatrix} \begin{pmatrix} \vec{b}_1 \\ \vec{b}_2 \end{pmatrix},$$

which again suggests a commensurate growth of the adlayer within the experimental errors. The length of the lattice vector $|\vec{c}_2| = (4.42 \pm 0.07)$ Å is much smaller than the van der Waals radius of a flat lying molecule. From this result we conclude that the molecules adsorb on KCl in an upright standing manner, in contrast to the nearly flat lying molecules on Ag(100). This might be caused by the weaker molecule-substrate interaction compared to the adsorption on the bare silver surface. In comparison, PTCDA adsorbs in flat lying geometry on KCl [2] mainly for two reasons: (i) the intermolecular interactions of PTCDA exhibiting an electrostatic quadrupole moment are effectively attractive, leading to the preferential formation of islands with flat lying molecules, and (ii) the attractive Coulomb interaction of the electronegative anhydride groups with the K^+-ions in the commensurate PTCDA/KCl epitaxial registry [2, 4].

In conclusion, the formation of highly ordered coronene films strongly depends on the properties of the substrate. While the molecules form a commensurate structure of flat lying molecules on the reactive Ag(100)-surface, the insulating KCl layer causes the adsorption in an upright standing but still commensurate manner.

References

[1] Y. Kubozono *et al.*, Phys. Chem. Chem. Phys. **13**, 16476-16493 (2011).

[2] M. Müller *et al.*, Surf. Sci. **605**, 1090-1094 (2011).

[3] M. Lackinger *et al.*, Anal. Bioanal. Chem. **87**, 685-687 (2002).

[4] T. Dienel *et al.*, Adv. Mater. **20**, 959-963 (2008).

Stoichiometry Dependent Structural Reordering Processes of PTCDA/Ag(111) upon K Intercalation

Christian Zwick, Marco Gruenewald, Roman Forker, and Torsten Fritz

Recent studies are increasingly focused on the field of doped or intercalated organic layers, since they are promising materials for novel organic electronic devices. Potassium intercalation is also known to introduce superconductivity in a variety of organic molecules [1]. However, a deeper understanding of the ongoing effects is still not achieved, especially in the case of ultrathin layered systems in the thickness regime of a monolayer or less. Therefore, PTCDA ($C_{24}H_8O_6$) adsorbed on Ag(111), presenting a very well-known model system [2,3], is used to determine the influence of intercalated potassium.

In the experiments, PTCDA monolayer domains on Ag(111) are grown under UHV conditions ($p \approx 10^{-10}\ mbar$) by thermal evaporation of the molecules onto the sputtered and annealed Ag(111), held at room temperature. Subsequently, potassium is deposited for various amounts of time. Each prepared sample is examined by LEED, to identify the intercalation stages by the contributions of the emerging structures to the diffraction pattern. To obtain highly precise lattice constants and epitaxy matrixes, the LEED images are corrected for distortions and multiple scattering effects are taken into account when analyzing using the software LEEDLab by Omicron. The novel STHM imaging mode of the Specs LT-STM, which is sensitive towards the total electron density instead of the local DOS [4,5], is applied to confirm the lattice parameters obtained by LEED and to determine the actual stoichiometry of the intercalation stages.

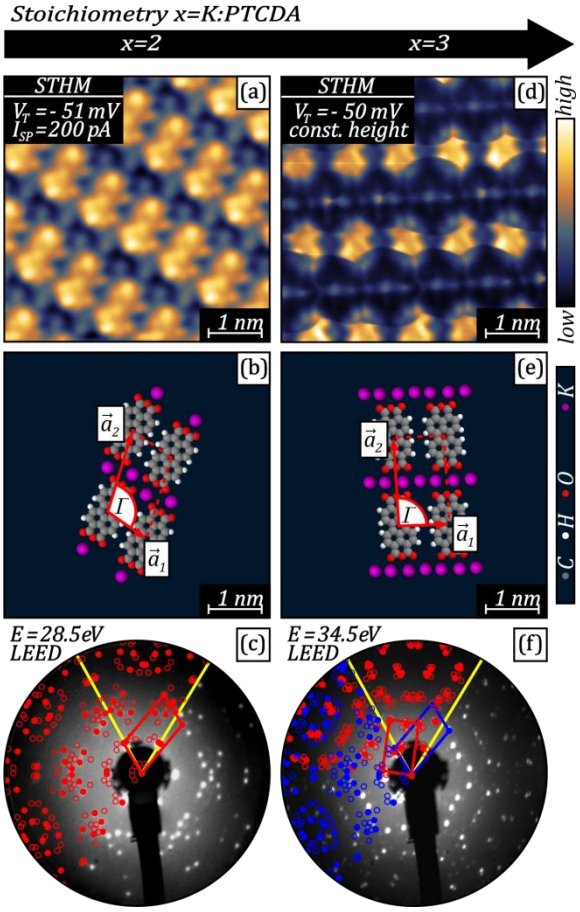

Fig. 1: *Self-assembled structures of K intercalated PTCDA/Ag(111) for the distinct stoichiometries $x = 2$ (left) and $x = 3$ (right). For each intercalation stage the measured STHM images (top), real space structural models (center) and LEED images (bottom) are shown. The STHM images are obtained for cooled samples ($T = 1.1\ K$) at the displayed tunneling parameters. The features visible arise from the simultaneous and direct imaging of PTCDA and K, displaying the lateral structure including the stoichiometry and adsorption sites of K w.r.t. PTCDA. The LEED images are obtained for cooled samples ($T = 12\ K$) at the energies displayed. The simulated reciprocal lattice and unit cell of the adsorbate (red) and substrate (yellow) are superimposed. For $x = 3$ the LEED image does not show a completed intercalation stage. Therefore it includes the simulated reciprocal lattice corresponding to $x = 2$ (blue) as well.*

First stage The first self-assembled intercalation stage is completed after doping for $8\,min$, leading to a complete conversion of the initial undoped PTCDA structure into the first intercalated phase. Evaluation of the corresponding LEED image (Fig. 1c) results in the following epitaxy matrix:

$$E = \begin{pmatrix} 3.16 \pm 0.01 & 0.16 \pm 0.01 \\ 0.98 \pm 0.01 & 6.00 \pm 0.01 \end{pmatrix}$$

representing a point-on-line (POL) epitaxy and therefore a general change in the type of epitaxy from the commensurate un-doped phase. This also includes a significant change of the lattice constants $|\overrightarrow{a_1}| = (8.98 \pm 0.01)$ Å, (decreased by ~29%), $|\overrightarrow{a_2}| = (16.04 \pm 0.02)$ Å (decreased by ~15%) and $\Gamma = (108.6 \pm 0.1)°$ (increased by 17.6 °) of the new monomolecular unit cell.

The corresponding STHM image (Fig. 1a) enables the simultaneous and direct identification of PTCDA and K, allowing to determine the actual stoichiometry as $x = \text{K:PTCDA} = 2$ and to clearify the adsorption sites of K w.r.t. PTCDA as the direct surrounding of the carboxylic oxygens. The real space model derived is shown in Fig.1b. The resulting stripe-like assembly of alternating rows of K and PTCDA seem to enable a maximum coordination of K towards the oxygens, suggesting that those K are mainly responsible for the interaction of the molecules with the dopants. Also, the disappearance of the commensurate structure may hint at a reduced hybridization, as it is a characteristic of strongly hybridized undoped PTCDA/Ag(111).

Second Stage The second self-assembled intercalation stage is completed after doping for $12\,min$, leading to a nearly complete conversion of the first K intercalated PTCDA structure into the second intercalated phase. Analyzing the corresponding LEED image (Fig. 1f) leads to the epitaxy matrix:

$$E = \begin{pmatrix} 3.55 \pm 0.01 & 3.00 \pm 0.01 \\ -2.65 \pm 0.01 & 4.00 \pm 0.01 \end{pmatrix}$$

once again indicating a POL epitaxy. However, again a significant change of the matrix entries and the lattice vectors $|\overrightarrow{a_1}| = (9.57 \pm 0.01)$ Å, $|\overrightarrow{a_2}| = (16.77 \pm 0.02)$ Å, and $\Gamma = (91.7 \pm 0.1)°$ is observed.

The STHM image (Fig. 1d) allows to determine the actual stoichiometry as $x = 3$ and to identify the adsorption sites of K towards PTCDA, which again are in the direct surrounding of the oxygens. The real space model gained is shown in Fig. 1b. The altered lattice constants indicate a shift of every second row of PTCDA along $\overrightarrow{a_1}$ for about half of its length, as it can be seen in Fig.1d and e. The resulting structure still shows a stripe-like assembly, but with a higher coordination of K towards the oxygens of PTCDA, underlining the crucial role of the interaction between K and O.

In conclusion, the main driving force for the occurring phase transitions of PTCDA/Ag(111) upon K intercalation can be determined as the attractive interaction between K and the oxygens of PTCDA, leading to a maximum coordination of O with K.

References

[1] Y. Kubozono *et al.*, Phys. Chem. Chem. Phys. **13**, 16476–16493 (2011).

[2] K. Glöckler *et al.*, Surf. Sci. **405**, 1–20 (1998).

[3] Y. Zou *et al.*, Surf. Sci. **600**, 1240–1251 (2006).

[4] C. Weiss *et al.*, Phys. Rev. Lett. **105**, 086103 (2010).

[5] R. Temirov *et al.*, New J. Phys. **10**, 053012 (2008).

Influence of potassium doping on the optical absorption of ultra-thin DBP layers on muscovite mica

Tino Kirchhübel, Marco Grünewald, Roman Forker, and Torsten Fritz

The organic dye molecule tetraphenyldibenzoperiflanthene (DBP, $C_{64}H_{36}$) consists of an aromatic backbone and four additional phenyl rings [1]. Recently, it has attracted attention for usage in optoelectronic devices due to its ability to customize the electronic structure as well as the molecular absorption and emission. As one possibility for achieving such changes we investigated the influence of controlled potassium doping on the absorption behavior of thin DBP-films on a muscovite mica substrate via differential reflectance spectroscopy (DRS).

The mica surface was cleaved *ex situ* parallel to the (0001) planes and rinsed for ~3 min in deionized water. In ultra-high vacuum the sample was degassed for 30 min at ~550 K and after cooling down to room temperature DBP molecules were deposited at a rate of ~0.06 ML/min. The growth and doping processes were controlled by means of *in situ* DRS. A detailed description can be found in refs. [2,3]. The DRS quantity is defined as the film thickness d dependent change of the sample reflectance R(E,d):

$$DRS(E,d) \equiv \frac{\Delta R}{R} := \frac{R(E,d)-R(E,d=0)}{R(E,d=0)},$$

where E denotes the photon energy. For the transparent mica substrate it describes approximately the absorption behavior of the molecular thin film.

As the interaction between DBP and the mica substrate is rather weak, fig. 1a shows the characteristic spectral fingerprint of neutral DBP molecules [1], indicated by the purple line with its distinct maxima at 2.13 eV, 2.30 eV and 2.46 eV. The low energy peak corresponds to the pure

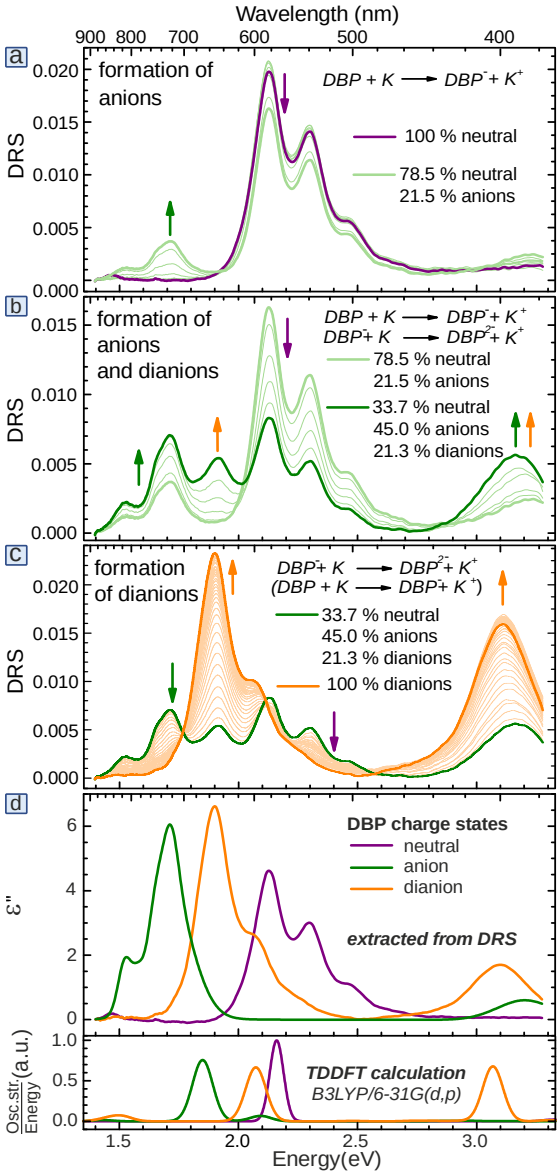

Fig. 1: (a-c) *Development of DR spectra during potassium doping of ~1.3 ML DBP on mica. The potassium concentration increases from (a) to (c) and leads to the formation of charged molecules with new absorption maxima. The dominating chemical reactions as well as the concentration of charged species for initial and final state are given.* ***(d)*** *Imaginary part of the dielectric function for charged DBP molecules and TDDFT [B3LYP/6-31G(d,p)] calculated absorption spectra.*

electronic HOMO-LUMO transition whereas the others are the result of addi-

tional vibrational excitations. When the potassium doping starts, the evolution of new features at ~1.52 eV and ~1.72 eV (light green lines) indicate the formation of DBP anions. Here the partial LUMO filling leads to new low energy transitions. As soon as ~21.5 % of the molecules have transformed into anions, a dianion formation reaction becomes significant, leading to a new feature at 1.91 eV and an increase of the broad maximum above 3 eV. When the concentration of anions (~45 %) is considerably higher than those of neutral DBP, the dianion formation becomes dominant (fig. 1c) at the expense of DBP anions. The final state is formed by a complete transformation into dianions without consecutive reactions on mica.

For each DR spectrum the imaginary part of the dielectric function $\hat{\varepsilon} = \varepsilon' - i\varepsilon''$ was extracted by a numerical algorithm (ref. [2]) and used to describe the absorption behavior of different DBP charged states as shown in fig. 1d. Considering the conservation of oscillator strength for each species the relative contribution of neutral molecules, anions and dianions was determined for every spectrum by Gaussian peak fits. The assignment of the absorption peaks is in agreement with our TDDFT calculations (fig. 1d, lower part).

Similar to the considerations in ref. [4] the two chemical reactions can be modeled by the following rate equations:

$$\frac{d}{dt}C_0(t) = -P_1 C_0(t) C_K(t)$$
$$\frac{d}{dt}C_1(t) = [P_1 C_0(t) - P_2 C_1(t)]\, C_K(t)$$
$$\frac{d}{dt}C_2(t) = P_2 C_1(t) C_K(t)\,,$$

where C_i denotes the concentration of DBP molecules with charge $-i \cdot e$, while P_1 and P_2 are the anion and dianion formation probabilities respectively. The concentration of neutral potassium atoms was approximated by the expression:

$$C_K(t) = \lambda_K t - C_1(t) - C_2(t)\,,$$

with a constant rate of potassium increase λ_K. By numerical solution of this equation system and fitting to the experimental data the ratio $P_1 : P_2$ is determined as 1.3 : 1. In this case the calculated development of the composition of the molecular film is in accordance with our experimental data (fig. 2), indicating that the assumption of two chemical reactions is a good approximation for the doping process of DBP on mica.

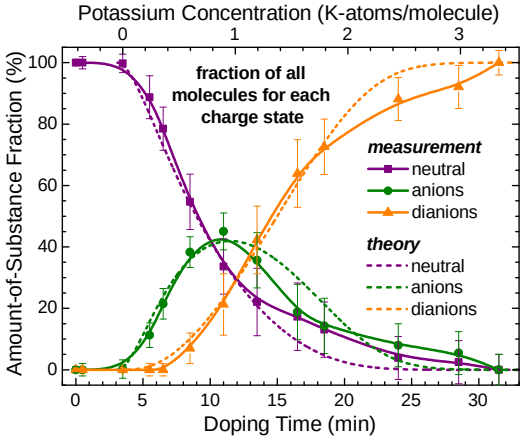

Fig. 2: *Development of the different molecular charge states during potassium doping of 1.3 ML DBP on mica over time in comparison with the numerically solved rate equations.*

The present work shows that potassium doping of DBP up to a dianion state is possible and allows us to customize the molecular absorption and emission over a wide range of the visible spectral region.

References

[1] J. D. Debad *et al.*, J. Am. Chem. Soc. **118**, 2374-2379 (1996).

[2] R. Forker et al., Annu. Rep. Prog. Chem., Sect. C: Phys. Chem. **108**, 34-68 (2012).

[3] R. Forker and T. Fritz, Phys. Chem. Chem. Phys. **11**, 2142-2155 (2009).

[4] T. Dienel et al., Adv.Mater. **22**, 4064–4070 (2010).

Gate Modulation of below-band-gap Photoconductivity in ZnO Nanowire Field-Effect-Transistors

Davide Cammi, Robert Röder and Carsten Ronning.

Nanowire-based field effect transistors (NWFETs) have been intensively investigated in the last decade, in particular for applications in nano-electronics, opto-electronics, gas and bio-sensing [1]. Due to the intrinsic n-type conductivity, the wide direct band gap at around 3.4 eV and the high UV sensitivity, ZnO nanowires are promising candidates as a semiconducting channel in electric circuits for UV photo-detectors [2]. However, defect states located in the band gap can alter the photo-response of the device and affecting the photo-detection performance. An accurate characterization of their properties is therefore required. In this study, we report on the investigation of the photo-conductivity properties of ZnO NWFETs under below-band-gap excitation as a function of the gate voltage.

The nanowires were grown by the VLS [3] method and subsequently transferred to a new substrate (850 nm of SiO_2 on Si). After photolithography and metal deposition, the final devices consist of some nanowires bridging two Ti/Au electrodes (10nm/100nm). The samples were then glued on a commercial chip carrier and contacted by electrical bonding. The electrical measurements were carried out with a Source-Measure Unit (SMU) Keithley (Model 237) applying a voltage difference between the drain and the source electrodes. The gate voltage V_{gs} was applied by using an additional voltage generator and a Xenon Lamp with 200 mm monochromator was used as a light source for the photo-conductivity investigation.

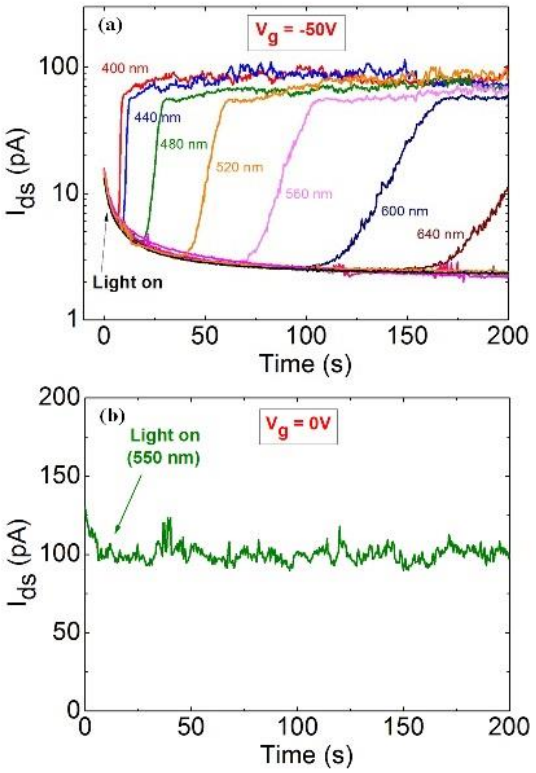

Fig. 1: *(a) I_{ds} as a function of the time under below-band-gap excitation in the range 400-800 nm in a ZnO NWFET with V_{gs} = -50 V. The device does not show any response under photo-excitation at wavelength longer than 640 nm. A reference measurement under excitation at 550 nm with V_{gs} = 0 V is shown in (b). In this case the current does not increase.*

The response of the device under light excitation in the range 400 - 800 nm with V_{gs} = -50 V is shown in figure 1(a). In the investigated temporal interval of 200 s we did not observe any increase of the drain-source current with exciting wavelength longer than 640 nm. Only when the wavelength becomes shorter than 640 nm an onset of the photo-current increase appears. A reference measurement performed under light excitation at 550 nm

shows that the current does not change when V_{gs} = 0 V (figure 1(b)).

Micro-PL measurements (μPL) were then performed on the same device, exciting the nanowire with a He-Cd laser at 325 nm in air at room temperature. The spectra measured at V_{gs} = 0V, immediately after switching to V_{gs} = -50 V and after 1 and 2 min are shown in figure 2. The change in the gate voltage does not induce any change to the deep-level emission, typically related to defect levels located in the band-gap of ZnO [4,5]. The result of the μPL measurements seems to indicate that the change in the gate voltage does not induce any appreciable variation in the population of defect levels located in the nanowire volume.

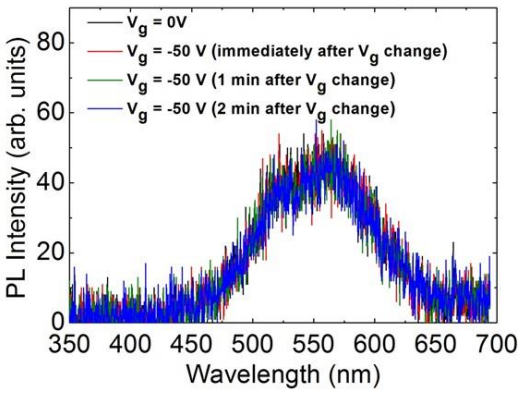

Fig. 2: *μPL spectra of the single ZnO NWFET shown in figure 1 in the spectral region of the deep-level-emission, at V_{gs} = 0 V and V_{gs} = -50 V. The change of the gate voltage does not induce any appreciable change in the defect-related emission, which is dominating the spectra.*

The possible contribution from localized states located at the the interface between the nanowire and the SiO_2 is investigating by considering the influence of a gate bias conditioning on the transconductance characteristics (I_{ds}-V_{gs}) of the device. In figure 3 we present three (I_{ds}-V_{gs}) measurements on the same device, measured before gate bias conditioning, after leaving the device for 1 hour at V_{gs} = -50 V, and after 1 hour at V_{gs} = +50 V. A positive gate bias conditioning induces a clear shift of the threshold voltage towards positive values of V_{gs}, while after a negative bias the threshold voltage shifts towards negative values. This suggests that a positive gate bias conditioning accumulates electron at the interface defect levels, while a negative bias conditioning force electrons to leave such levels.

According to these results, we can interpret the observed below band gap photoconductivity properties with V_{gs} =-50 V as light-assisted escape of electrons from defect levels located between the ZnO nanowire and the gate dielectric SiO_2.

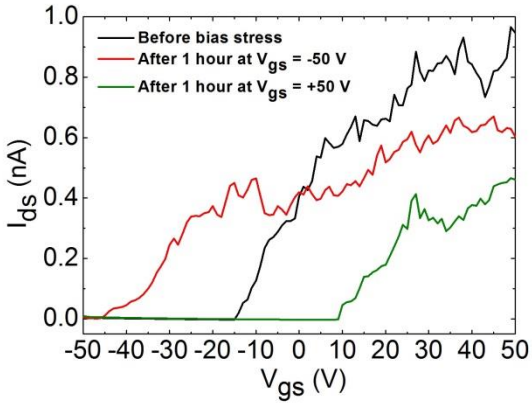

Fig. 3: *Transconductance characteristics (I_{ds} – V_{gs}) before and after two gate bias conditioning procedures at V_{gs} = -50 V and V_{gs} = +50 V. A corresponding shift of the threshold voltage is evident.*

References

[1] Y. Cui and C. M. Lieber, Science **291** 851-853 (2001).

[2] C. Soci *et al.*, 2007 Nano Lett. **7** 1003-1009 (2007).

[3] C. Borschers *et al.*, J. Phys. Chem. B **110**, 1656-1660 (2006).

[4] S. H. Jeong *et al.*, Appl. Phys. Lett. **82** 2625-2627 (2003).

[5] Shan F K *et al.*, J. Appl. Phys. **101** 053106 (2007)

Bond stretching force constant in GaP

Stefanie Eckner, Martin Gnauck, Andreas Johannes, Helena Kämmer, Mark C. Ridgway, Claudia S. Schnohr*

**Department of Electronic Materials Engineering, Research School of Physics and Engineering, The Australian National University, Canberra ACT 0200, Australia*

Compound semiconductors are the fundament of ground-breaking achievements in electronics and optoelectronics. Especially III-V semiconductors offer already today a broad range of technological applications. Nevertheless some of their properties are still not fully understood.

One central property of the material is the force constant for stretching and compressing the interatomic bonds. It determines not only the atomic scale structure of semiconductor alloys and strained nanostructures but also the vibrational behaviour of the atoms.

Therefore the vibrational properties of GaP were studied using temperature dependent extended x-ray absorption fine structure spectroscopy (EXAFS). EXAFS measures the element specific interatomic distance distribution, which can be characterised by the average value, the variance and higher order cumulants.

Measurements of the Ga K edge at ten different temperatures ranging from 20 K to 300 K were performed in transmission mode at Beamline C of HASYLAB (DESY) in Hamburg. Data processing and analysis were performed utilizing a specifically written software based on the program package Larch [1]. Theoretical phase shifts and scattering amplitudes were calculated using FEFF9 [2].

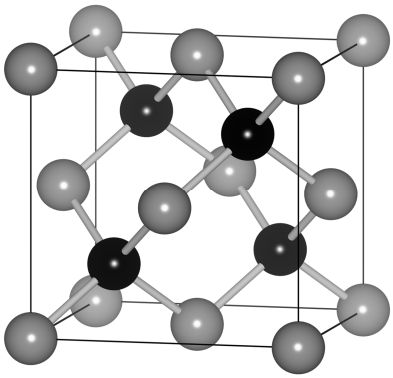

Fig. 1: *Schematic of the zinc blende structure.*

A model based on the zinc blende structure depicted in Fig. 1 and including all single and multiple scattering paths with a half-path-length up to 8 Å was fitted to the recorded spectra. The first three single scattering paths were modelled with one set of parameters each, while all other scattering paths were parameterized via geometric considerations. The coordination number was fixed whereas the amplitude reduction factor S_0^2 and the threshold energy E_0 were left free.

The thus determined variance of the first nearest neighbour (1NN) distance distribution (σ^2) is plotted as a function of temperature in Fig. 2. The error bars plotted represent the fitting uncertainties.

The variance increases considerably with increasing temperature. The reason is the increase of vibrations of atoms relative to each other which cause a larger variation of interatomic distances for higher temperatures.

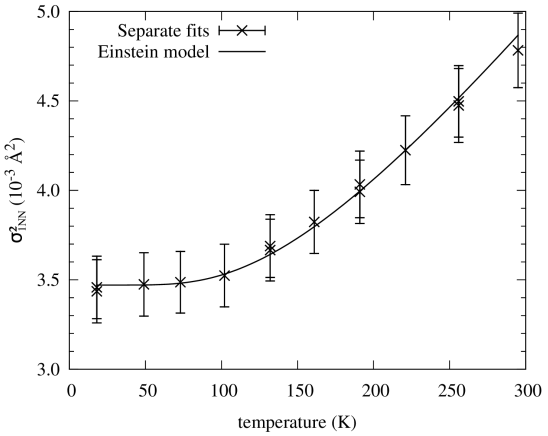

Fig. 2: *Variance of the first nearest neighbour distance distribution σ^2_{1NN} as a function of temperature. Symbols represent individual fits. The line corresponds to an Einstein model with Einstein temperature 450 K and a static contribution of 9 × 10^{-4} Å^2.*

The temperature dependence of atomic vibrations was modelled using a simple Einstein model, describing the bonds with a bond stretching force constant corresponding to an Einstein temperature. Static disorder was covered by an additive constant. A value of 450 ± 10 K for the Einstein temperature and (9 ± 1) x 10^{-4} Å^2 for the static term was determined in a fit. The resulting curve is plotted in Fig. 2 and agrees very well with the data. The variances of the second and third nearest neighbour distance distributions show a similar temperature dependence and are similarly well described by the Einstein model.

The Einstein temperature of 450 ± 10 K for the 1NN distance distribution in GaP is higher than the known values of 392 ± 8 K [3] and 331 ± 4 K [4] for InP and GaAs, respectively, meaning the Ga-P bond is stiffer than both the In-P and Ga-As bond. It is known from other tetrahedrally coordinated systems, that a stiffer bond corresponds to a shorter bond length [5,6]. By exchanging the Ga of the Ga-P bond with In the bond elongates, which is seen as an increase of the lattice constant from 5.45 Å (GaP) to 5.87 Å (InP) [7]. Similarly the exchange of the P of the Ga-P bond with As induces an increase of the lattice constant to 5.65 Å (GaAs) [7]. So in both cases the elongation of the bond is accompanied by a decrease of the bond stiffness.

The Einstein temperature of 450 ± 10 K corresponds to a bond stretching force constant of 124 N/m for the Ga-P bond in GaP. An accurate knowledge of the bond stretching force constants is crucial for numerical simulations of strained systems and nanostructures. In addition, the detailed comprehension of vibrational properties can improve the analysis of Raman and IR spectra.

References

[1] M. Newville, *http://cars.uchicago.edu/xraylarch*.
[2] J.J. Rehr *et al.*, Phys. Chem. Chem. Phys. **12**, 5503 (2010).
[3] C.S. Schnohr *et al.*, Phys. Rev. B **79**, 195203 (2009).
[4] S.I. Ahmed *et al.*, J. Chem. Phys. **139**, 164512 (2013).
[5] L. Artus and J. Pascual, J. Phys.: Condens. Matter **4**, 5835-5844 (1992).
[6] A.S. Verma, Solid State Comm. **149**, 1236-1239 (2009).
[7] S. Adachi, *Properties of Group IV, III-V and II-VI Semiconductors*, Wiley, NewYork (2005).

Electroluminescence of Eu ions implanted single ZnO nanowires

Y. Haj Hmeidi, M. Riediger, R. Röder, D. Cammi, and C. Ronning

Zinc oxide (ZnO) is a wide band gap (3.37 eV at RT) semiconductor with a large exciton binding energy of 60 meV at RT [1]. Therefore, it is a good candidate to host rare earth ions, which exhibiting intra-shell transitions in the visible and infrared emission. And indeed recent photoluminescence studies of Eu ions implanted single ZnO (NWs) reveal intense emission lines of intra-4f transitions at RT [2]. As consequence next step, electrically driven light emission of RE implanted single ZnO NWs may lead to pioneer optoelectronic devices such as single photon emitters. Although electroluminescence of RE doped ZnO bulk systems have been achieved by applying DC voltage or AC voltage [3-6], the electroluminescence of RE implanted single ZnO nanowires is still a challenging task. In this work, we propose a new approach for EL devices based on Eu ion implanted single ZnO nanowire.

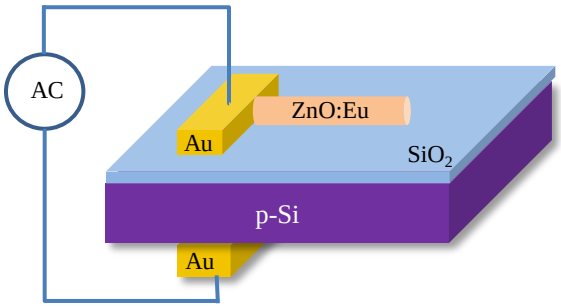

Fig. 1: *Schematic diagram of final device structure.*

Zinc oxide nanowires were grown via vapor transport enabled by the VLS mechanism in horizontal furnace. The NWs ensemble were subsequently implanted with a fluence of $\Phi = 2\times10^{15}cm^{-3}$ with an ion energy of 200 keV. The Eu ions implanted ZnO nanowires were annealed for 120 minutes at 700° C in air in order to remove irradiation damage and create Eu-O_i complexes [2]. Finally, the implanted ZnO nanowires were imprinted directly on samples, on which beforehand photolithography was used to define contacts pads with thickness of 10 nm Ti / 100 nm Au. The final device structure is based on an additional isolating layer SiO_2 between the implanted single ZnO nanowires and the bottom electrode, resulting in a capacitor like architecture as it is shown in figure 1.
Electroluminescence (EL) measurements were performed using a microphotoluminescence set up, which is described in reference [10]. An AC voltage was applied to the final device, as it is illustrated in figure 1. The implanted ZnO nanowires show EL at RT by applying an AC voltage sinusoidal wave with voltages in the range of 10-15 V (peak to peak value), and frequencies in the range of 10.5-16.5 MHz. The observed EL occurs at exactly the interface between the implanted nanowire and the contact pad, as it is shown in the optical microscope picture shown in Fig. 2.

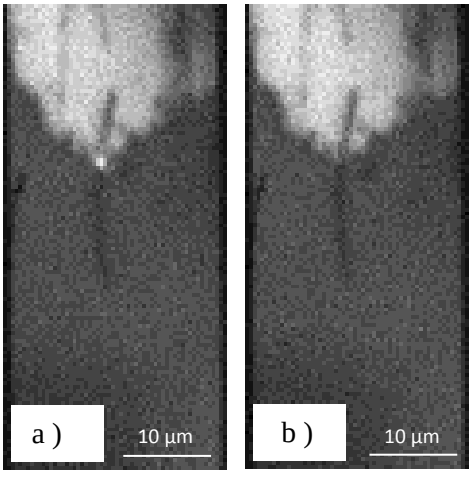

Fig. 2: *a) CCD image of EL at f=16.5 MHz, V_{pp} = 10 V, at RT. b) Reference optical image.*

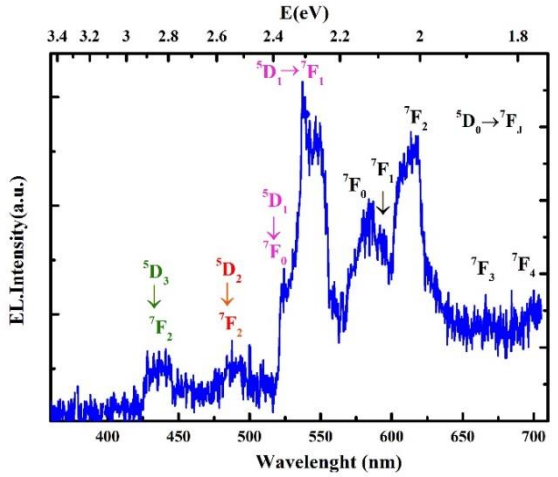

Fig. 3: *Room temperature EL spectrum of ZnO:Eu nanowires at f=16.5 MHz, V_{pp} = 10 V.*

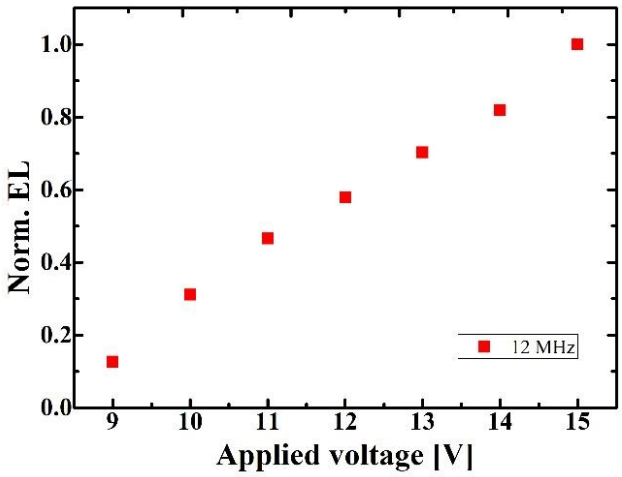

Fig. 4: *Room temperature EL as function of applied AC voltage, while the frequency was kept constant at 12 MHz.*

The EL spectrum of the same nanowire is shown in figure 3. The observed EL is attributed to 4f-intrashell transitions of Eu ions, which are labeled according to literature [2-9]. The EL of Eu ions, which are trivalent charged in ZnO, proves the success of ion implantation as a powerful method to dope the ZnO nanowires using optically activated centers and subsequent thermal annealing. The Eu ions are electrically excited, and since there is no EL observed from ZnO of near band gap tranistions, the suggested mechanism of excitation is direct-impact ionization of luminescence centers by hot electrons injected from the gold electrode. The EL increases linearly with increasing voltage up to 15 V at a constant frequency, as it is shown in figure 4.

In summary, we report on electroluminescence of Eu ions implanted single ZnO at room temperature. The most likely mechanism is direct-impact ionization by hot electrons. This approach is simple and applicable also to another RE elements in ZnO nanowires and opens therefore wide range of possibilities for optoelectronic applications based on ZnO nanowires.

References

[1] S. Liu, et al., Adv. Mater. **21**, 1217 (2009).

[2] S. Geburt, *et al.*, Nano Letters **14**, 4523 (2014).

[3] S. Iwan, *et al.* Materials Science in Semiconductor Processing **30**, 263 (2015).

[4] S. Bachir, C. Sandouly, J. Kossanyi, and J. C. Ronfard-Haret, J. Phys. Chem. Solids **57**, 1869 (1996).

[5] S.A.M. Lima, *et al.*, Applied Physics Letters **90**, 023503 (2007).

[6] Yang, *et al.*, Adv. Optical Mater. **2**, 240 (2014).

[7] Wang, *et al.*, J. Phys. Chem. C **115**, 22729 (2011).

[8] Chen, *et al.*, Journal of Alloys and Compounds **431**, 317 (2007).

[9] U. Vetter, PhD Thesis, University of Göttingen (2003).

[10] S. Geburt, PhD Thesis, FSU Jena (2012).

Composition-dependent atomic-scale structure of the Cu-(In,Ga)-Se system

Erik Haubold, Philipp Schöppe, Stefanie Eckner, Susan Schorr[1], Francesco di Benedetto[2], Ivan Colantoni[3], Francesco d'Acapito[3], Claudia S. Schnohr

[1] Helmholtz-Zentrum Berlin für Materialien und Energie, Hahn-Meitner-Platz 1, 14109 Berlin, Germany & Institut für Geologische Wissenschaften, Freie Universität Berlin, Malteserstr. 74-100, 12249 Berlin, Germany
[2] Dipartimento di Scienze della Terra, Università degli Studi di Firenze, Via La Pira 4, 50121 Firenze, Italy
[3] CNR-IOM-OGG c/o ESRF LISA CRG, 71 Avenue des Martyrs, 38000 Grenoble, France

$Cu(In,Ga)Se_2$ shows the highest conversion efficiencies of all thin film solar cells with more than 20%. It is believed that the formation of copper poor surface regions within the absorber is important for reaching these high efficiencies. However, the properties of the material, including the band gap energy, are determined not only by the material composition but also by the local arrangement of the atoms [1,2]. Therefore, we studied the atomic-scale structure of $Cu(In,Ga)Se_2$ (1-1-2 phase, $0.8 \leq Cu/III = Cu/(In+Ga) \leq 1.0$) and the two copper poor phases $Cu(In,Ga)_3Se_5$ (1-3-5) and $Cu(In,Ga)_5Se_8$ (1-5-8) as a function of the In/III = In/(In+Ga) ratio using extended X-ray absorption fine structure spectroscopy (EXAFS) at low temperatures. EXAFS yields the *element-specific* average bond lengths and bond length variations thus providing structural information highly complementary to that obtained by diffraction techniques which yield the long-range crystallographic structure of the material.

The 1-1-2 phase is well known and can be described with a chalcopyrite type crystal structure (space group $I\bar{4}2d$). This structure is derived from the zinc blende structure by populating the cation positions with copper and group-III atoms in an ordered manner as shown schematically in Fig. 1. In comparison, the crystal structure of the copper poor 1-3-5 and 1-5-8 phases has been strongly discussed [3,4]. One proposed structure is the stannite type crystal structure (space group $I\bar{4}2m$) shown in Fig. 1. It also is a tetrahedrally coordinated structure where every cation has four selenium neighbors. This directly requires the presence of vacancies in the copper poor phases. Furthermore, the stannite structure has three instead of two crystallographic cation positions, the population of which varies in different reports [4]. Despite these differences the local coordination remains similar for each cation and it is the aim of this EXAFS study to assess whether the atomic-scale structural parameters differ for the different phases.

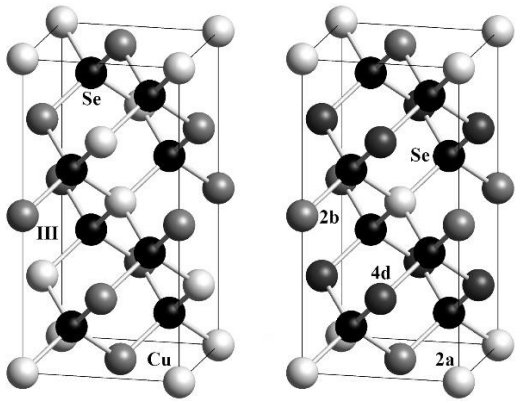

Fig. 1: *Schematic of the chalcopyrite ($I\bar{4}2d$, left) and stannite ($I\bar{4}2m$, right) type crystal structure of the Cu-(In,Ga)-Se system.*

The samples were synthesized at the Helmholtz-Zentrum Berlin in a solid state reaction from the pure elements. The powders were diluted with boron nitride or cellulose and then filled into suitable sample holders or pressed into pellets. The 1-1-2 phase was previously measured at Beamline C of HASYLAB (DESY) in Hamburg at approximately 20 K [1,5]. The 1-3-5 and 1-5-8 phase were measured at the GILDA Beamline BM08 of the ESRF in Grenoble at approximately 100 K. In all cases, the copper, gallium and indium K edges were investigated.

Data processing and analysis were performed using IFEFFIT [6] and the corresponding user interface ATHENA [7]. Theoretical phase shifts and scattering amplitudes were calculated with FEFF9 [8]. A simple structural model, considering only the first nearest neighbor shell consisting of four selenium atoms, was used. This yields in the Cu-Se, Ga-Se and In-Se average bond lengths and bond length variations.

As an example, Fig. 2 shows the Cu-Se bond length as a function of the In/III ratio for all three phases. For the 1-1-2 phase, there is a small increase in the bond length with increasing In/III content [1,5]. For both copper poor phases, a similar increase of the bond lengths can be observed. Comparing the different phases, a small yet clear increase of the bond lengths is visible with decreasing copper content. Similar findings were previously reported for the pure Cu-In-Se system [9,10]. The results of this work now clearly show that this behavior is independent of the indium or gallium content and that the change of the Cu-Se bond length as a function of the In/III ratio is very similar for all three phases. Together with the results obtained for the Ga-Se and In-Se bond lengths, these findings draw a comprehensive picture of the relationship between the local structural parameters and the material composition for different phases of the important Cu-(In,Ga)-Se system.

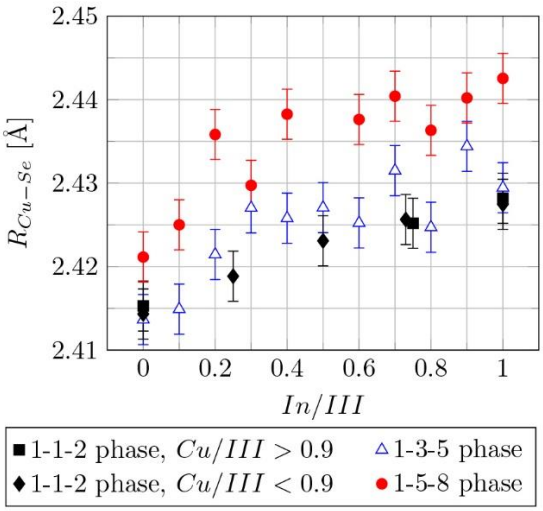

Fig. 2: *Cu-Se bond length as a function of the In/III ratio for the 1-1-2, 1-3-5 and 1-5-8 phase of the Cu-(In,Ga)-Se system. The data collected at HASYLAB has been adjusted to a measurement temperature of 100 K.*

References

[1] C.S. Schnohr *et al.*, Phys. Rev. B. **85**, 245204 (2012).

[2] S. Eckner *et al.*, Appl. Phys. Lett. **103**, 081905 (2013).

[3] T. Hanada *et al.*, Jpn. J. Appl. Phys. **36**, 1494-1497 (1997).

[4] S. Lehmann *et al.*, J. Appl. Phys. **109**, 013518 (2011).

[5] C.S. Schnohr *et al.*, Thin Solid Films, *in press*. doi: 10.1016/j.tsf.2014.10.078.

[6] M. Newville, J. Synchrotron Rad. **8**, 322-324 (2001).

[7] B. Ravel and M. Newville, J. Synchrotron Rad. **12**, 537-541 (2005).

[8] J.J. Rehr *et al.*, Phys. Chem. Chem. Phys. **12**, 5503-5513 (2010).

[9] J.M. Merino *et al.*, Thin Solid Films **480-481**, 295-300 (2005).

[10] S. Yamazoe *et al.*, J. Mater. Res. **12**, 1504-1516 (2011).

High temperature sequential CIGSe deposition

M. Oertel, S. Schönherr, Ph. Schöppe, C.S. Schnohr, U. Reislöhner, C. Ronning

On laboratory scale Cu(In,Ga)Se_2 (CIGSe) thin film solar cells have impressively proven their capability for high efficiencies in the recent past.[1] These high efficient cells were produced by co-evaporation. Unfortunately, the co-evaporation process is difficult to scale up, has a low throughput and high material consumption. Therefore, sequential processes are more favored in mass production,[2] but show typically lower efficiencies, mainly due to very low gallium content in the space charge region and therefore lower open circuit voltages. To overcome this issue, higher process temperatures could be a solution.[3] To this end, we developed a high temperature sequential process and compared the results with our standard temperature process.

The metallic CuGa/In multilayer stack (precursor) were deposited on a molybdenum coated soda lime glass by dc-magnetron sputtering with the exactly same parameters for all samples. The overall Ga/(Ga+In) ratio was around 0.35, where the Cu/(Ga+In) ratio was around 0.9. To resist the higher process temperature during the following selenization the high temperature samples were prepared on an experimental high temperature stable glass made by Schott whereas the standard temperature sample were prepared on commercial Pilkington OptiWhite glass. Both glasses have nearly the same sodium content as well as the same thermal expansion coefficient. After the precursor deposition the samples were reactively annealed in a high vacuum system where the reactive elemental selenium atmosphere were produced by a Knudsen-type evaporation source. The heater temperature profiles during the selenization are shown in Fig. 1.

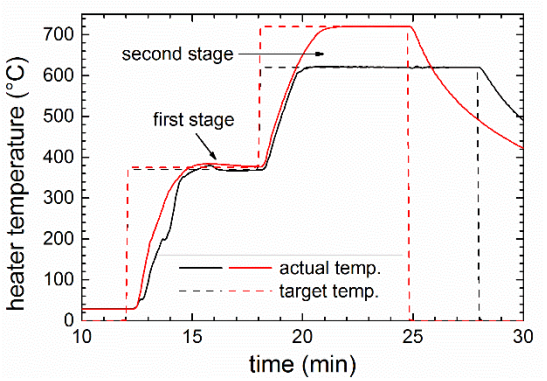

Fig. 1: *Representative heater temperature profiles of the standard (black) and the high temperature process (red).*

As one can see, the second stage heater temperature is increased from 620°C to 720°C for the high temperature process. The corresponding substrate temperature is around 360 °C in the first stage and around 530°C and 620°C in the respective second stage. In the standard temperature process a selenium rate of 200 nm/min were supplied in the whole process, while in the high temperature process the selenium rate was increased to 250 nm/min in the second stage. The adaption of the selenium supply and the dwell time (Fig. 1) are necessary to prevent elemental losses and a too strong back contact selenization at higher temperatures. The prepared CIGSe absorbers were processed to solar cells according to Ref. [4].

A comparison of representative j-V-curves of cells of the standard and the high temperature process is shown in Fig. 2.

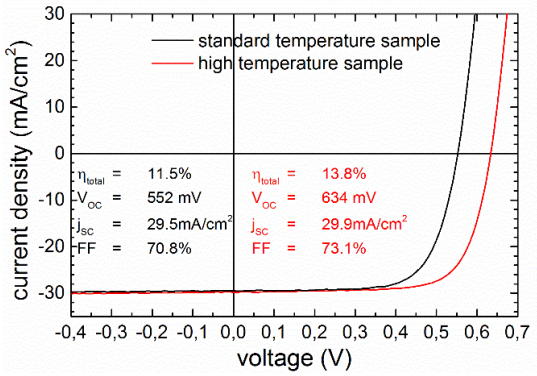

Fig. 1: *Comparison of representative j-V-curves of cells of the standard and the high temperature process. Electrical values are given in the graph in the corresponding color.*

As a remarkable result the open circuit voltage of the high temperature cell is around 80 mV higher than the value of the standard processed cell. Because both cells have comparable resistances the increase of the open circuit voltage increases also the fill factor of the high temperature processed cell. Both changes increase the efficiency by 2 % absolute. A nearly similar increase in the open circuit voltage was also reported by Haarstrich et al.[3] for co-evaporated CIGSe cells deposited at nearly the same temperature. A higher open circuit voltage is typically caused by a larger bandgap at the p-n-junction. So measurements of the external quantum efficiency (EQE) were done to check for differences of the absorption of the different processed absorbers. The results are shown in Fig. 3.

The EQE of the standard temperature sample shows a significant larger current generation in the wavelength region between 1050 and 1200 nm. This strongly indicates a smaller bandgap. Because the overall composition of both samples is the same, the in depth gallium profile must be more homogenous in the high temperature absorber to get the higher bandgap at the p-n-junction. Additionally, the slope of the EQE at the long wavelength edge is steeper for the high temperature sample which means the sample has a better current collection and less bulk defects.

As it was shown, a selenization at higher temperatures requires several other process adaptions beside. But it significantly increases the efficiency of CIGSe thin film solar cells mainly by increasing the open circuit voltage by a homogenization of the gallium profile in the absorber layer.

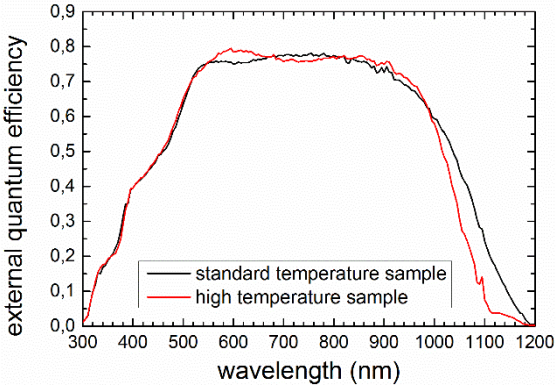

Fig. 1: *EQE of solar cells processed at different heater temperature.*

Acknowledgement

We acknowledge gratefully the BMWi for financial support within the “comCIGS II” project under support code 0325448E.

References

[1] P. Jackson *et al.*, Phys. Status Solidi RRL **8,** 219 (2014).

[2] S. Niki *et al.*, Prog. Photovolt. Res. Appl. **18**, 453-466 (2010)

[3] J. Haarstrich *et al.*, Sol. Energy Mater. Sol. Cells **95,** 1028–1030 (2011).

[4] M.Oertel, Ph.D. thesis, Friedrich-Schiller-Universität Jena, Germany. Available: http://www.db-thueringen.de/servlets/DocumentServlet?id=20642.

Cathodoluminescence on lamellae of CIGSe solar cells

A.E. Anthony, S. Schönherr, Ph. Schöppe, M. Oertel, U. Reislöhner, and C. Ronning

CIGSe solar cells were prepared by a sequential process, where a stack of metallic Cu-Ga-In layers is selenized to the $Cu(In,Ga)Se_2$-absorber. Typically, the Ga-concentration increases towards the back contact in this kind of process. An increase of the Ga content causes an increase in the bandgap by mainly shifting the position of the conduction band minimum [1] and thus strongly influences the functionality of the solar cell.

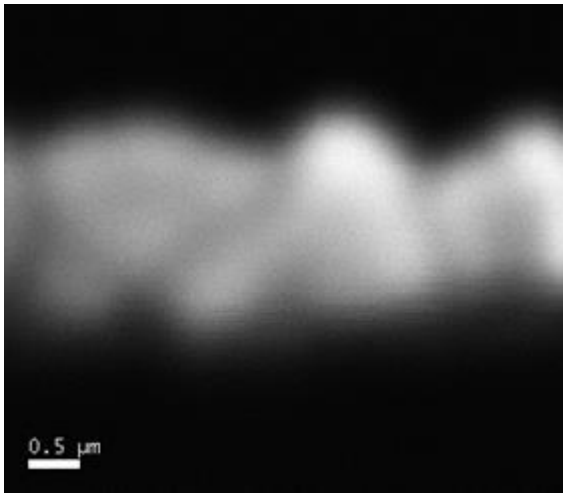

Fig. 1: *The lamella shows an intense polychromatic luminescence, which reveals the grain structure. The back contact side is below the bright region, the pn-junction is above.*

Cathodoluminescence (CL) on lamellae is suited very well for characterizing the CIGS-absorbers, because the luminescence reveals also information on lateral inhomogeneity, which may correlate with the grain structure [2]. The lamellae were prepared as a cross section from a completely processed solar cell using our focused ion beam system. With a typical thickness of only 250 nm, it was possible to perform EDX (energy dispersive x-ray spectroscopy), CL and STEM (scanning transmission electron microscopy) at the identical lamellae with a high lateral spatial resolution of about 100 nm for EDX. This high resolution results from the small excitation volume which here almost only depends on the diameter of the electron beam. In contrast to the rough surfaces of cleaved cross-sections the lamellae possess very smooth surfaces and the CL intensity is thus not influenced by geometry effects due to the surface morphology but clearly reveals the underlying grain structure as shown in figure 1 and in more detail in reference [2]. The CL measurements were performed at T=10 K with an electron energy of 10 keV.

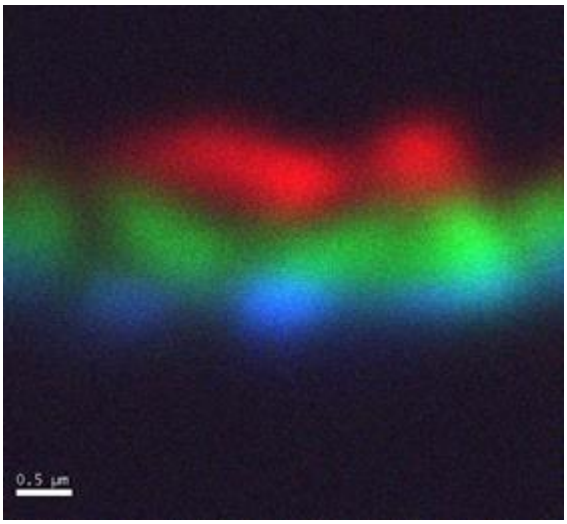

Fig. 2: *Monochromatic CL-measurements performed at wavelengths of 1050 nm (blue), 1090 nm (green), and 1200 nm (red). The back contact side is below the blue region, the pn-junction is above the red one.*

The monochromatic CL-measurements in figure 2 clearly show a decrease of the wavelength from the pn-junction to the back contact, which is equivalent to an increase of the band gap energy towards the back contact.

CL-spectra taken near the contacts (fig. 3) reveal this energy shift in more detail, as shown in figure 4. The shift of the luminescence energy ΔE_{CL} equals 82 meV and is very close to the bandgap shift ΔE_{gap}=90 meV due to the change in the Ga-concentration. The bandgap energy was calculated from the Ga-concentration [3], which was measured by EDX (energy dispersive x-ray spectroscopy) at the same lamella. This result shows that the increased Ga content towards the back contact, which is detected by pure elemental analysis, is mainly integrated within the Cu(In,Ga)Se_2-lattice and does not lead to a Ga-enrichment of grain boundaries or to Ga-inclusions, because grain boundaries or Ga-inclusions do not contribute to the observed CL-luminescence.

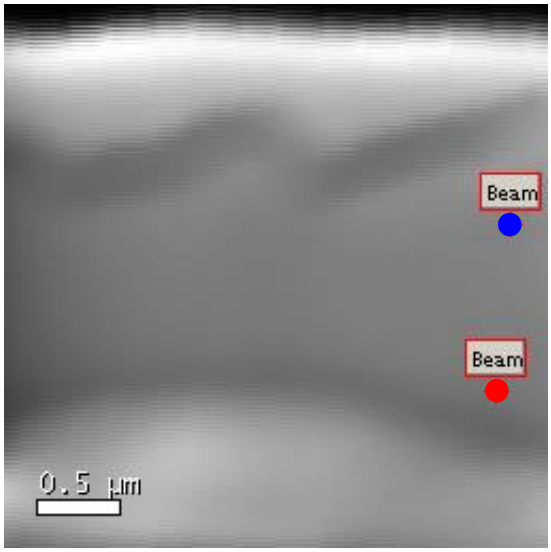

Fig. 3: *The SEM-image indicates the locations where the spectra were taken that are shown in figure 4.*

The small difference between ΔE_{CL} and ΔE_{gap} is assumed to be caused by a charging process of the lamella which led to small deflections of the electron beam. These charging effects are now suppressed by coating the lamella on both sides with a thin conductive carbon layer.

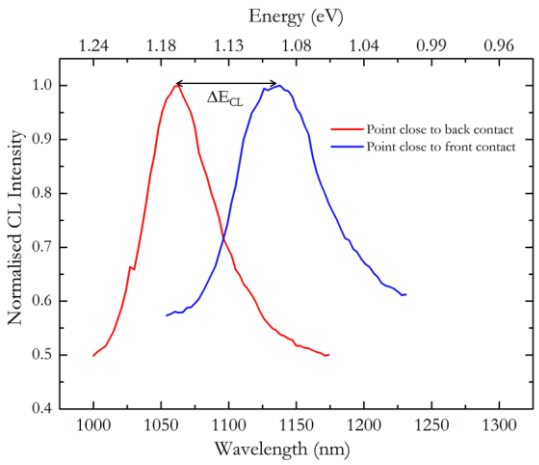

Fig. 4: *CL-spectra taken at locations near the pn-junction and the back contact as shown in figure 3. The energy shift* ΔE_{CL} *is caused by a shift of the band gap energy due to a different Ga-concentration.*

Summarizing, we demonstrated the possibility of performing CL-analysis on thin lamellae. This technique enabled CL-analysis with a high spatial resolution in contrast to measurements at cleaved cross-sections. While polychromatic luminescence mainly reflects the grain structure, monochromatic luminescence clearly shows the shift of band gap energy due to an increase of the Ga-concentration towards the back contact.

Acknowledgement

We acknowledge gratefully the BMWi for financial support within the “comCIGS II” project under support code 0325448E.

References

[1] T. Dullweber *et al.*, Solar Energy Materials and Solar Cells, **67**, 145-150 (2001).

[2] S. Schönherr *et al.*, Photovoltaic Specialist Conference (PVSC), 2014 IEEE 40th, 1699-1703 (2014).

[3] Dullweber *et al.*, IEEE Trans Electron Dev, **47**, 2249-2254 (2000)

Spectrally resolved polarization properties of lasing ZnO nanowires

Max Riediger, Robert Röder, Daniel Ploss[1], Ulf Peschel[2] and Carsten Ronning

[1] *Institute of Optics, Information and Photonics, Universität Erlangen-Nürnberg*
[2] *Institute of Condensed Matter Theory and Solid State Optics, Universität Jena*

Semiconductor nanowires (NWs) are potential nanoscale light sources for overcoming the limits of electronic circuitry by on-chip optical data transmission and processing. High quality ZnO NWs with a band gap of 3.4 eV and excellent waveguide properties act as Fabry-Pérot (FP) resonators, exhibiting ultraviolet lasing emission around 385 nm at room-temperature [1]. Since optical processing is specified by the direct emission of a lasing device, a setup, shown in Fig. 1 (a), was developed to investigate the polarization properties of the NW emission by measuring its Stokes parameters.

The four Stokes parameters S_0 to S_3 describe the polarization of a light source in terms of intensities [2]. If the light source is partially polarized, a degree of polarization P can be determined: $P = (S_1^2 + S_2^2 + S_3^2)^{1/2} / S_0$ [3].

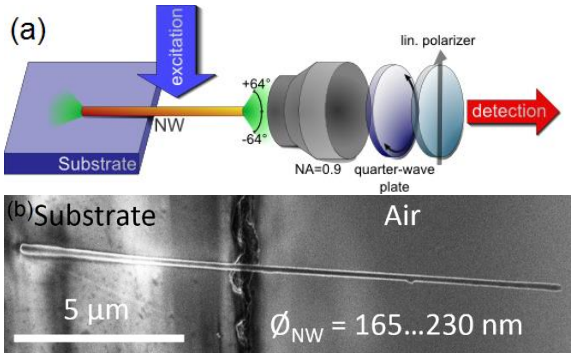

Fig. 1: *(a) Setup for Stokes-measurement of the end facet emission of a single NW. (b) ZnO NW with a length of 16.1 µm and a diameter between 165 and 230 nm lying on the edge of a MgF_2 substrate.*

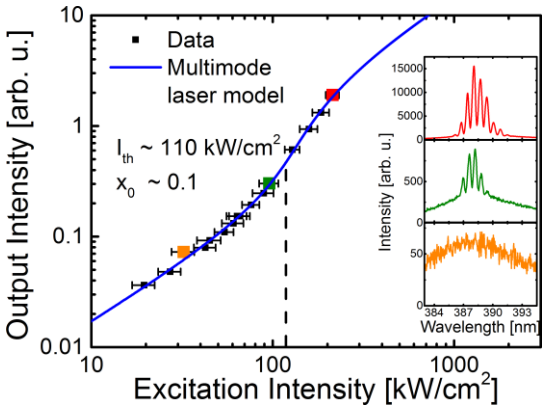

Fig. 2: *Power dependence of the NW output intensity on the excitation intensity shows a multimode laser behavior. The inset shows the corresponding emission spectra below, at and over the laser threshold.*

Investigations of the optical emission properties were carried out. The 16.1 µm long ZnO NW with diameters ranging from 165 to 230 nm, depicted in Fig. 1 (b), was pumped by a frequency tripled Nd:YAG laser at 355 nm. The luminescence emitted out of the end facet was collected by an objective and spectrally detected with the help of a monochromator. The power dependence of the NW output intensity on the pump intensity is shown in Fig. 2. The double logarithmic plot of the acquired data points shows the typical s-shape behavior of a multimode laser subsequently fitted by a laser model [4]. Below the laser threshold of 110 kW/cm² spontaneous emission occurs accompanied by a linear power dependence and a broad emission spectra, shown in the inset of Fig. 2 (bottom). In the transition region around the laser threshold, the power dependence becomes nonlinear and sharp peaks appear super-

imposed to the spectrum, which are proven to be FP modes of the NW resonator. Above the threshold the power dependence returns to a linear slope and the spectra are dominated by the FP lasing modes.

In order to determine the Stokes parameters of the laser emission, a 8-point-measurement was used as described in [3]. In Fig. 3 the spectrally resolved Stokes parameters and the corresponding degree of polarization of the NW emission in the lasing regime are shown. Note that the parameters S_1 to S_3 are normalized to the total emission intensity S_0 in order to get comparable values over the whole depicted spectral range. At the center of the FP lasing modes, illustrated by the grey dashed lines exemplary for the first four modes, P has highest values of up to 60 %. The spectral region in between is lower polarized due to a high fraction of the spontaneous emission.

Surprisingly, the parameter S_3 is 0.4…0.5 for the first five FP modes indicating an overall dominating right circular polarization; whereas, linear polarization, characterized by S_1 and S_2, has only small contributions to the degree of polarization. However, a high S_3 value does not obligatory suggest a circular polarization: Transverse modes with linear polarization, which changes direction over the beam profile as the case for TE or TM like modes, can also lead to these results. Furthermore, mode switching of transverse modes needs to be considered. A circular polarization is not expected, because no phase shift between x- and y-component of the optical field is introduced due to the isotropic refractive index of ZnO along the direction of the waveguide. Furthermore, no spin selection should occur in the emission process.

Qualitatively, the Stokes parameters appear to be similar for the different FP modes indicating the same polarization properties and resembling transverse modes.

In summary, the spectrally resolved investigation of the Stokes parameters of lasing ZnO NWs revealed the existence of transverse modes with over the beam profile inhomogeneous linear polarization or transverse mode switching. The FP modes of the NW resonator show similar polarization properties with degrees of polarizations up to 60%.

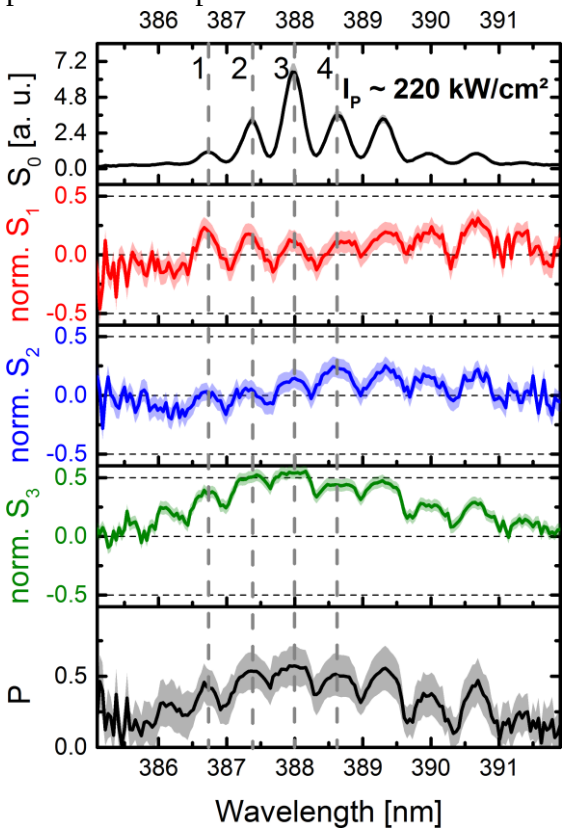

Fig. 3: *Spectral measurement of the Stokes parameters and the corresponding degree of polarization of one lasing ZnO NW.*

References

[1] M.A. Zimmler *et al.*, Appl. Phys. Lett. **93**, 051101 (2008).

[2] G.G. Stokes, Trans. Cambridge Soc. **9**, 399-416 (1852).

[3] B. Schaefer *et al.*, Am. J. Phys. **75**, 163 (2006).

[4] L.W. Casperson *et al.*, JAP **46**, 5194 (1975).

Antimony-doped CdTe nanowires

R. Röder, M. Riediger, L. Huang, C.-C. Lin*, P. L. Tse*, J. G. Lu*, C. Ronning*

** University of Southern California, Department of Physics and Astronomy*

Functional nanoscale elements form the building blocks, which are urgently required to fulfill the accelerated demand in device miniaturization. Semiconductor nanowire (NW) based devices show therefore an immense promise as they've been already used as chemical sensors, field effect transistors (FET), photodetectors and solar cells. Since cadmium telluride (CdTe) exhibits a high absorption coefficient accompanied by a band gap of 1.49 eV at room temperature fitting the sun spectrum, it's needed to be considered also as candidate for core-shell nanostructured solar cells besides the thin film counterparts [1]. Thus, nanowire solar cells as well as photodetectors might in addition benefit from their NW morphology due to the tunable absorption resonances. The fabrication of efficient NW devices is heavily linked to the fundamental understanding of doping in CdTe.

Antimony (Sb) has been proven to be an effective p-type dopant in CdTe although suffering from a self-compensation effect. To gain further insights, we carried out a comprehensive investigation on Sb-doped CdTe NWs with correlating the optical and electrical properties to elucidate the occurrence of the acceptor levels.

Ensembles of CdTe:Sb nanowires were synthesized by using a catalytic chemical vapor deposition (CVD) in a horizontal tube furnace. Details on the growth process are given in [2]. Diameters of the single zinc blende NWs range from 100 nm to 1 µm with a typical length of 10 – 30 µm. Energy dispersive X-ray spectroscopy indicates a stoichiometric atomic ratio of Cd and Te, while the atomic incorporation of Sb is approximately 1 – 2 at.%. The NWs grow along the [200] crystal axis of the zinc blende structure as investigated using high resolution TEM [2].

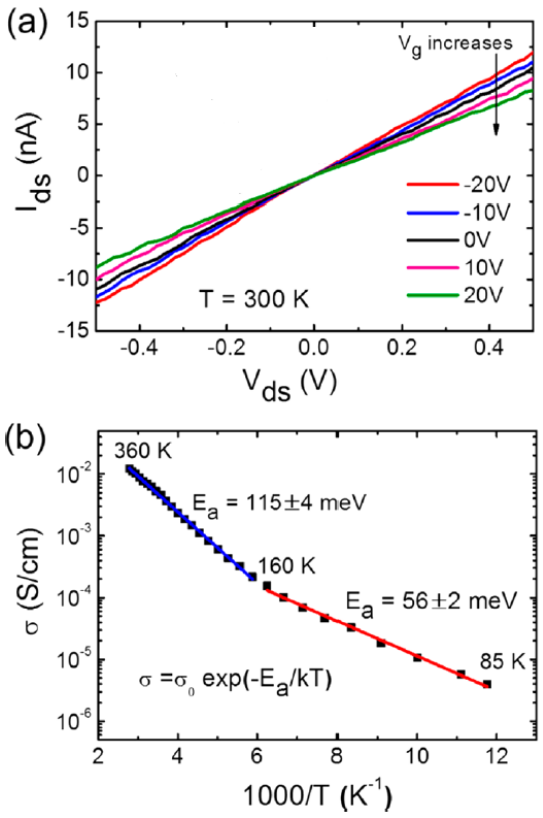

Fig. 1: *(a) Drain-source current I_{ds} as a function of drain-source V_{ds} for various gate voltages V_g for one CdTe:Sb nanowire FET. (b) Arrhenius plot of the conductivity σ versus the inverse temperature also for a CdTe:Sb nanowire FET unambiguously shows two linear regions, corresponding to the two acceptor levels at 56 meV and 115 meV.*

The electrical transport characteristics of single NWs were investigated in FET configuration. Figure 1(a) shows the linear I_{ds} – V_{ds} curves for various gate voltages

V_g, demonstrating p-type gating. Temperature dependent conductivity measurements were performed from 85 – 360K, as shown in the Arrhenius plot of figure 1(b): the two linear regions verify that the electrical transport is governed by thermal excitations involving two acceptor levels induced by Sb incorporation with activation energies of 56 meV and 115 meV above the valence band. The shallow level at 56 meV is attributed to Sb on a Te lattice site (Sb_{Te}).

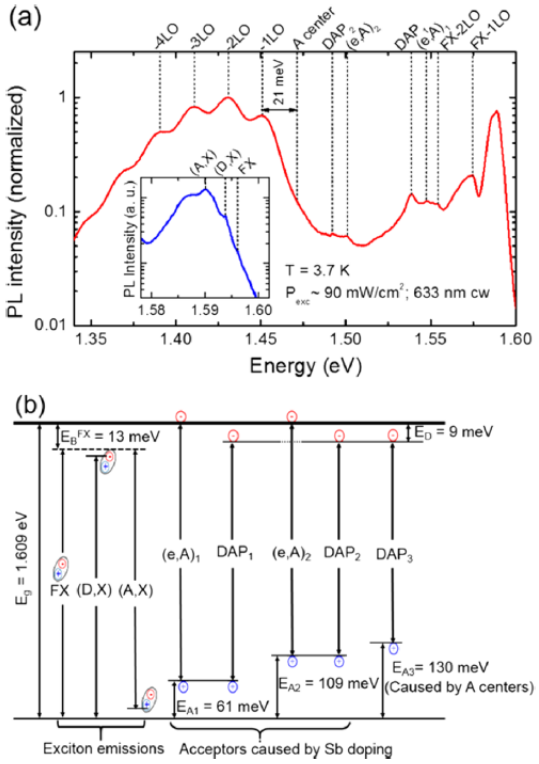

Fig. 2: *(a) Photoluminescence (PL) spectrum of a CdTe:Sb NW ensemble taken at 4K. Several near band edge (NBE) transitions are labeled: the free exciton (FX), donor (D,X) and acceptor bound excitons (A,X), free electron to acceptor (e,A) and donor-acceptor pair (DAP) transitions accompanied by their phonon replica (-LO). (b) The schematic band diagram shows the expected energy levels within the band gap of CdTe:Sb: one donor and three acceptor levels.*

Low temperature photoluminescence (PL) was used to study radiative recombination pathways of the optically excited NW ensemble. Figure 2(a) shows the PL spectrum with the assignment of typical transitions in CdTe: free exciton (FX), donor (D,X) and acceptor bound exciton (A,X) [3]. From the transitions of free electrons with acceptor bound holes (e,A) and the corresponding donor-acceptor pair transitions (DAP), we can determine the donor level to be at 9 meV below the conduction band. The acceptor levels, which are introduced by the Sb are situated at ~ 60 meV and 109 meV above the valence band; thus, the optical and electrical investigations coincide very well. The transition labeled A center originates also from a DAP involving a deeper intrinsic acceptor level contributing to the compensation effect.

Persistent photoconductivity measurements and their temperature dependence reveal that the deeper level arises from Sb in an atomic configuration with large lattice relaxation (AX center) contributing to the compensation effect as well [2, 4].

In conclusion, single crystalline CdTe:Sb NWs have been synthesized with subsequent implementation into NW FET devices. Electrical characterization revealed p-type doping due to Sb incorporation. Antimony doping induces two acceptor levels. The shallow level is attributed to Sb on a Te site, while the deeper level corresponds to an AX center – an atomic configuration with large lattice relaxation compensating free holes in the p-type CdTe NWs.

References

[1] Z. Fan *et al.*, Nat. Mater. **8**, 648-653 (2009).

[2] L. Huang *et al.*, Nano Letters (2015) DOI: 10.1021/nl503781u.

[3] M. Soltani *et al.*, *J. Appl. Phys.* ***78***, 5626-5632 (1995).

[4] D. J. Chadi *et al.*, *Phys. Rev. B* ***59***, 15181-15183 (1999).

Local versus global electronic properties of $Cu(In,Ga)S_2$

Rafael Sarmiento-Pérez[1], Silvana Botti[1], Claudia S. Schnohr, Iver Lauermann[2], Angel Rubio[3,4], Benjamin Johnson[4]

[1] Institut Lumière Matière, Université Lyon 1-CNRS, 69622 Villeurbanne Cedex, France
[2] Helmholtz-Zentrum Berlin für Materialien und Energie, Hahn-Meitner-Platz 1, 14109 Berlin, Germany
[3] Departamento de Física de Materiales, Universidad del País Vasco UPV/EHU, Avenida de Tolosa 72, 20018 San Sebastián, Spain
[4] Fritz-Haber-Institut, Max-Planck-Gesellschaft, Faradayweg 4-6, 14195 Berlin, Germany

Thin film solar cells based on $Cu(In,Ga)(Se,S)_2$ have reached record conversion efficiencies well above 20% thus closing the gap to silicon based technologies. The properties of the material can be specifically tuned by adjusting the material composition. For example, $Cu(In,Ga)S_2$ crystallize in the chalcopyrite structure where each Cu, In and Ga cation has four S first nearest neighbors while each S anion is bonded to two Cu and two group-III (In or Ga) atoms. The lattice constants change linearly with In to Ga ratio between those of the ternary end members. Similarly, the band gap of $Cu(In,Ga)S_2$ changes continuously from 1.5 eV for $CuInS_2$ to 2.4 eV for $CuGaS_2$. Interestingly, this change is mostly caused by a shift of the conduction band minimum while the valence band maximum remains nearly unaltered.

Unoccupied electronic states can be accurately probed by near edge X-ray absorption fine structure (NEXAFS) spectroscopy, where an absorbed photon excites a core level electron into an empty conduction band state according to dipole transition rules. One would thus expect that a shift of the conduction band minimum due to a change of the In to Ga ratio in $Cu(In,Ga)S_2$ leads to a shift of the X-ray absorption edge positions as measured by NEXAFS.

Solar cell grade $CuIn_xGa_{1-x}S_2$ thin films with x = 0, 0.7 and 1 where studied by NEXAFS at the Cu, Ga and S K- and L_3-edges and at the In L_3- and $M_{4,5}$-edges [1]. As an example, Fig. 1 shows the S and Ga K-edge spectra as a function of excitation energy. As expected, the S K-edge position shifts to lower energies when the Ga content of the material and thus the band gap is decreased. A similar behavior is also observed for the S L_3-edge. In contrast, no change is observed in the position of the

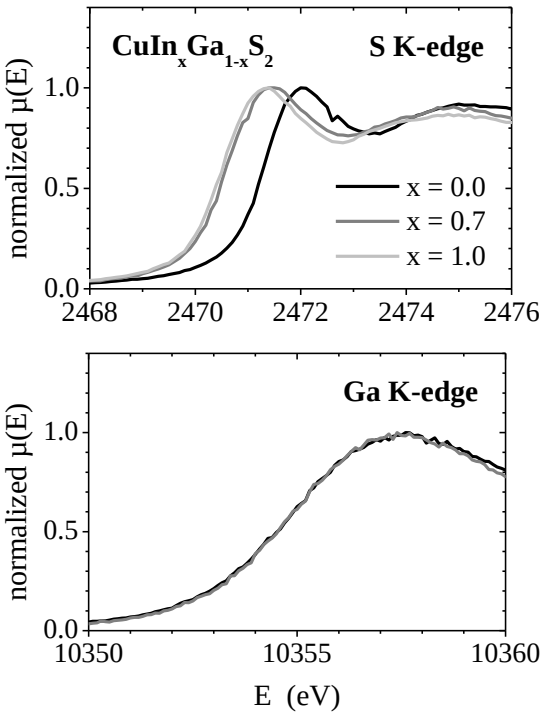

Fig. 1: *Measured absorption coefficient μ(E) versus the X-ray energy E for the S and Ga K-edges of $CuIn_xGa_{1-x}S_2$.*

Ga K-edge in Fig. 1 or any of the other cation edges [1]. This means that although the band gap and thus the energy of the conduction band minimum change, only the anion absorption edges exhibit a corresponding shift whereas the cation absorption edges remain unchanged.

To unravel the origin of this unexpected behavior, we performed density functional theory calculations of the electronic states of $CuIn_xGa_{1-x}S_2$ for different x including 0, 0.7 and 1 [2]. The alloys were modelled with special quasi-random structures and the projected partial densities of states (pDOS) where calculated using a screened hybrid Heyd-Scuseria-Ernzerhof exchange-correlation potential. Figure 2 plots the pDOS of the S and Ga *p* states of the conduction band which correspond to the unoccupied states sampled at the S and Ga K-edge as shown in Fig. 1. Clearly, the S pDOS shifts with changing composition

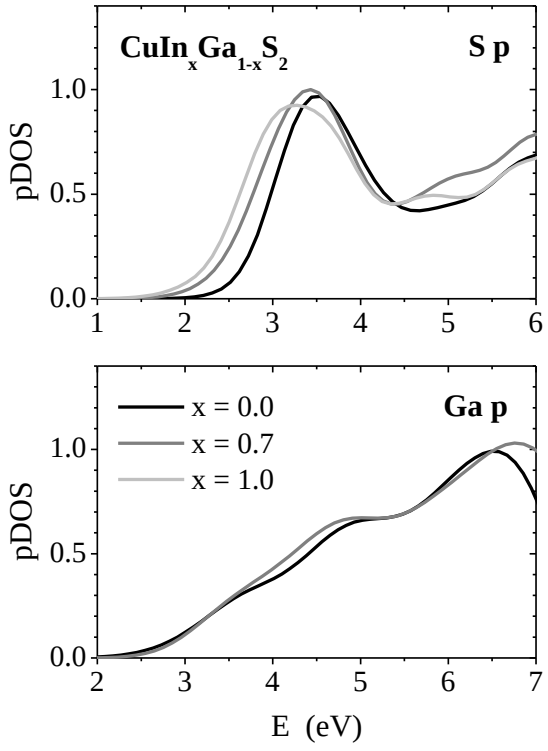

Fig. 2: *Calculated pDOS versus energy E of p states on S and Ga atoms for the conduction bands of* $CuIn_xGa_{1-x}S_2$.

while the Ga pDOS remains unchanged in excellent qualitative agreement with experiment. Similar agreement between the measured NEXAFS spectra and the calculated pDOS is also obtained for the other absorption edges [2].

The explanation for this behavior of the absorption edge positions can be found in the atomic-scale structure of $Cu(In,Ga)S_2$ alloys [2]. All cations are surrounded by four S atoms independent of composition. Furthermore, it was shown by extended X-ray absorption fine structure spectroscopy that the element-specific bond lengths remain nearly constant over the whole compositional range despite the significant change of the lattice constants [3]. The first nearest neighbor structural environment of Cu, In and Ga is thus nearly independent of composition and the *element-specific local* electronic states remain almost unchanged. Since the core level electrons are excited predominantly into unoccupied states of the absorbing atom itself, the absorption process is sensitive to these local electronic states. As a consequence, the cation absorption edges do not shift with changing composition. In contrast, the first nearest neighbor environment of the S anions contains two Cu and two group-III atoms and thus changes with changing In to Ga ratio. Consequently, the S absorption edges shift with varying composition. The observed change of the band gap thus arises from a changing spatial average of the nearly unaltered local states rather than from a change of the states themselves [2].

References

[1] B. Johnson *et al.*, J. Electron Spectrosc. **190**, 42-46 (2013).

[2] R. Sarmiento-Pérez *et al.*, J. Appl. Phys. **116**, 093703 (2014).

[3] S. Eckner *et al.*, Appl. Phys. Lett. **103**, 081905 (2013).

High lateral resolution energy dispersive X-ray spectroscopy on lamellae of CIGSe solar cells

Sven Schönherr, Alexander Tille, Philipp Schöppe, Michael Oertel, Udo Reislöhner, and Carsten Ronning

Because of its high absorption coefficient and its low production costs, $Cu(In,Ga)Se_2$ (CIGSe) is one of the most attractive thin film material for solar cells. Furthermore, solar cells with CIGSe absorber layers show high efficiencies exceeding 20 % [1]. The band gap increases with increasing [Ga]/([Ga]+[In]) (GGI)[2]. A higher open circuit voltage can be obtained with a locally increased GGI in the space charge region and an increasing GGI towards the back contact leads to an electric field in the absorber layer and can benefit the carrier collection [3].

CIGSe solar cells can be prepared in a sequential process. In such a process the bandgap engineering is difficult, since the Ga moves to the back contact during the annealing step. An inappropriate bandgap profile has been shown to lead to a degradation of the solar cell efficiency [4]. Therefore, an efficient characterization technique is needed to measure the Ga-grading.

Energy dispersive X-ray spectroscopy (EDS) measurements can be used to determine the concentration of single elements. However, the spatial resolution strongly depends on the kinetic energy of the electrons, because the excitation volume increases rapidly with the acceleration voltage. It has been shown that a spatial resolution of down to 100 nm may be obtained by reducing the acceleration voltage down to few kV [5]. But such low voltages are not applicable to characterize CIGSe solar cells, because the peak positions of the L-shells are energetic too close to be separated clearly with typically used detectors. Therefore, high voltages are needed, so that the K-shells of the investigated elements are excited. The preparation of thin lamellae reduces the excitation volume. As a consequence, the excitation volume is limited by the thickness of the lamellae and depends only slightly on the acceleration voltage. For the preparation of the thin lamellae our focused ion beam (FIB) system was used.

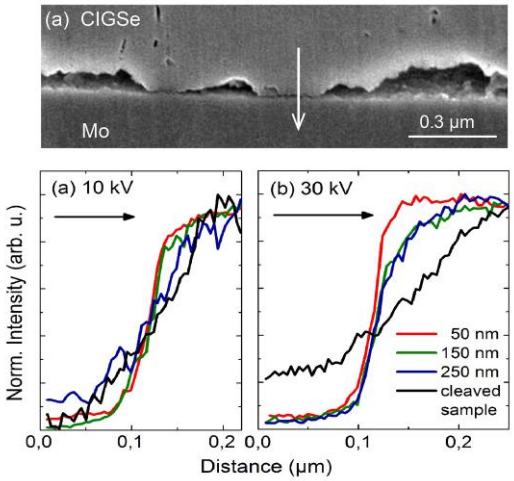

Fig. 1: *Determination of the spatial resolution: SEM image of the abrupt transition between metallic Mo and the CIGSe-layer, exemplarily for a 250 nm thin CISe lamella (a); Normalized EDS intensity of the K-shell molybdenum transition at the CIGSe – Mo interface measured on lamellae with different thicknesses at 10 kV (b) and 30 kV (c); the arrows show the measurement direction across the interface.*

Several lamellae with different thicknesses were prepared in order to determine the spatial resolution as a function of the lamellae thickness. The resolution was measured at the molybdenum absorber interface, because

of the abrupt transition between metallic Mo and the CIGSe-layer (figure 1a). The energy of the molybdenum L-shell was measured across the interface for two different acceleration voltages, 10 kV (figure 1b) and 30 kV (figure 1c) as a function of the lamella thickness. For both voltages the rise of the EDS signal at the interface becomes more abrupt with decreasing lamella thickness, which indicates a higher spatial resolution. The spatial resolution was defined as the distance, where the intensity of the Mo_L line increases from 20 % to 80%. The results are shown in figure 2.

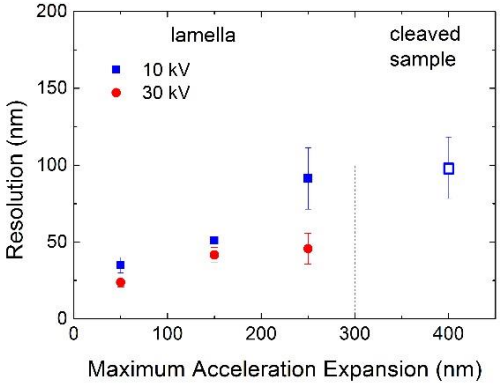

Fig. 2: *Spatial resolution as a function of the lamella thickness, measured at the absorber-molybdenum interface with different acceleration voltages.*

The spatial resolution increases with decreasing lamellae thickness to a resolution of 25 nm for a 50 nm thin lamella and an acceleration voltage of 30 kV. With this high spatial resolution at high acceleration voltages the CIGSe absorber layers can be characterized in detail and the GGI can be determined exactly.

In thin lamellae X-ray absorption and fluorescence can be neglected and thus the EDS intensity is only a function of lamella thickness and composition. Therefore the Ga concentration can be calculated via the corresponding concentration ratio c_A/c_B by the equation:

$$\frac{c_A}{c_B} = k_{AB} \frac{I_A}{I_B},$$

where I_A/I_B is the EDS intensity ratio and k_{AB} is a factor, which accounts for the relative efficiency of X-ray generation and detection. The factor was determined as 1.31 at a reference cell with known GGI.

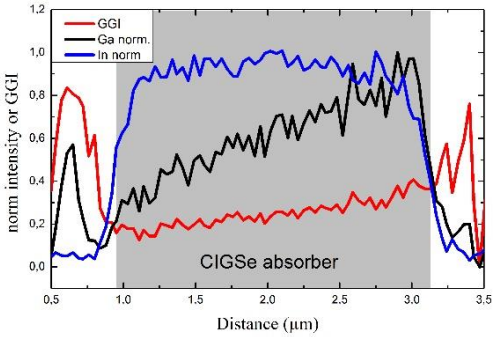

Fig. 3: *Normalized intensity of the EDS-signal from the In_L and the Ga_K transition measured at a 250 nm thin CIGSe lamella with an acceleration voltage of 30 kV and the calculated GGI.*

A 250 nm thick CIGSe lamella with a homogeneous sputtered precursor layer was investigated. The intensities of the EDS-signal from the In_L and the Ga_K transition were detected and the GGI was calculated and is shown in figure 3 with the typical increasing Ga concentration to the back contact. Further details and results can be found in reference [6].

References

[1] M. A. Green *et al.*, Prog Photovolt: Res. Appl. **21**, 1107-1111 (2013).

[2] S. Wei *et al.*, J. of Appl. Phys. **78**, 3846-3856 (1995).

[3] O. Lundberg *et al.*, Thin Solid Films **480-481**, 520-525 (2005).

[4] M. Gloeckler *et al.*, J. of Phys. and Chem. of Solids **66**, 1891-1894 (2005).

[5] I. Barkshire *et al.*, J. Mikrochimica Acta **132**, 113-128 (2000).

[6] S. Schönherr *et al.*, PVSC 2014 IEEE 40th, 1699-1703 (2014).

Improved Ga grading of Cu(In,Ga)Se_2 lamelles confirmed by X-ray fluorescence analysis

Philipp Schöppe, Claudia S. Schnohr, M. Oertel, A. Kusch, A. Johannes, S. Eckner, M. Burghammer[1,2], G. Martínez-Criado[1], U. Reislöhner, C. Ronning

[1] *European Synchrotron Radiation Facility, B.P. 220, F-38043 Grenoble Cedex, France*
[2] *Department of Analytical Chemistry, Ghent University, Krijgslaan 281, S12, B-9000 Ghent, Belgium*

Chalcopyrite type thin film solar cells have recently closed the gap to silicon based technologies after record efficiency above 20 % was reported [1,2]. The Cu(In,Ga)Se_2 absorber is by nature inhomogeneous at different scales [3-7]. Compositional and structural properties of the absorber affect the solar cell performance [8]. Especially the Ga gradient of the absorber has a strong impact on the efficiency [9]. In order to investigate the composition of the solar cell a new approach of measuring thin cross section lamellas via highly focused synchrotron X-ray fluorescence (XRF) was developed. Two different Cu(In,Ga)Se_2 solar cells were analyzed using this new approach [10].

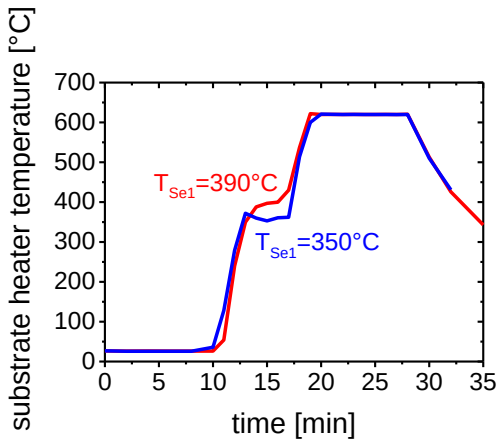

Fig. 1: *Two stage selenization process of two Cu(In,Ga)Se_2 samples. The substrate temperature during the first stage was set to either 350°C or 390°C. The substrate temperature during the second stage was the same for both samples.*

The Cu(In,Ga)Se_2 solar cells were produced via a sequential process [11]. For the two investigated samples the same set of process parameters was used except for the substrate temperature during the first stage of selenization, which was set to either 350°C or 390°C (see **Fig. 1**). Thin cross section lamellas, which were prepared using a focused ion beam (FIB), were cut out from complete solar cell devices. The lamellas had a final thickness of 200 to 300 nm. Subsequently, the lamellas were analyzed by X-ray fluorescence measurements with high spatial resolution at the Beamline ID13 of the European Synchrotron Radiation Facility (ESRF). The X-ray beam with a spot size between 200 and 300 nm scanned the lamella and the resulting fluorescence radiation was analyzed. As the typical grain size of Cu(In,Ga)Se_2 is in the order of one micrometer our new approach offers the possibility of getting information even from single grains.

Fig. 2 shows the obtained Ga/(Ga+In) ratio (GGI) of the two samples. The integral amount of Ga is more or less the same for both samples. The low temperature sample shows an increase of the GGI from 0.15 at the front contact to 0.35 at the back contact; whereas, the high temperature sample shows an almost homogenous GGI over the depth. The homogenous Ga profile while having the

same integral amount of Ga leads to a higher Ga concentration at the p-n junction. Thus, the open circuit voltage is

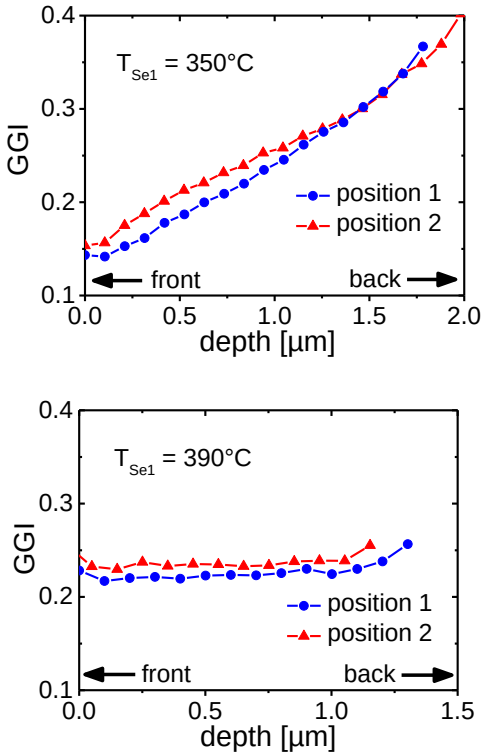

Fig. 2: *Ga/(Ga+In) ratio (GGI) of two different Cu(In,Ga)Se$_2$ samples, which were prepared under the same conditions except for the substrate temperature during the first stage of selenizaztion T_{Se1}. For each sample two GGI profiles from different areas of the lamellas are displayed.*

significantly increased, which contributes beneficial to the efficiency of the solar cell. Unfortunately the high temperature sample shows a lower steep of the GGI towards the back contact compared to the low temperature sample. That reduces the short circuit current. But the positive impact of the increased open circuit voltage outweighs this negative impact of the reduced short circuit current. The efficiency for those two samples could be improved from 11.0 to 12.1 % (total area, without anti-reflection coating). In addition, **Fig. 2** shows for each sample two Ga profiles, which belong to different areas of the lamellas. For both samples a slight variation of the GGI in the order of 0.01 can be observed. This is the same order like the uncertainty of the measurement. However, the variation of the GGI is systematic and hence it is significant.

References

[1] A. Chirila et al., Nat. Mater. **12**, 1107 (2013).
[2] P. Jackson et al., Phys. Status Solidi RRL **8**, 219 (2014).
[3] U. Rau et al., Appl. Phys. A **96**, 221 (2009).
[4] U. Reislöhner and C. Ronning, Appl. Phys. Lett. **100**, 252111 (2012).
[5] C. S. Schnohr et al., Phys. Rev. B **85**, 245204 (2012).
[6] S. Eckner et al., Appl. Phys. Lett. **103**, 081905 (2013).
[7] Y. Yan et al., Appl. Phys. Lett. **87**, 121904 (2005).
[8] D. Abou-Ras et al., Sol. Energy Mater Sol. Cells **95**, 1452 (2011).
[9] O. Lundberg et al., Thin Solid Films **480–481**, 520 (2005).
[10] Ph. Schöppe et al., Appl. Phys. Lett. **106**, 013909 (2015).
[11] M. Oertel, Ph.D. thesis, Friedrich-Schiller-Universität Jena, Germany.

Growth of free-standing phase-pure vanadium dioxide nanowires

Alexander Tille, Jura Rensberg, Tim Barth, and Carsten Ronning

One of the most interesting and widely studied phase change material is vanadium dioxide (VO_2), which exhibits a metal to insulator transition (MIT) when the temperature is increased above a critical temperature T_C~ 68°C for bulk. The high-speed reversible transition in the order of nanoseconds makes this material very promising for integrated devices like ultra-fast switches, sensors, or memories [1].

The growth of high-quality VO_2 films with bulk-like electronic properties and high crystalline quality is still challenging. Enormous strains exist at the interfaces, mainly due to the differences in the crystal lattice parameters and thermal expansion coefficients between film and substrate [2]. For this reason, nanostructures are of particular relevance. For example stress can quickly relax laterally in nanowires, allowing growth with very high crystal quality [3].

A lot of synthesis methods have been developed in order to obtain VO_2 nanowires. Unfortunately, VO_2 nanowires cannot be grown by metal catalyst aided chemical-vapor-deposition but rather by oxygen assisted self-catalytic growth. Most growth methods need an oxygen rich surface layer and provide nanowires, which are embedded in the substrate surface. To circumvent this issue Cheng et al. proposed roughened silica as growth substrates [4]. Although the nanowires are still embedded in the substrate, the growth front can leave the substrate, due to the rough surface resulting in undirected free-standing nanowire growth.

In this study, we will show the influence of different substrate temperatures on the vanadium oxide phase and morphology of the grown nanowires. Therefore, V_2O_5 powder was placed in a ceramic boat in a horizontal tube furnace. Rough silica substrates were placed above the V_2O_5 precursor. During growth the pressure was kept constant at 3 mbar and the evaporation time was at least one hour. The temperature was varied in a range between 650°C and 900°C.

The morphology of the grown nanowires was investigated using a SEM Jeol JSM-6490. The results for all growth temperatures are summarized in figure 1.

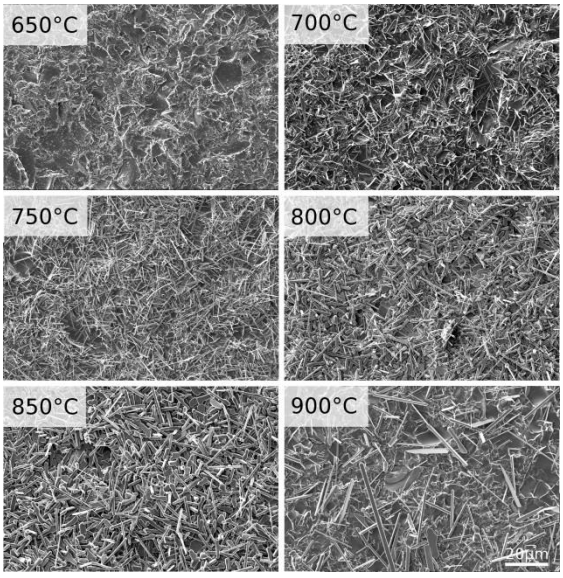

Fig. 1: *REM images of roughened SiO_2 used as growth substrates for VO_2 nanowire growth at different growth temperatures. Above 700°C free-standing VO_2 nanowires are grown.*

At 650°C solid droplets can be observed all over the silica surface. These droplets are the starting point of self-catalytic nanowire growth. Due to the melting point of V_2O_5 at 680°C at normal conditions the support with material for nanowire growth

was too low to form a significant amount of nanowires.

Increasing the growth temperature to 700°C leads to a higher material flux towards the sample surface resulting into nanowire growth. Furthermore, the nanowires grow out of the quartz surface. At 750°C the density of the wires further increases and the shape of the wires is more uniform than at 700°C. An increase of the temperature up to 800°C and 850°C leads to a further increase of the nanowire density. At this temperature the substrate is completely covered with nanostructures. At these temperatures the growth changes partially from uniaxial growth to two-dimensional growth, which leads to small platelets and nanowires with larger diameters. Therefore, the grown structures change a lot at temperatures of 900°C. Large microwires and two-dimensional structures can be observed.

In order to determine the phase of the grown nanowires, Raman spectroscopy using a Renishaw inVia 56H940 with a 514 nm Argon laser was employed. The laser spot had a diameter of 15µm in order to average the Raman signal of many wires. The results are shown in figure 2. In order to compare the measured results with known vanadium oxide phases, the Raman spectra of V_2O_5 and VO_2 are also shown in figure 2. The important peaks of these phases are marked with diamond or triangle symbols, respectively.

Although the Raman intensity of the sample grown at 650°C is very low, the spectrum shows the two prominent peaks of V_2O_5 at 145 cm^{-1} and 994 cm^{-1}, which is consistent with the V-O phase diagram. On the other hand, Raman peaks of both the V_2O_5 and VO_2 phase are observed for samples grown at 700°C, which means, that these nanowires consist of mixed vanadium oxide phases. Moreover, the prominent VO_2 peak at 615 cm^{-1} (triangle) is shifted to higher wavenumbers, indicating the existence of strain in the material and forming a metastable VO_2 phase. Above 750°C all Raman spectra can be attributed to phase-pure unstrained VO_2.

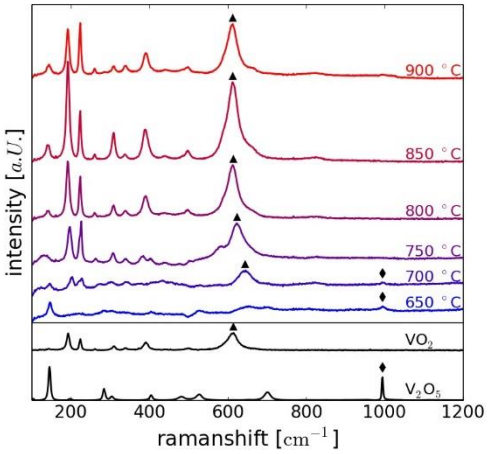

Fig. 2: *Raman spectra of the nanowires on the growth substrate. As comparison the spectra of V_2O_5 and VO_2 (black). Important peaks are marked with diamond and triangle symbols, respectively.*

In conclusion, we have shown that phase- pure free-standing VO_2 nanowires can be grown on rough silica substrates without the use of a metal catalyst. Furthermore, an increasing growth temperature results in a gradual transition of the grown nanowires from V_2O_5 to VO_2 via metastable vanadium oxide phases.

References

[1] Soltani *et al.*, Applied Physics in the 21st Century (2008).

[2] Wong *et al.*, J. of Cryst. Growth **364**, 74 (2013).

[3] Mandl *et al.*, Nano Letters **6**, 1817 (2006).

[4] Cheng *et al.*, Applied Physical Letters **100**, 103111 (2012).

Formation of GaN nanocrystals in thermally oxidized silicon

E. Wendler, K. Filintoglou[1], P. Kutza, Ph. Lorenz, K. Lorenz[2], F.F. Komarov[3], S. Ves[1], E. Paloura[1] and M. Katsikini[1]

[1]*Aristotle University of Thessaloniki, Greece*
[2]*Instituto Superior Técnico Bobadela, Portugal*
[3]*Belarusian State University, Minsk, Belarus*

Ion implantation is a well established technology in device fabrication. There is some interest in application of this technique to the formation of nano-structures within the Si technology as a possible solution for combining electronic and optical functionalities on one and the same chip. One possible ansatz is the formation of nano-crystals in SiO_2 thermally grown on Si. Additionally there is a general interest in understanding of the formation of nano-structures by ion implantation and subsequent annealing.

In our investigations thermally grown SiO_2 layers of about 1 µm thickness on Si were implanted with 180 keV Ga ions to an ion fluence of 6×10^{16} cm^{-2} and 50 keV N ions to7.5×10^{16} cm^{-2}. After implantation rapid thermal annealing (RTA) with halogen lamps is performed at temperatures between 1000 und 1300°C for 30 s up to 10 min in an atmosphere of 50% N_2 and 50% NH_3.

The total amount and distribution of Ga is detected with Rutherford backscattering spectrometry (RBS) using 1.4 MeV He ions. For detecting the total amount of N the resonance of 3.7 MeV He ions is exploited. The existence of GaN bonds in the implanted and annealed samples is studied by extended X-ray absorption fine structure (EXAFS) at the Synchrotron Radiation Storage Ring BESSY in Berlin and by Raman spectroscopy (RS).

The optimum annealing conditions with respect to retaining the implanted Ga and N atoms within the samples as detected by RBS were found to be 1000°C and times between 30 and 90 s. Higher temperatures or longer annealing times result in a loss of both Ga and N atoms through the surface.

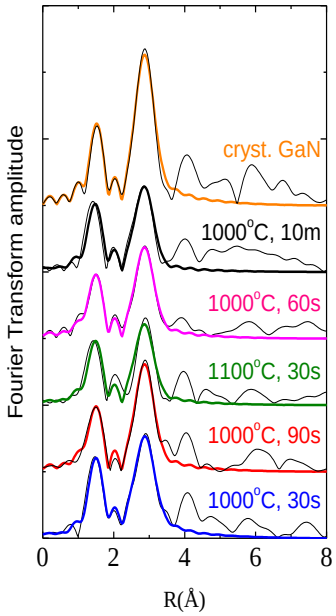

Fig. 1: *Fourier transform amplitude of the EXAFS spectra (color lines: fitting, then black lines: experiment) for implanted and annealed samples and for a crystalline GaN sample.*

Fig. 1 shows the Fourier transform amplitude of the EXAFS spectra. The comparison with that of crystalline GaN clearly indicates the existence of microcrystalline GaN in the implanted and annealed SiO_2. A more detailed analysis of the spectra reveals that coordination number and nearest neighbor distance are closest to that of GaN for annealing at 1000°C for 90 s. The existence of microcrystalline GaN was confirmed by RS (not shown).

Damage formation in $LiNbO_3$ due to electronic energy loss

E. Schmidt, J. Rensberg, M. Schmidt, M. Toulemonde[1], W. Wesch, E. Wendler

[1]CIMAP, Caen, France

For the formation of wave guide structures in $LiNbO_3$ thick layers are necessary which can be achieved by implanting high-energetic ions with energies of few MeV. In this case both nuclear and electronic energy deposition of the implanted ions to the lattice atoms contribute to damage formation. For thick layers and complicated crystals like $LiNbO_3$ difficulties may arise in the determination of damage profiles by Rutherford backscattering spectrometry (RBS) in channelling mode. For solving this problem, the dechannelling probability was calculated over an extended range of reduced damage thicknesses and a factor was introduced, which allows to controlling the height of the dechannelling background of the analysing He ions.

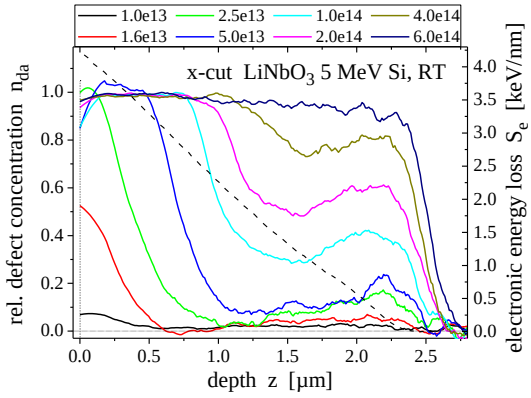

Fig. 1: *Damage profiles $n_{da}(z)$ for 5 MeV Si ions implanted into x-cut LiNbO3 at RT: The ion fluences are given in cm^{-2}. The dashed line is the electronic energy loss S_e.*

Under these conditions reasonable damage profiles are obtained which reach zero at the end of the implanted layer. This is demonstrated in Fig. 1 for x-cut $LiNbO_3$ implanted with 5 MeV Si ions at room temperature (RT). Of special interest here is the damage formation at the surface, which is caused by the electronic energy loss of the implanted ions (see Fig. 1).

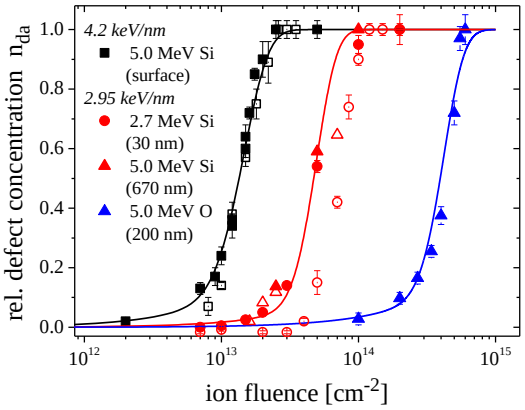

Fig. 2: *Relative defect concentration versus ion fluence for x-cut (filled symbols) and z-cut (open symbols) $LiNbO_3$ for two different values of the electronic energy loss per unit depth reached by different implantation conditions as indicated in the figure.*

The effect of the electronic energy loss on damage formation in $LiNbO_3$ is not yet fully understood. By calculating proper damage profiles, defect evolution versus ion fluence can be studied for fixed values of the electronic energy loss S_e occurring at different depths, which is shown in Fig. 2. This figure reveals that the defect concentration remaining after implantation does not solely depend on the electronic energy loss S_e but also on the ion species. This indicates the importance of the lateral energy distribution perpendicular to the beam direction. Differences between x-cut and z-cut LiNbO3 occur when mainly point defects and no amorphous clusters exist within the irradiated layer.

Electrical percolation in MgB_2-$La_{0.7}Sr_{0.3}MnO_3$ composites: evidence for a superconducting long-range proximity effect in the magnetic manganite

Mykola Krupa[1], Victoria Kononenko[2], Vladimir Tarenkov[2], Mikhail Belogolovskii[2], Stefan Schmidt, and Paul Seidel

[1] *Institute of Magnetism, 03142, Kyiv, Ukraine*
[2] *Donetsk Institute for Physics and Engineering, 83114, Donetsk, Ukraine*

Coexistence of such antagonistic phenomena as superconductivity (S) and ferromagnetism (F) below their respective ordering temperatures, T_c and T_C, is a longstanding problem in solid-state physics. Originally, it was believed that they are mutually exclusive, but more recently it was found that they can coexist under certain circumstances giving rise to novel combined effects. One of the possibilities to observe the interplay between itinerant electron ferromagnetism and superconductivity is to put the two metallic films into a contact. In this case, due to the proximity effect, superconducting correlations penetrate into the F-metal. In a diffusive system, spin-singlet superconducting correlations, as well as triplet ones with zero spin projection on the F-layer magnetization axis, decay over a very short distance $\xi_F = \sqrt{\hbar D/(2\varepsilon_{ex})}$, where D is the F-layer diffusion coefficient and ε_{ex} is the exchange energy. But it is not so when the triplet component with a finite total spin is generated at a magnetically inhomogeneous F/S interface which can be created, in particular, by domain walls, ultra-thin magnetic multilayers with different magnetization orientations, etc. [1]. In this case, superconducting correlations can penetrate into the F region over a much longer distance of the order of $\xi_T = \sqrt{\hbar D/(2\pi k_B T)}$ where T is the temperature. Since usually $k_B T << \varepsilon_{ex}$, supercurrent in such SFS structures can be detected for anomalously large distances between the S electrodes.

The most striking observation of a long-range Josephson effect was that in lateral structures based on the half-metallic CrO_2 [2]. But up to now there is no consensus relating half-metallic manganite layers with 100% spin polarization where singlet superconducting correlations cannot exist in principle. Some authors have registered the long-range proximity phenomenon [3,4] while other deny it and explain the observation by the effect of pinholes [5,6].

In this work, we address this problem by studying transport characteristics of composites formed by granules of a superconducting MgB_2 on μm scale and those of $La_{0.7}Sr_{0.3}MnO_3$ (LSMO) as small as 8-10 nm. The extreme difference between the sizes of the two compounds is the most important feature of our samples. Homogeneous structure of the composite was attained by mixing the components in alcohol followed by drying and additional mechanical agitation. The resulting mixture was pressed into plates with dimensions 0.2 mm × 1 mm × 10 mm under pressure of 40-60 kbar. It is known that the density of *in situ* prepared MgB_2 samples is typically only about half of its theoretical value which indicates high porosity. [7] In our case, the density of MgB_2 after treating with the pressure of 40-60 kbar reached the value of (72 ± 3) %. The density of the LSMO nanopowder compacted at the same pressure was (68 ± 3) % of bulk value. At the same time, the density of the MgB_2 - LSMO composite with the relative volume fraction of superconducting grains $p \approx 0.74$ was (96 ± 3) % of the theoretical value. Such high density of the composite indicates that under high uniaxial pressures the LSMO nanopowder was "spreading" over the sample filling the pores around comparatively large granules of magnesium diboride.

The normal-state resistance of the compounds was extremely low for the volume fraction of LSMO in the MgB_2 background

between 0 and 10 %. It started to rise above p = 0.9 and suddenly enhanced by more than an order of magnitude at $p = p_c \approx 0.8$ which can be regarded as a percolation threshold for the underlying network of well conducting magnesium diboride and high-resistive manganite components. The finite resistance up to 4.2 K for the composite with p = 0.74 proves that all superconducting paths through the sample are blocked by non-superconducting inclusions. It can be clearly seen in Fig. 1 where we demonstrate current-voltage characteristics for two composites with p = 0.9 and 0.74.

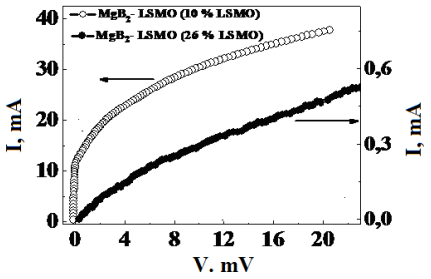

Fig. 1: Current-voltage characteristics of two composites formed by magnetic LSMO and superconducting MgB_2 granules, T = 4.2 K.

If we assume that the manganite grains form a sheath around MgB_2 granules, we can estimate the average thickness d of the sheath for the threshold value $p_c \approx 0.8$: d = 350 - 700 nm. The proximity-induced spectral features were observed in papers [3,4] for manganite thicknesses up to 30 nm (note that this value is an order of magnitude larger than the expected ferromagnetic coherence length ξ_F in manganites). Such extra-thinning of the manganite coverings with the average d of the order of hundreds nm seems improbable. From the other side, if the ferromagnetic manganite grains would be completely impenetrable for superconducting correlations (except the very narrow sheath of the order of ξ_F which is equal to a few nanometers in manganites [3]), the resistance of the composite should drop to a finite value determined by normal interspaces and the transition interval would be very narrow. On the contrary, the transition region for a sample with p = 0.9 was about 10 K after which the resistance vanishes while that for p = 0.74 was about 25 - 30 K before the flattening in the $R(T)$ curve which approached an asymptotical value equal at T = 0 to one-third of the normal magnitude. In our opinion, these results definitely indicate the presence of proximity-induced effects at distances of the order of several tens of nanometers.

To find additional arguments supporting the statement above we have performed high-pressure experiments. The samples with p = 0.74 were placed into a pressure chamber with a piston and a mixture of kerosene with oil as a pressure-transmitting medium. At pressures of about 12 kbar, we have observed a shift of the midpoint in the $R(T)$ curve to higher temperatures which can be related to the enhancement of the superconducting proximity effect in hetero-contacts formed by superconducting MgB_2 and ferromagnetic manganite components. Moreover, whereas in pure MgB_2 the critical current was reduced under the 12 kbar pressure (in accordance with the tendency of the critical temperature T_c), in our hybrid samples it rather increased.

Resuming, our experiments have yielded new indirect arguments proving the existence of a superconducting current across proximized regions of half-metallic $La_{0.7}Sr_{0.3}MnO_3$ manganite, most probably, due to the generation of triplet superconducting correlations.

This work was performed within the German-Ukrainian project SE 664/18-1 supported by the Deutsche Forschungsgemeinschaft (DFG).

References

[1] F. S. Bergeret, A. F. Volkov, and K. B. Efetov. Rev. Mod. Phys. **77**, 1321, 2005.
[2] R. S. Keizer, S. T. B. Goennenwein, T. M. Klapwijk *et al.* Nature **439**, 825, 2006.
[3] Y. Kalcheim, T. Kirzhner, G. Koren, and O. Millo. Phys. Rev. B **83**, 064510, 2011.
[4] C. Visani, Z. Sefrioui, J. Tornos *et al.* Nature Phys. **8**, 539, 2012.
[5] M. Van Zalk, A. Brinkman, J. Aarts *et al.* Phys. Rev. B **82**, 134513, 2010.
[6] A. M. Petrzhik, G. A. Ovsyannikov, A. V. Shadrin *et al.* J. Exp. Theor. Phys. **112**, 1042, 2011.
[7] M. Eisterer. Supercond. Sci. Technol. **20**, R47, 2007.

High-performance MgB_2 superconductors: role of Mg-B-O nanoinclusions

Andrii Shapovalov[1], Tatyana Prikhna[1], Viktor Boutko[2], Mikhail Belogolovskii[2], and Paul Seidel

[1] *Institute for Superhard Materials, 04074 Kyiv, Ukraine*
[2] *Donetsk Institute for Physics and Engineering, 83114, Donetsk, Ukraine*

The normal-to-superconducting transition at 39 K discovered more than ten years ago in magnesium diboride, with a simple binary chemical composition, attracted much interest in diverse practical applications. Up to now, one of the central topics of research in this field is the critical current density J_c in bulk MgB_2 materials, the main parameter allowing their use in motors, generators, magnetic separators, magnetic levitation systems, as well as high-energy physics devices operated at 10–20 K without liquid helium. The primary obstacles suppressing the global J_c value in MgB_2 polycrystalline samples are impurity phases. Although defect inclusions with sizes comparable to the coherent length of the superconductor play, as usually, he role of strong flux pinning centers, the presence of large-size particles at the grain boundaries could result, as it is often considered, in the degradation of grain connectivity.

Whereas magnesium diboride is nominally an oxygen-free compound, magnesium oxide MgO is always present in the final compounds as an inevitable impurity phase due to the high affinity of magnesium to oxygen, which can be supplied by the gaseous oxygen in the protective Ar gas and/or oxide impurities like boron oxides in the starting materials [1]. In this contribution, we provide new arguments supporting the statement that, contrary to the generally accepted opinion, MgO and Mg-B-O inclusions play a positive role for attaining high critical current densities not only as pinning centers but also as **connecting bridges** between superconducting MgB_2 grains.

Let us now refer to results of the works [2,3] where MgB_2 bulk samples with enhanced critical current densities have been successfully fabricated using hot pressing process. Oxygen-rich Mg-B-O nano-layers and/or nano-scaled inclusions have been observed in all samples independently on the preparation method, pressure (0.1 MPa - 2 GPa), and temperature (600-1100^o C), as well as in MgB_2 ceramics with different connectivity (18-98%) and density (55-99%). It was also found that increase in critical transport values in low and medium magnetic fields is accompanied by transformation of 15-20 nm thick Mg-B-O nanolayers into separated inclusions and by the impurity oxygen localization. In the following, in order to get systematic insight into electronic properties of oxygen-rich MgB_2 compounds, we present a comparative first-principles study of the electronic band structure of three Mg-B-O compounds. Comparison with the MgB_2 band structure shows that they are metals with very similar band parameters. This finding suggests that superconducting transport across two comparatively large MgB_2 grains linked by a Mg-B-O bridge occurs due to the proximity effect which induces superconducting correlations in, probably, normal oxygen-rich MgB_2 conducting voids.

In our calculations, we have assumed that Mg-B-O compounds adopt the same layered crystal structure (space group P6/*mmm*) as that of the parent MgB_2. It is a simple hexagonal lattice of close-packed metal layers alternating with graphite-like B interlayers where a part of boron atoms is substituted with oxygen ones. The boron atoms are arranged at the corners of a hexagon with three nearest neighbor B atoms in each plane. The metal atoms are located at the center of the B hexagons, midway between adjacent boron layers. In the parent compound, the primitive cell contains one metal and two boron atoms. The band struc-

ture of $Mg(B_{1-x}O_x)_2$ was calculated for four different values of x = 0, 0.125, 0.25, and 0.5. For x equal to 0.125 and 0.25, we have used a super-cell (2×2×1) including four monocrystalline MgB_2 primitive cells. For each composition, lattice parameter values were optimized.

To analyze the Mg-B-O compounds, we have applied the density functional theory [4] based on a full-potential linearized augmented plane wave method with the generalized gradient correction to exchange-correlation potential [5] (the program package WIEN2k [6]).

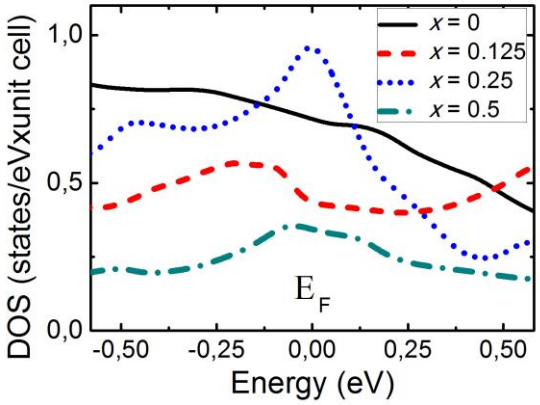

Fig. 1:. Total density of electronic states in pure MgB_2 (solid line), $MgB_{1.75}O_{0.25}$ (dashed line), $MgB_{1.5}O_{0.5}$ (dotted line), and MgBO (dashed-dotted line) compounds.

Fig. 1 shows an effect of the oxygen substitution on the total densities of states (DOS) in magnesium diboride and three Mg-B-O compounds. In the nearest vicinity of the Fermi energy E_F corresponding dependencies are not constant and their changes with x are non-monotonous. But, in any case, all compounds studied are conductors with a non-zero density of states at the Fermi level. Large density of delocalized states proves the metallic type of the charge transport in studied compounds.

Even if they are not superconducting, the Cooper pairing in Mg-B-O inclusions can be induced via proximity effect improving the background grain connectivity. We believe that it is one of the main factors which strongly improve MgB_2 critical transport characteristics relevant for power applications.

Table 1 compares the total densities of states and related binding energies E_b in the studied Mg-B-O compounds. The comparison of the latter values shows that appearance of mesoscopic inclusions with comparatively high oxygen content is disadvantageous from the energetic viewpoint. It means that such defects will be pushed out from the crystallization zone to peripheral regions and the oxygen entry into the Mg-B-O compound is only related to the limitation of the kinetic processes within the separation diffusion.

Table 1. Total DOSs and binding energies in the $Mg(B_{1-x}O_x)_2$ compounds.

x	0	0.125	0.25	0.5
total DOS	0.72	0.43	0.96	0.34
E_b, Ry	1.12	1.10	1.06	0.94

We have numerically studied possible lattice distortion effects in the oxygen-rich compounds and found that, for x = 0.125 and 0.25, deviations from the unperturbed lattice are indeed small while it is not so for x = 0.5. In our opinion, it is an indication of the presence of an upper metastability boundary for the Mg-B-O system when the oxygen content increases.

This work was performed within the German-Ukrainian project SE 664/18-1 supported by the Deutsche Forschungsgemeinschaft (DFG).

References

[1] Z. Ma and Y. Liu. In: Sintering of Ceramics - New Emerging Techniques, A. Lakshmanan (Ed.), In Tech, pp. 469-498, 2012; ISBN 978-953-51-0017-1.

[2] T. A. Prikhna, W. Gawalek, V. M. Tkach *et al.* J. Phys.: Conf. Ser. **234**, 012031, 2010.

[3] T. Prikhna, M. Eisterer, W. Gawalek *et al.* Solid State Phenom. **200**, 137, 2013.

[4] R. G. Parr and W. Yang, W. Density-Functional Theory of Atoms and Molecules, Oxford Univ. Press, 1989.

[5] J.P. Perdew, S. Burke, and M. Ernzerhof, Phys. Rev. Lett. **77,** 3865, 1996.

[6] P. Blaha, K. Schwarz, G. K. H. Madsen *et al.* WIEN2K, An augmented plane wave + local orbitals program for calculating crystal properties. Techn. Univ., Wien (2001).

Quasiparticle Spectroscopy on Co-doped Ba-122

Sebastian Döring, Stefan Schmidt, Noor Hasan, Volker Tympel, Frank Schmidl, Kazumasa Iida[1], Fritz Kurth[1], Ingolf Mönch[1], Bernhard Holzapfel[1], and Paul Seidel

[1] *Institute for Metallic Materials, IFW Dresden, Helmholtzstraße 20, D-01069 Dresden*

For the investigations on iron-based superconductors we used SNS' and SIS' heterojunctions in different geometries [1,2]. They consist of a $Ba(Fe_{1-x}Co_x)_2As_2$ (Ba-122) base electrode, a Pb counter electrode (covered by In) and different kinds of barriers. The planar junctions used sputtered layers of gold and oxidized titanium. This junction type uses current transport along the c-axis of Ba-122. The second junctions are edge-type ones for the transport in the ab-plane. They have interface engineered barriers, caused by the influence of chemicals, ion beams and chemical reactions on atmosphere (O_2, H_2O) to the Ba-122 surface. Both junction types can be used for Andreev- and tunneling spectroscopy, if the junction is measured at temperature above the critical temperature of the Pb counter electrode.

To describe a normal conductor (N) – superconductor (S) interface with some barrier between commonly the Blonder-Thinkham and Klapwijk (BTK) model is used [3]. Therein the barrier potential is assumed as $= U_0\delta(x)$. To describe the interface transparency the parameter $Z = U_0/\hbar v_F$ is used. The extrema $Z = 0$ and $Z \to \infty$ simulates a full transparent barrier and an insulating barrier, respectively. The normalized differential conductance of the junction is given by:

$$\frac{G}{G_n} = \frac{(1+Z^2)}{e}\frac{d}{dV} \int_{\infty}^{\infty} [f(E-eV) - f(E)][1 + A(E) - B(E)]dE \qquad (1)$$

f(E) is the Fermi-distribution, while the parameters A(E) and B(E) are the probabilities for Andreev- and normal reflection. Both contain Z as well as the Order parameter Δ. The existence of multiple gaps can be included by the weighting of single conductances as well as by scattering between these bands [4].

In iron-based superconductors there are band-structure calculation of hole-like bands around the Γ point and electron-like bands around the M point crossing the Fermi energy. This leads to the proposal of an extended or anisotropic s-wave symmetry of the order parameter [5], but also d- and p-wave [6,7] are not fully excluded.

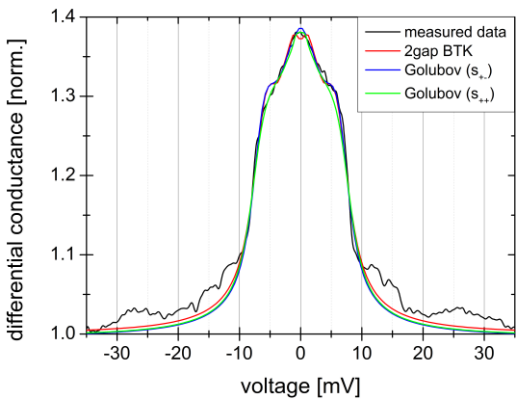

Fig. 1: *Normalized conductance of an edge-type junction with an area of 7µm × 100 nm at T=8.2K.*

Firstly we present a spectrum from an edge-type junction as it is shown in fig. 1. As can be seen, it shows a steep increase for |V|<10meV and a second smaller peak around zero. The modelling is done by the weighted 2-band BTK model and the model of Golubov *et al.* [4], which

includes scattering. This is done with the same sign of both bands (s++) and different signs (s+-). As one can see, all three models give similar but well agreement to the measured data. Deviation at higher voltages are caused by electron-phonon interactions, which are not included in the models. The gap values, which can be obtained from the fits are between 6.3 and 7.2 meV for Δ_1. For the lower gap Δ_2 the BTK model gives 1.8meV, while the Golubov-model gives 0.5meV, so there is a big difference between them. While the higher gap gives ratios $2\Delta/(k_B T_c)=8.0\pm0.7$ close to literature values, the second gap is much smaller compared to results obtained by other techniques.

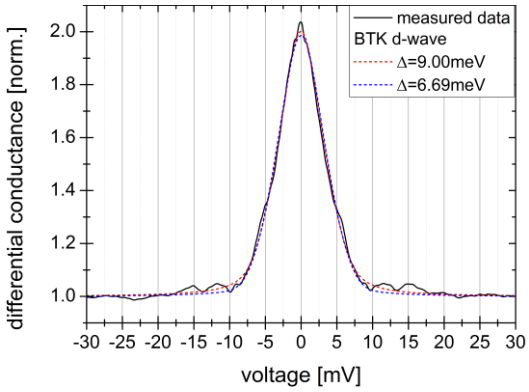

Fig. 2: *Normalized conductance of a planar junction with gold barrier and an area of 100 µm × 100 µm at T=7.9K.*

Comparing the spectrum of the edge-type junction to one of a planar junction one can see clear differences. The spectrum in fig. 2 does not show a typical s-wave behavior, which will cause a double peak or plateau shape. But the spectra of planar junctions with gold barrier show a zero-bias peak with nearly linear rise of conductance. Additionally the value at $V = 0$ is higher than 2, which is not possible in standard s-wave symmetry. Also for the s+- case such value is connected with the occurrence of side dips, which are not observed here. Nevertheless this spectrum can be modelled using a d-wave symmetry for the order parameter Δ. However, the fit can have big uncertainties of the obtained gap values. As one can see, fits with $\Delta = 9.00$meV and 6.69meV are possible, with slightly different values of Z and the Dynes-parameter Γ. The temperature dependence (fig.3) of the fitted gap values show a BCS curve up to 14K but deviates with smaller values for $14\text{K} < T < T_c$.

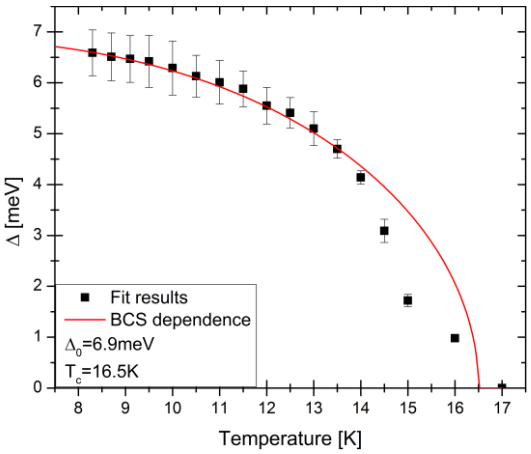

Fig. 3: *Temperature dependence of the gap values obtained from the planar junction compared to BCS.*

We thank the EC (project IRON-SEA), the DFG (SPP 1458), the DAAD and the Landesgraduiertenförderung Thüringen for financial support.

References

[1] S. Schmidt *et al.*, Phys. Proc. **36**, 82-87 (2012).
[2] S. Döring *et al.*, Physica C **478**, 15-18 (2012).
[3] G.E. Blonder *et al.*, Phys. Rev. B **25**, 4515–4532 (1982).
[4] A.A. Golubov *et al.*, Phys. Rev. Lett. **103**, 077003 (2009).
[5] I.I. Mazin, *et al.*, Phys. Rev. Lett. **101**, 057003 (2008).
[6] P.A. Lee and X.-G. Wen, Phys. Rev. B **78**, 144517 (2008).
[7] Q. Si, and E. Abrahams, Phys. Rev. Lett. **101** 076401, (2008).

Cryogenic Current Comparator for non-destructive beam current monitoring at particle accelerators and storage rings

René Geithner[1,2], Ralf Neubert, Jessica Golm[2], Febin Kurian[2,3], Hannes Reeg[3], Thomas Sieber[3], Marcus Schwickert[3], Paul Seidel, and Thomas Stöhlker[1,2,3]

[1]Institut für Optik und Quantenelektronik, Friedrich-Schiller-Universität Jena
[2]Helmholtz-Institut Jena
[3] GSI Helmholtzzentrum für Schwerionenforschung GmbH

In a joint effort of Institute of Solid State Physics at FSU Jena and HI-Jena a non-destructive beam monitoring system for particle beams in accelerators and storage rings based on the Cryogenic Current Comparator (CCC) principle was recently developed [1].

The CCC consists of a high-performance low-temperature DC superconducting quantum interference device system, a superconducting toroidal pick-up coil and an extremely effective meander-shaped superconducting niobium shield. This device allows the measurement of continuous as well as pulsed beam currents in the nA-range. The resolution and the frequency response of the detector strongly depend on the toroidal pick-up coil and its embedded ferromagnetic core.

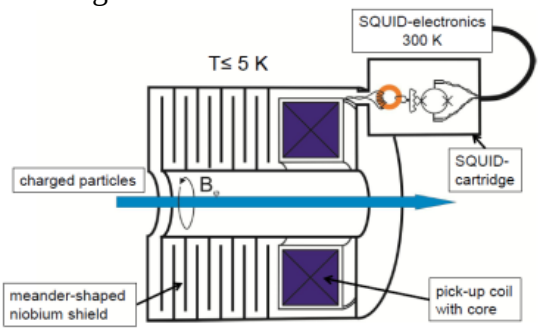

Fig. 1: *Schematic view of the CCC. Only the azimuthal magnetic field of the beam current passes the meander shaped shielding, all other magnetic field components are highly attenuated. The azimuthal magnetic field induces screening currents in the superconducting pick-up coil, which are detected by the SQUID sensor. Because of the superconductivity of all sensing parts, the CCC is able to detect continuous as well as pulsed beam currents.*

The current spectral density $\langle I^2 \rangle$ of a coil at a temperature T could be calculated with the Fluctuation-Dissipation-Theorem (FDT) and the measured frequency dependent serial inductance L_S (ν) respectively serial resistance R_S (ν) in the equivalent circuit diagram of a real coil [2], whereas R_S (ν) represents the total losses:

$$\left\langle I^2 \right\rangle = 4k_B T \int \frac{R_S(\upsilon)}{\left(2\pi\upsilon\left(L_{SQUID} + L_S(\upsilon)\right)\right)^2 + \left(R_S(\upsilon)\right)^2} d\upsilon \quad .(1)$$

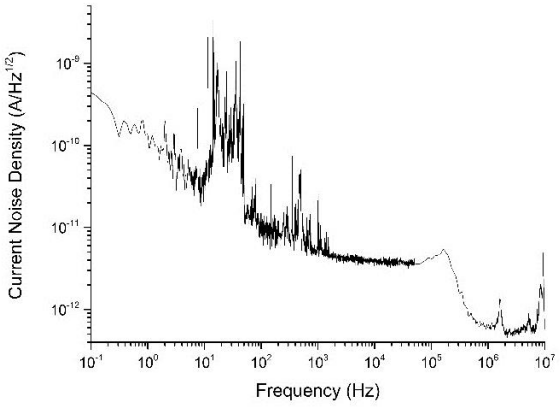

Fig. 2: *Current noise density of the improved FAIR-CCC with Nanoperm M764 core, matching transformer and Supracon SQUID sensor CP2 blue. A Magnicon XXF-1 electronics was used. The bandwidth of the SQUID system was adjusted to 7.49 GHz.*

Investigations of both the temperature and frequency dependence of the relative permeability and the noise contribution of several nanocrystalline ferromagnetic core materials were carried out to optimize the CCC with respect to an improved signal-

to-noise ratio and extended transfer bandwidth [3].

The current noise of the CCC could be decreased by a factor of five compared to previous systems [4] (see figure 2).

This decrease results from the usage of iron-based nanocrystalline Nanoperm as core material for the pick-up coil. With this optimized CCC a noise limited current resolution of 1 nA should be achievable in the disturbed environment of an accelerator [3].

The bandwidth of the CCC could not be measured in a direct manner yet due to the lack of a suitable high-bandwidth current source. In the case of the noise measurements the SQUID system bandwidth was adjusted to 7.49 GHz. A CCC bandwidth of 200 kHz is estimated from the decrease of the current noise in this frequency range.

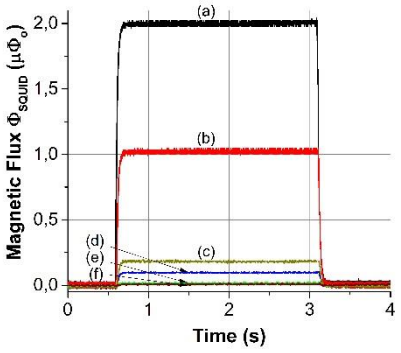

Fig. 3: *Response of the FAIR-CCC to a rectangular current signal of 2 µA (a), 1 µA (b), 200 nA (c), 100 nA (d), 20 nA (e) and 10 nA (f) applied to a beam simulating wire along the beam axis.*

Figure 3 shows the response of the FAIR-CCC to a rectangular current signal of 2 µA (a), 1 µA (b), 200 nA (c), 100 nA (d), 20 nA (e) and 10 nA (c) applied to a beam simulating wire along the beam axis. The bandwidth of the SQUID system was adjusted to 217 kHz. There is no low pass filter or time-averaging used.

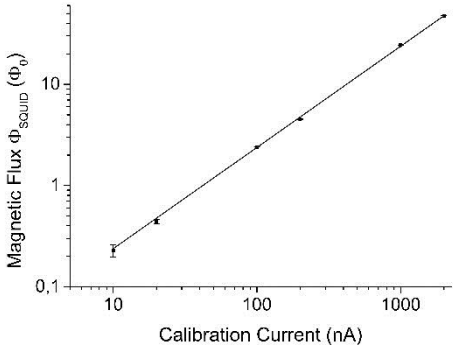

Fig. 4: *Peak-to-peak value of the step function response vs. the calibration current.*

Figure 4 shows dependency of the peak-to-peak value of the step function response form the applied current. The transfer function shows a high dynamic range with a linear behavior from 10 to 2000 nA. From this plot the overall current sensitivity is calculated to be 42 nA/ Φ_0.

For the international FAIR project at Darmstadt it is foreseen to install several CCC detectors at the high-energy transport beam lines. Here, beam currents in the range between 10^{-4} and 10^{-2} mA are to be expected.

In addition the installation of a CCC system at AD at CERN as well as at CRYRING is planned for highly accurate absolute current measurements at low beam energies and small particle numbers for ions as well as for antiprotons.

References

[1] R. Geithner *et al.*, IEEE Trans. Appl. Supercond . **21**(3), 444-447 (2011).

[2] R. Geithner *et al.*, Cryogenics. **54**, 16-19 (2013).

[3] R. Geithner *et al.*, Proc. IBIC 2014, Monterey, USA. WECZB1, (2014).

[4] R. Geithner *et al.*, Rev. Sci. Instrum. ***82***, 013302 (2011).

Set up of a Rotating Wave Plate Polarimeter for measuring stress induced birefringence in silicon at 1550 nm

René Glaser, Christian Schwarz, Daniel Heinert and Ronny Nawrodt

Interferometric gravitational wave detectors rely on the use of linear polarized light. Any disturbance from this polarization will limit the sensitivity. A possible element to change the polarization within the interferometer can be found in the input test masses (see [1] for example), where light passes the element. Load induced birefringence and permanent birefringence from crystal growth may disturb the linear polarization. For this reason the birefringence of the silicon input test masses should be well known for the application in a detector. A Rotating Wave Plate Polarimeter (RWPP) was set up to investigate the photoelastic behavior of silicon.

Due to its cubic crystal structure, silicon in an equilibrium state is optical isotropic and therefore non-birefringent. Applying a mechanical stress to the silicon crystal, the crystal structure will change to the tetragonal case and the material becomes optical anisotropic and therefore birefringent. This effect is called photoelasticity and is also applicable to non-crystalline materials [2]. This behavior can be described by the stress-optic law

$$n_x - n_y = C(\sigma_x - \sigma_y)$$

for the refractive indices n_x, n_y in x- and y-direction for light propagating in the z-direction. The change of the refractive indices is connected to the principle stresses σ_x, σ_y by the photoelastic coefficient C, which depends on the material and its orientation in relation to the applied stresses [3].

A schematic of the setup is shown in Figure 1. The important parts are the rotating quarter wave plate and the polarizer used as an analyzer in front of the detector. Together they form the polarimeter. The wave plate and polarizer in front of the sample are used to create linear polarized light in an arbitrary direction. A diode laser emitting at a wavelength of 1550 nm is used. The light is detected by a Ge photodiode and its signal is recorded by an analog/digital converter board on a PC.

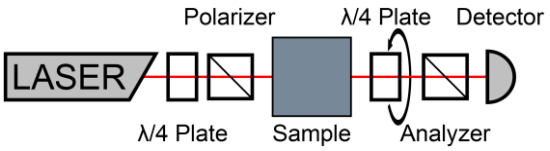

Fig. 1: *Schematic of the setup. The RWPP consists of the rotating quarter wave plate and the polarizer (analyzer) in front of the detector.*

The whole setup, except the sample, is mounted on rails and linear stages, providing the possibility to perform lateral scans along the sample.

For the measurement the quarter wave plate rotates continuously by 360 degree and the signal of the photodiode is sampled for one revolution. The recorded signal can be described by the following equation [4]

$$I(\phi) = \frac{1}{2}\left[\left(S_0 + \frac{1}{2}S_1\right) + S_3 \sin 2\phi + S_1 \cos 4\phi + S_2 \sin 4\phi\right].$$

The so called Stokes parameter S_i can be obtained by analyzing the Fourier amplitudes of the recorded angular signal.

Each parameter describes a different part of the light, as shown in Figure 2.

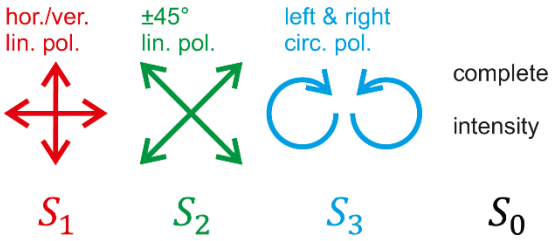

Fig. 2: *Each Stokes parameter describes a different part of the light.*

In the experiment linear polarized light is used. If the sample shows no birefringence, the linear polarization state will not change and the signal does not contain a S_3 component. If the sample is birefringent it adds a small circularly polarized part, which can be seen as a non-vanishing S_3 component.

In figure 3 a lateral scan of a silicon substrate is shown. The dimensions of the sample are a diameter and a length of 100 mm. In the figure the supporting structure is indicated by shaded circles and the outline of the sample is indicated by a dashed line.

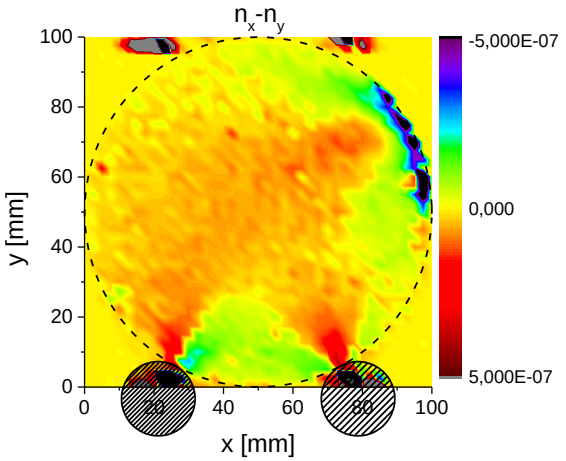

Fig. 3: *Birefringence of a silicon substrate, measured with the presented setup.*

The measurement shows a region with strong birefringence close to the supporting structure, caused by the gravitational load of the own mass of the sample. The dark structure at the top right of the substrate is caused by a damaged surface, also a source for stress and therefore for birefringence.

The measurement shows, that the setup is able to determine differences of the refractive indices in the range of 10^{-8}.

Further measurements will determine the photoelastic coefficients of silicon for different crystal orientations and their temperature dependence.

This work was supported by the Aspera/Appec project "ET R&D" under contract 05A13SJ1.

References

[1] G. M. Harry *et al.*, Classical Quantum Gravity. **27**, 084006 (2010).

[2] J. F. Nye, Physical Properties of Crystals Their Representation by Tensors and Matrices. Clarendon Press, Oxford (2008).

[3] K. Ramesh, Digital Photoelasticity Advanced Techniques and Applications. Springer, Berlin (2000).

[4] E. Collet, Polarized Light Fundamentals and Applications. Marcel Dekker Inc., New York (1993).

Synchronization of separately heated Josephson junctions

Alexander Grib[1] and Paul Seidel

[1]*Physics Department, Kharkiv V. N. Karazin National University, 61022, Kharkiv, Ukraine*

The essential progress in the creation of local sources of sub-mm radiation was made in both experiments and theory on synchronization of radiation from intrinsic Josephson junction arrays in high temperature superconductors [1,2]. It was observed that the temperature along the radiating sample was changed up to the appearance of 'hot spots', i.e. places in the sample which are overheated above the critical temperature of the superconductor [3]. The normal resistance which appears in the place of the hot spot can shunt intrinsic junctions along the height of the mesa structure, providing both resistive and inductive feedback for synchronization. At the same time, junctions around the hot spot have also different temperatures along the height of the mesa. Junctions near the surface of the mesa have the temperature of the bath whereas the temperature of junctions inside the mesa is higher. We show that just this inequality of temperatures along the height of the mesa structure can lead to the appearance of the additional strong mechanism of synchronization [4]. We consider the chain of two junctions which are externally and separately heated to different temperatures (Fig.1a). We assume that one of these junctions is placed on the surface of the mesa structure and another is placed inside the mesa structure, so their temperatures are different. The model system includes also the feedback resistive loop with some inductance (Fig.1a) analogously to the shunting resistance produced by the hot spot.

To find IV-characteristics of junctions,

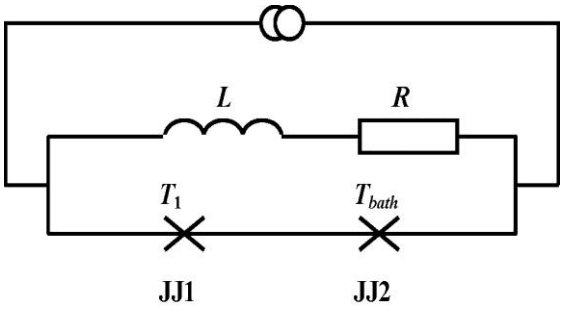

Fig. 1: *The scheme of the system. Josephson junctions (crosses) have different temperatures T_1 and T_2.*

one must solve dynamic equations for phase differences across junctions together with the differential equation for the current in the circuit [4].

Now we describe the changes of parameters of junctions caused by the temperature. Close to the critical temperature T_c, the dependence of the characteristic voltage on the temperature can be expanded to values of the first order [4]:

$$V_{ci}(T_i) = V_{ci}(T_{bath}) + \frac{dV_{ci}}{dT}(T_i - T_{bath}), \quad (1)$$

where T_{bath} is the temperature of the cryostat, $dV_{ci}/dT \approx -3.89 \cdot 10^{-4}$ V/K for high-temperature superconductors [4]. For clarity, we assume $I_{c1}>I_{c2}$ for $T_1=T_2=T_{bath}$ and $V_{c1}=V_{c2}=V_c$ at T_{bath}. In the process of calculations one should set parameters $I_{c1,2}=I_{ca}(1\pm\delta)$ with $I_{ca}=(I_{c1}+I_{c2})/2$ and δ is spread of critical currents at the temperature of the cryostat. The difference of temperatures between each of the *i*-th junction and the temperature of the cryostat is equal to $\Delta T_i=T_i - T_{bath}$. We assume $\Delta T_2 =0$ in all calculations. Then the

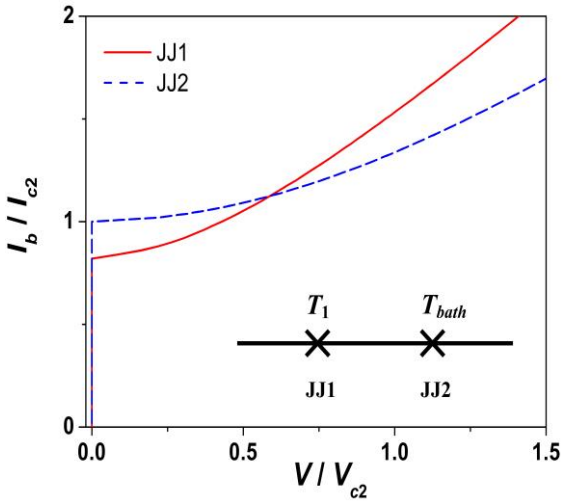

Fig. 2: *IV-characteristics of junctions without the LR-shunt for ΔT_1=1 K, ΔT_2 =0. Red solid line is for the junction 1, and blue dashed line is for the junction 2. The high-frequency scheme is shown in inset. Parameters of junctions: I_2=1 mA, δ=0.16, $V_c(T_{bath})$ = 1 mV, C_{j1} =C_{j2} =0.16 pF, R=1 Ohm, L=1.3 pH.*

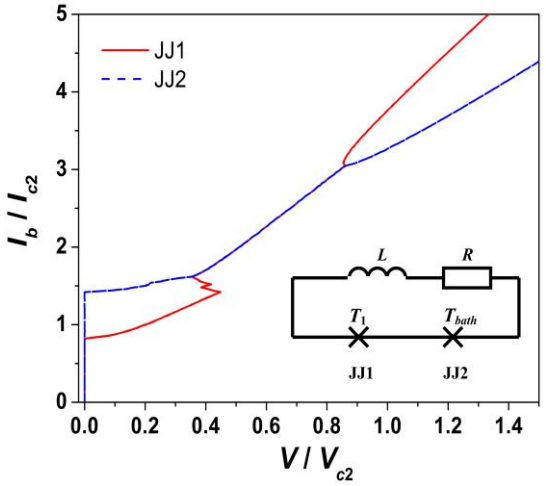

Fig. 3: *IV-characteristics of junctions with the LR-shunt for ΔT_1=1 K, ΔT_2 =0. Parameters of calculations and notifications are the same as in Fig.2. The high-frequency scheme is shown in inset.*

new value of I_{c1} is calculated for the given ΔT_1 and the relation $I_{c1}=V_{c1}/R_{J1}$ with the use of Eq. (1). Finally, this value of I_{c1} is substituted in the system of equations for the calculation of IV-characteristics.

IV-characteristics of junctions without the shunt are presented in Fig. 2 IV-curves for junctions in the shunted chain are shown in Fig. 3. It is seen that in Fig. 2 IV-curves cross each other at some voltages and they are coincide in Fig. 3 in the same range of voltages. Our calculations show that oscillations of voltages over junctions are synchronized in this range. The mechanism of synchronization is as follows. If the junction with larger critical current (the junction 1 in our case) is heated, its critical current decreases and become smaller than the critical current of the second junction. IV-characteristics of junctions cross each other (Fig. 2) and the ac feedback current can easily synchronize both junctions. Our calculations show that the maximal tolerant spread of critical currents is about 0.15-0.20. This value is comparable with the maximal tolerant spread for the strongest synchronizing loads such as the resonator and the transmission line.

In conclusion, we showed that the increase of the temperature of the junction with larger critical current in the chain lead to mutual in-phase synchronization. In the mesa structure of high-temperature superconductors the hot spots act like shunts and can produce synchronization of junctions placed in different 'colder' parts of the mesa structure by means of the described here mechanism.

References

[1] L. Ozyuzer *et al*., *Science* **318**, 1291-1293 (2007).

[2] A. Grib, M. Mans, M. Büenfeld, J. Scherbel, F. Schmidl, H. Schneidewind, and P. Seidel, IEEE Trans. Appl. Supercond. **24**, 1800205.

[3] S. Guénon, *et al*., Phys. Rev. B **82**, 214506 (2010).

[4] Alexander Grib and Paul Seidel, Phys. Status Solidi **B 251**, 1040–1044 (2014).

Thermal noise of free charge carriers in semiconductors

Daniel Heinert, Angus Bell[1], Gianpietro Cagnoli[2], Jerome Degallaix[2], Gianluca Gemme[3], Stefan Hild[1], Jim Hough[1], Yuri Levin[4], Harald Lück[5,6], Iain W. Martin[1], Sheila Rowan[1], Sergey P. Vyatchanin[7] and Ronny Nawrodt

[1]*SUPA, School of Physics and Astronomy, Institute for Gravitational Research, University of Glasgow, Glasgow G12 8QQ, United Kingdom*
[2]*Laboratoire des Mat´eriaux Avanc´es, IN2P3/CNRS, Universit´e de Lyon, 7 Avenue Pierre de Coubertin, Villeurbanne 69100, France*
[3]*INFN, Sezione di Genova, I-16146 Genova, Italy*
[4]*School of Physics and Monash Center for Astrophysics, Monash University, Post Office Box 27, Victoria 3800, Australia*
[5]*Albert-Einstein-Institut, Max-Planck-Institut f¨ur Gravitationsphysik, D-30167 Hannover, Germany*
[6]*Institut für Gravitationsphysik, Leibniz Universität Hannover, D-30167 Hannover, Germany*
[7]*Faculty of Physics, Moscow State University, Moscow 119991, Russia*

The search for gravitational waves and their direct detection has been a demanding challenge for more than the last four decades. Due to their faint effect on spacetime former instruments were not able to directly detect gravitational waves. However the second generation of interferometric gravitational wave detectors like Advanced LIGO [1] and Advanced VIRGO [2] is expected to show such a sensitivity that gravitational waves should be detected at least by a rate of a few per month. On this way towards the first direct detection of gravitational waves an important milestone has been achieved by the first locking of the Advanced LIGO detectors in 2014 already exceeding all sensitivities obtained before. The first direct detection will give birth to the field of performing astronomical observations by studying gravitational waves. This will promise new insight into cosmological objects like e. g. black holes or neutron stars. At the same time this goal demands for even more sensitive detectors increasing the accessible range of such an instrument.

Thermal noise has been identified to severely limit the sensitivity of previous detectors and is one of the dominating effects hampering a detection. Its understanding, modelling and optimization have been a corner stone for the design of Advanced LIGO promising the first direct detection in the near future. For the purpose of a GW based astronomy thermal noise has been further improved in the design of the Einstein Telescope (ET) as a third generation detector [3].

The ET Design Study proposes a combination of two detectors. ET-HF is aiming at high frequencies and will be operated at room temperature showing a high laser power to reduce shot noise and large fused silica mirrors and suspension to decrease thermal noise. In contrast at low frequencies ET-LF is planned to use low laser power and test masses and suspensions at low temperatures. Decreasing temperature as the driving force for thermal noise promises a further increase of sensitivity. For this purpose fused silica as the standard substrate material of previous GW detectors is not suited due to the strong increase of its

mechanical loss at low temperatures. Due to the fluctuation-dissipation theorem [4] this will result in an increased level of noise. In contrast silicon shows a low mechanical loss at low temperatures [5] and is available in monocrystalline samples at large diameters.

A change in material is always accompanied by a change of its physical properties and parameters and can result in the additional noise processes. While the theory of Brownian and temperature fluctuations covers the case of silicon as well a major difference can be found in the electric properties of both materials. Here silicon as a semiconductor exhibits freely moving charge carriers that are absent for fused silica as an insulator. In silicon the concentration of free carriers will undergo fluctuations due to their motion, e.g. driven by diffusion. As the refractive index of silicon turns out to depend on the concentration of free carriers [6] such an effect will lead to refractive index fluctuation. Consequently any transmissive optics in an interferometric gravitational wave detector like the beam splitter or the input test masses will undergo a new kind of thermal noise – carrier density (CD) noise.

For a rough approximation of this effect we consider the case were only diffusion drives the motion of free carriers in silicon. Further the calculation is restricted to doped silicon exhibiting only one kind of free charge carrier. Then the Langevin equation for their concentration n follows

$$\frac{\partial n}{\partial t} - D\Delta n = F(\vec{r}, t)\,, \qquad (1)$$

where D denotes the diffusional constant and $F(\vec{r}, t)$ the driving force of carrier motion. In analogy to previous work on thermorefractive noise [7] in the adiabatic limit (fluctuations with periods smaller than the characteristic time of diffusion) the spectral density of fluctuations of the carrier density can be obtained. For cylindrical samples (thickness H) and a transmissive beam of Gaussian shape (radius r_0) this would lead to a noise level of

$$S_n^{CD}(\omega) \simeq \frac{4}{\pi} k_B T \frac{\partial n}{\partial \mu} \frac{D}{H r_0^4} \frac{1}{\omega^2}\,. \qquad (2)$$

Here μ represents the chemical potential of the carriers and $k_B T$ the thermal energy.

For silicon at doping densities of above 10^{14} cm^{-3} the respective level of CD noise will exceed the level of thermo-refractive noise at temperatures above 100 K representing a serious effect in future detectors. Nevertheless at lower temperatures the freeze out of carriers will result in a strong decrease of CD noise.

So far no electronic interaction of the particles has been considered. This point remains as an open task for future investigations and for a refined estimate of CD noise. This might affect not only the field of GW detectors but e.g. a huge number of applications in the micro- and nano-optic as well.

References

[1] G. M. Harry et al., Class. Quantum Grav. **27**, 084006 (2010).

[2] F. Acernese et al., Class. Quantum Grav. **32**, 024001 (2015).

[3] M. Punturo et al., Class. Quantum Grav. **27**, 194002 (2010).

[4] H. B. Callen et al., Phys. Rev. **83**, 34 (1951).

[5] D. F. McGuigan et al., J. Low Temp. Phys. **30**, 621 (1978).

[6] R. A. Soref et al., IEEE J. Quant. Electron. **QE-23**, 123 (1987).

[7] V. B. Braginsky et al., Phys. Lett. A **271**, 303 (2000).

Mechanical loss of indium

Gerd Hofmann, Dan Chen[1] , Julius Komma, Frank Schmidl, Christian Schwarz, Daniel Heinert, Kazuhiro Yamamoto[1], Ronny Nawrodt

[1]Institute for Cosmic Ray Research, The University of Tokyo, Kashiwa-no-Ha, Japan

Currently the first generation of interferometric gravitational wave detectors from the mid-90s namely GEO600, LIGO, and Virgo are partly offline or rather discontinued in case of TAMA300 to pave the way for upgrading to the second generation of detectors [1 and refs. therein]. These detectors will incorporate novel techniques to enlarge the observable space by a factor of thousand. The so called advanced detectors LIGO [2], Virgo [3], and GEO600 [4] will stay along fused silica as test mass material but KAGRA [5,6] is the first detector which will utilize crystalline sapphire at cryogenic temperatures.

The suspension of the test masses is a complex chain of pendulums and springs which provides a proper vibration isolation. Moreover to give a low thermal noise [7] low loss materials are inevitable in the last stage of the chain. Thus aside from the test mass itself also the connection to the penultimate mass is of great importance. In KAGRA sapphire fibers are considered to be connected to the test mass either by hydroxide catalysis bonding, direct bonding [] or by indium bonding.

To study the mechanical loss ϕ of an indium bond between sapphire two cylindrical sapphire samples of 30 mm diameter and 50 mm respectively 70 mm were joined. A 100 µm thick indium foil was put between the samples and all heated slightly above the melting point of 156.6°C while a pressure of 23.6 kPa was applied. The indium bond layer lacks 5 % of the interface due to dewetting (see Fig. 1). The overall thickness of the layer was obtained by optical microscopy to be 13.6±2.0 µm.

Fig. 1: *Indium bond layer between two sapphire substrates.*

The mechanical loss ϕ is defined as energy ΔE lost per cycle of a vibration at a frequency f_0 with. It can be obtained as:

$$\phi = \frac{\Delta E}{2\pi E_{tot}} = \frac{1}{\pi f_0 \tau}$$

by measuring the ring down time τ. In this case the whole energy loss ΔE is given by the sum of sapphire ΔE_{bulk} and the indium bond ΔE_{bond} thus it reads:

$$\phi_{meas} E_{tot} = \phi_{sub} E_{sub} + \phi_{bond} E_{bond} .$$

The mechanical loss contributed by the sapphire ϕ_{sub} itself can be obtained from a single piece of crystal as a reference sample of the same size as the bonded one. The results of that measurement are given by the lower solid symbols in Fig. 3. Also the results for the bonded sample (Fig. 3, open symbols) are given. Thus it is

obvious that $\phi_{meas} \gg \phi_{sub}$. Further as the bond layer is very thin nearly all the energy is stored in the substrate and one can assume that $E_{sub} \approx E_{tot}$. Thus the loss of the bond is given by:

$$\phi_{bond} \approx \phi_{meas} \frac{E_{tot}}{E_{bond}}.$$

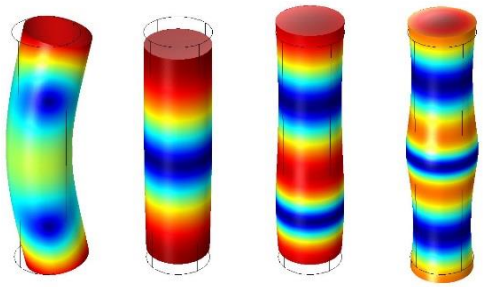

Fig. 2: *Mode shapes at 17 kHz, 44 kHz, 89 kHz, and 132 kHz of the sapphire samples.*

The ratio of the energies stored in the whole sample and in the bond where calculated by a finite element analysis using COMSOL for all four modes (Fig. 2). The final results of the extracted mechanical loss of an indium bond are shown by the upper solid symbols in Fig. 3.

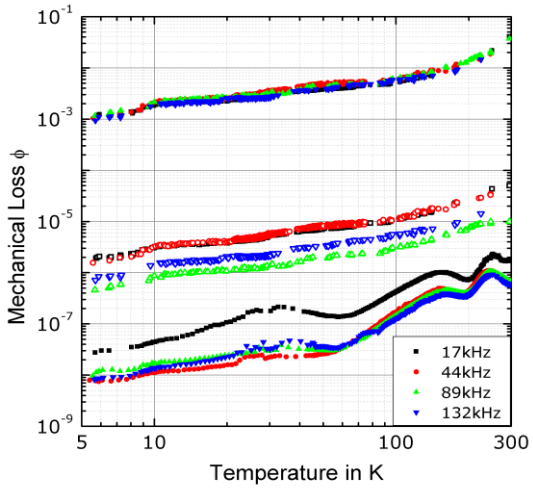

Fig. 3: *Mechanical loss of the reference sample (lower solid symbols), the bonded sample (open symbols), and the indium bond (upper solid symbols).*

For the desired temperature of 20 K in KAGRA [5] the mechanical loss of the indium bond between the sapphire samples is in the order of 2×10^{-3} and increases up to 4×10^{-2} at room temperature. Kim and Ledbetter have measured the loss of pure polycrystalline indium at 295 K to be 3.2×10^{-2} [9].

Hence our measurement indicates hardly any increase in the loss at room temperature when using indium as a bond material compared to bulk. To our knowledge the low temperature results were so far measured for the first time and thus will drive the final design for KAGRA.

This work was supported by the DFG under the SFB TR7 grant.

References

[1] K. L. Dooley *et al.*, *arXiv preprint arXiv*:1411.6068 (2014).
[2] The LIGO Scientific Collaboration. Advanced LIGO (2014).
[3] F. Acernese *et al.*, *Class. Quantum Grav.* **32**, 024001 (2015).
[4] H. Lück *et al.*, *J. Phys.: Conf. Ser.* **228** 012012 (2010).
[5] K. Somiya, *Class. Quantum Grav.* **29**, 124007 (2012).
[6] Y. Aso *et al.*, *Phys. Rev. D* **88**, 043007 (2013).
[7] P. R. Saulson, *Phys. Rev. D* **42**, 2437-2445 (1990).
[8] T. Suzuki *et al.*, *J. Phys.: Conf. Ser.* **32** 309-314 (2006).
[9] S. Kim and H. Ledbetter, *Materials Science and Engineering*, **A 252.1**, 139–143 (1998).

Improving the Meissner screening of $YBa_2Cu_3O_{7-\delta}$ by gold nanoparticles

Christian Katzer, Evelyn Stilp[1], Elvezio Morenzoni[1] and Frank Schmidl

[1]Laboratory for Muon Spin Spectroscopy, Paul Scherrer Institut, CH-5232 Villigen PSI

During the last years a great deal of effort has been applied to optimizing the high-temperature (high-T_c) superconductor $YBa_2Cu_3O_{7-\delta}$ (YBCO). Now, the development of new growth processes [1] and the inclusion of highly effective pinning centers enables high growth rates and current carrying capabilities, respectively. Thus, YBCO appears to be the material of choice for the preparation of coated conductors [2]. Furthermore, very recently a new technique of locally embedding Au nanoparticles has been presented, allowing to locally affecting superconducting properties like the critical current density j_c and the critical temperature T_c [3]. This paves the way for a custom tailored current carrying capability in arbitrary patterns, which is especially important for superconducting sensor devices with an improved performance.

However, until now little is known about the effect of embedding Au nanoparticles on the microscopic superconducting parameters, such as the London penetration depth λ_L, which is also linked to the superfluid density n_s. Thus, we investigated three sets of YBCO thin films with and without Au particles by means of muon spin rotation (μSR) experiments [4]. To employ this method for thin films, low energy muons had to be used, which was only possible at the Swiss Muon Source of the Paul Scherrer Institute. The samples were prepared using an optimized pulsed laser deposition routine as described in [4].

To improve the statistics, four samples of each set were glued on a nickel coated aluminum plate and irradiated with low energy muons, produced by pion decay and moderated using a solid Ar/N_2 film. After reaccelerating the μ^+ by applying a bias voltage between 5 keV and 25 keV, the mean stopping depth of the muons could be varied at a range of 25-106 nm. After zero field cooling the samples, an external magnetic field of 8 mT was applied parallel to the film/substrate interface and perpendicular to the initial muon spin. Thus, the muon spin started a precession around the field direction with the frequency depending on the local field magnitude. Measuring the temporal evolution of this muon spin polarization by detecting the μ^+ decays positron, which is preferentially emitted in spin direction, thus allowed to measure the inhomogeneous local magnetic field distribution at the μ^+ site. To analyze the data, a London model profile resulting from an exponential decay of B_{ext} from both interfaces was used:

$$B = \begin{cases} B_{ext}\dfrac{\cosh[\frac{(z-z_0-d_{sc}/2)}{\lambda_{ab}}]}{\cosh(d_{sc}/2\lambda_{ab})} & z \geq z_0 \\ B_{ext} & z < z_0 \end{cases}$$

at which d_{sc} is the thickness of the superconducting layer, caused by a dead layer z_0 at the vacuum interface, which is due to the roughness of the sample surface. A simultaneous analysis of spectra measured at seven different implantation depths then allowed to determine the Meissner screening profiles (Fig. 1) and penetration depths. Interestingly, the dead layer at the vacuum interface was small for all sets of samples compared to bulk and other YBCO thin film measurements, indicating a very smooth surface.

Furthermore, also the dead layer at the substrate interface was significantly reduced by embedding Au nanoparticles. Since this layer of weak superconductivity is mainly caused by mechanical strain, introduced by the lattice misfit of substrate and YBCO film, one might conclude that this strain relaxes at the nanoparticles, leading to an improved interface. These findings are in excellent agreement with previous investigations [3, 5].

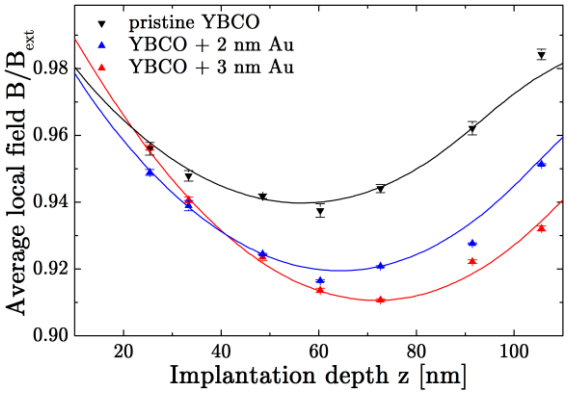

Fig. 1: *Meissner Screening profiles.*

As can be seen in Fig. 1, Au modified YBCO screens the external magnetic field better than conventional YBCO and thus exhibits a smaller penetration depth λ_L. Measuring μSR spectra at an energy corresponding to the minimal average local field for different *T*-values allowed obtaining the temperature dependence $\lambda_L(T)$.

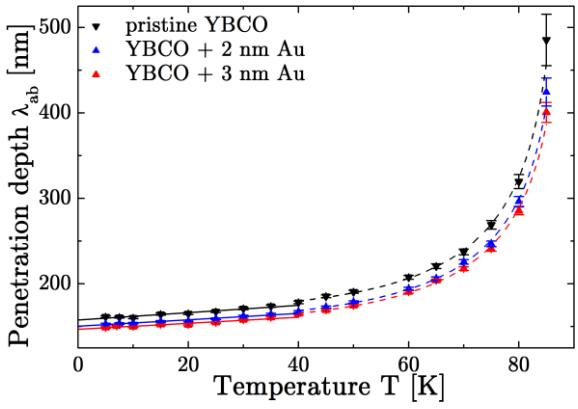

Fig. 2: *Temperature dependence of* λ_L.

The conventional as well as the Au modified YBCO sample sets show a linear decrease of the penetration depth below 35K, which is characteristic for a d-wave pairing. Since the slopes give information on the superconducting gap one can conclude, that embedding Au nanoparticles does not affect the cooper pairing within the experimental uncertainty. However, the presence of Au nanoparticles leads to a smaller value of $\lambda_L(0K)$, as one would expect for single crystalline bulk-samples. A possible explanation for this optimized magnetic penetration depth in Au modified YBCO could be given by an incorporation of Au atoms in the YBCO lattice [4]. However, this can be neglected, as we could show in xray diffraction measurements. Instead, we attribute the optimized penetration depth to a reduced defect density in Au modified YBCO, which is in excellent agreement with previous investigations [3].

In summary, we used low-energy muon spin spectroscopy to investigate the influence of Au on the microscopic superconducting parameter λ_L. Although the pairing mechanism seems to be unaffected, we noticed a decrease of the absolute penetration depth at 0K and thus an improved Meissner screening of an external field. We attribute this to a reduced defect density in Au modified YBCO.

References

[1] T. Ohnishi *et al.*, *J. Mater. Res.* **19**, 977 (2004).

[2] J. L. MacManus-Driscoll *et al.*, *Supercond. Sci. Techn.*, **23**, 034009 (2010) .

[3] C. Katzer *et al.*, *New J. Phys.* **15**, 113029 (2013).

[4] E. Stilp *et al.*, *Phys. Rev. B.*. **89**, 020510(R) (2014).

[5] V. Grosse *et al.*, *Phys. Status Solidi - RRL* **4**, 97 (2010).

Optical absorption measurement at cryogenic temperature on silicon wafers at 1550 nm

Julius Komma, Gerd Hofmann, Jerome Degaillaix[1], Angus Bell[2], Christian Schwarz, Daniel Heinert and Ronny Nawrodt

[1]Laboratoire des Matériaux Avancés, IN2P3/CNRS, Université de Lyon, 7 Avenue Pierre de Coubertin, Villeurbanne 69100, France, [2]Institute for Gravitational Research, SUPA University of Glasgow, G12 8QQ Glasgow, UK

There are two materials which are promising for future cryogenic interferometric gravitational wave detectors (GWD). On the one side there is sapphire which is the choice for the for the Japanese KAGRA detector which is under construction at the moment [1]. On the other side there is silicon which is the designated material for the future European GWD named Einstein Telescope [2].

For the design of the cryogenic parts of such a detector the knowledge of the optical absorption of the mirror material is crucial.

First measurements on silicon samples at low temperatures have been done in collaboration with groups in Lyon [3] and Glasgow. The measurements in Jena have been performed with a calorimetric setup [3] while results in Lyon and Glasgow have been obtained by an optical deflection method [4]. First results are shown in Fig. 1. All measurements have shown a minimum in the optical absorption of silicon around 100 K.

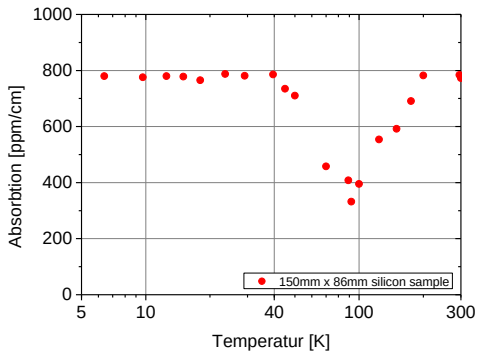

Fig. 1: *Temperature dependent optical absorption data at a wavelength of 1550 nm. The boron doped silicon sample has a cylindrical geometry with 150 mm diameter and a length of 86 mm.*

All measurements so far were done on bulk samples. This means that the samples are expensive and difficult to handle (polishing, surface characterization etc.). So we decided to upgrade our setup to measure wafers. An example for such a wafer piece is shown in Fig. 2. The challenge when using small samples is scattering light. The temperature sensor is fixed on the sample near the laser beam and absorbs all scattered light that reaches it.

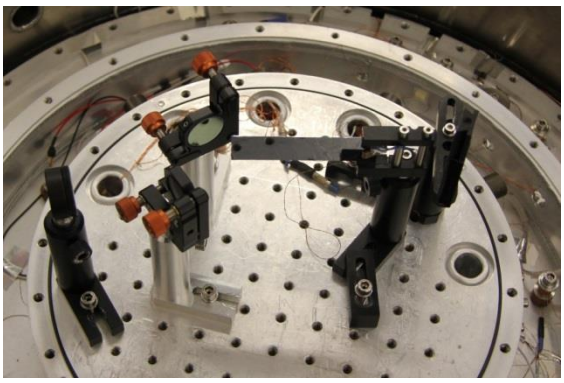

Fig. 2: *500 µm thick silicon wafer piece placed inside a special build helium cryostat. The mirrors are used to guide the laser beam through an optical window out of the cryostat.*

In Fig. 3 a typical heating and cooling curve for a calorimetric measurement is shown. The data evaluation is based on the

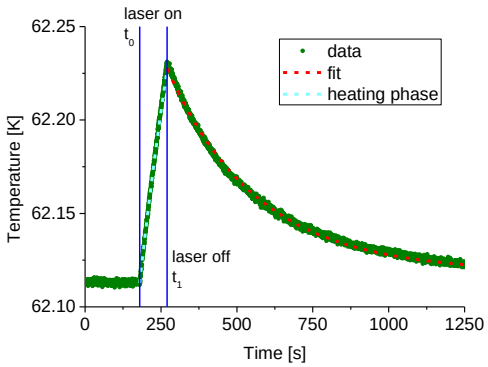

Fig. 3: *Example for the evaluation of the measured data. The loss parameter γ is specified by an exponential fit of the temperature decrease. This parameter is needed to calculate the optical absorption as explained in the text.*

differential equations which describe the heating by laser and the cool down back to the equilibrium temperature [5]:

$$T(t) = \begin{cases} 0 & t \le t_0 \\ \frac{\alpha P}{\gamma m C}\left(1 - e^{-\gamma(t-t_0)}\right) & t_0 < t < t_1 \\ T(t_1)\, e^{-\gamma(t-t_1)} & t > t_1 \end{cases}$$

Where T(t) is the time dependent temperature of the sample, α the absorption coefficient, P the laser power, m the mass of the sample, C the heat capacity and γ a loss coefficient dependent on the thermal coupling of the sample to the surrounding. The loss coefficient is determined by fitting the temperature decrease like shown in Fig. 3.

First results for a temperature dependent measurement on a silicon wafer are shown in Fig. 4. The three curves were measured with different types of dopants and although in different setups. The temperature dependent minimum is although visible so that for a detailed study of this behavior wafers can be used instead of bulk samples.

The absorption around room temperature in silicon is based on free carrier absorption [6] due to ionized donors. Cooling down the sample the donor states recombine and the populated states can now cause optical absorption. To verify this assumption further measurements are needed and will be done as next steps.

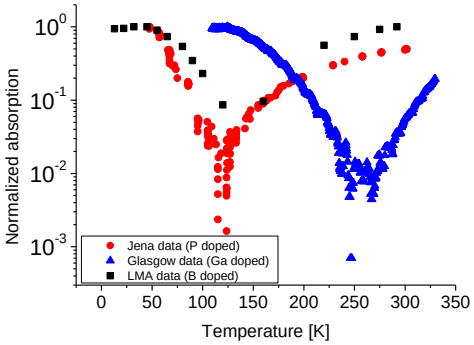

Fig. 4: *Temperature dependent absorption data measured in Jena, Glasgow and LMA with different doping.*

This work was supported by the DFG under contract SFB Transregio 7.

References

[1] K. Somiya *et al.*, *Class. Quant. Grav.* **29**, 124007 (2012).
[2] https://tds.ego-gw.it/ql/?c=7954.
[3] J. Degallaix *et al.*, *Class. Quant. Grav* ***31***, 185910 (2014).
[4] J. Degallaix *et al.*, *Optics Latters* **38**, 2047-2049 (2012).
[5] U. Willamowski *et al.*, *Applied Optics*. **37**, 8362-8370 (1998).
[6] W. Spitzer and H. Fan, *Phys. Rev.* **108**, 268-271 (1957).

Weak continues monitoring of a flux qubit - resonator system with intermediate coupling

S.N. Shevchenko[1], G. Oelsner[2], Ya. S. Greenberg[3],P. Macha[2], D.S. Karpov[1], M. Grajcar[4], U. Hübner[2], A.N. Omelyanchouk[1], E. Il'ichev[1], H.-G. Meyer[1], and P. Seidel

[1]B. Verkin Institute for Low Temperature Physics and Engineering, Kharkov, Ukraine
[2]Leibniz Institute of Photonic Technology, Jena, Germany
[3]Novosibirsk State Technical University, Novosibirsk, Russia
[4]Department of Experimental Physics, Comenius University, Bratislava, Slovakia

Nowadays, artificial quantum systems are in use in different fields of modern physics. One important realization exploits the quantum behavior of small Josephson junctions. For example, inserted into a superconducting ring they can form the analog of a real atom by means of an anharmonic oscillator. Since the energetic difference between the first two levels is usually much smaller than the distance to the third, often only the lowest two levels are considered. In this two level approximation they are described by the Hamiltonian

$$H = -\frac{\varepsilon_0}{2}\sigma_z + \frac{\Delta}{2}\sigma_x,$$

where the $\sigma_{x,z}$ are the Pauli matrices. The Hamiltonian includes an external controllable parameter, the energy bias ε_0, and an intrinsic one, the tunnel splitting Δ, given by the fabrication. The total energy splitting between the states is then $h\nu = \sqrt{\varepsilon_0^2 + \Delta^2}$.

Such systems often called superconducting qubits [1], have important advantages over real atoms: First, they are macroscopic systems and therefore couple very efficiently to external control fields. Second, their properties are well under control either by the fabrication or by external parameters and third these systems are scalable.

In experiments where such single qubits are coupled to cavities with similar eigenfrequenies, different effects known originally from quantum optics have been observed. To name some: the vacuum Rabi splitting [2,3], a single atom lasing [4] or the resonance fluorescence of a single qubit[5].

In our own work a similar system was considered. It consisted of a coplanar-waveguide-(CPW) resonator and a single qubit coupled to it. A strong driving signal is then applied in one of the harmonics of the resonator and leads to a dressing of the qubit states.

This influences not only the shape of the energy levels but also there population. In that way were able to achieve amplification and attenuation when fulfilling the resonance condition for the fundamental mode with the Rabi frequency of the driven qubit [6].

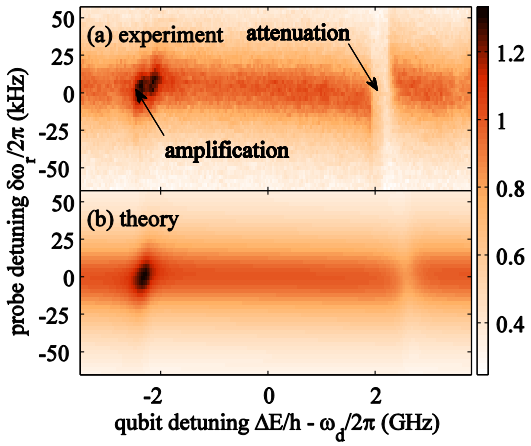

Fig.1: Measured a) and simulated b) normalized transmission amplitude of the resonator around the fundamental mode frequency as a function of the detuning between qubit and driving frequency. We find amplification and damping of the transmission signal depending on the sign of the detuning when the resonance condition between the Rabi levels of the driven qubit and resonator are fulfilled.

Nevertheless, when increasing the driving strength new resonance lines appeared (see Fig. 2). They show narrow regions of both amplification and attenuation, but could not be described with the model for describing the Rabi resonances used in [6].

Therefore, we introduce the doubly dressed qubit, to improve the theoretical description of the measurement data [7]. In a first step, the influence of the strong driving signal on the qubit is analyzed. Calculations show that a renormalization of the parameters in the qubit Hamiltonian around the k-th.

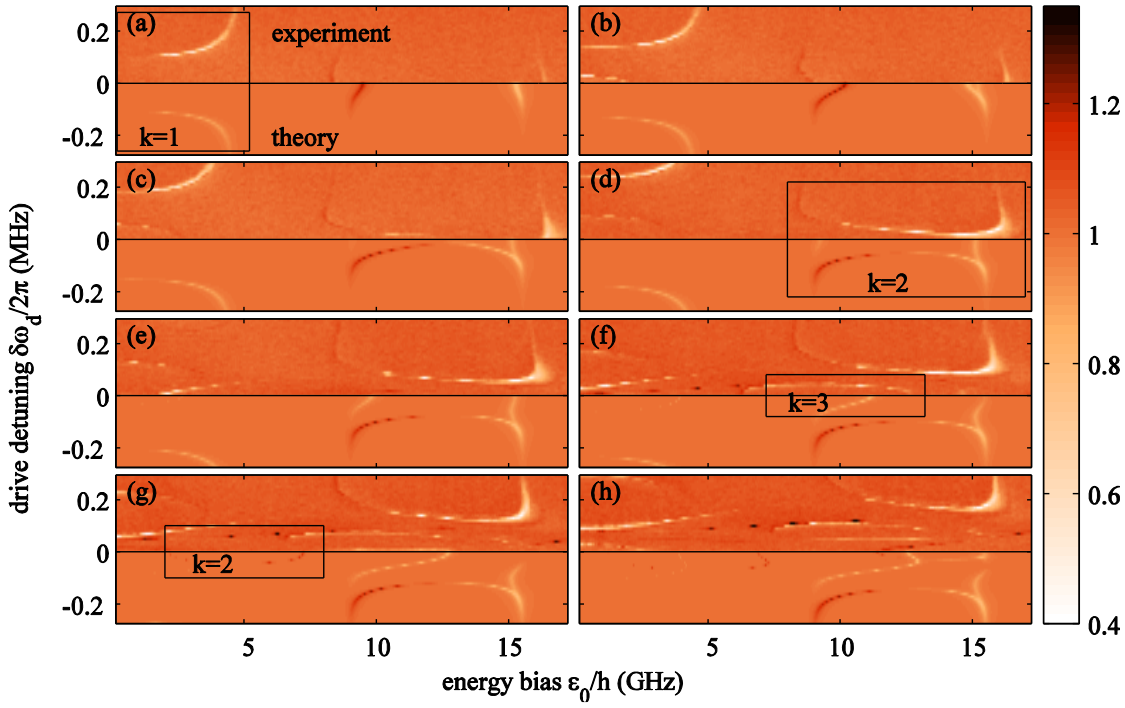

Fig.2: Normalized transmission amplitude at the resonators fundamental mode frequency on dependence of the qubits energy bias and the detuning between driving signal and qubit. From a) to h) the driving power is increased in 2 dBm steps. In each plot the region of positive detuning shows the experimental results while for negative detunings calculation results based on the doubly dressed states are shown. For different regions the calculation had to consider resonance conditions with different index k, which is marked by black rectangulars.

resonance ($\nu_q = k\nu_d$) accounts for the change of the energy levels and occupations. Then a set of new two level systems (one for each k) is found, where the renormalized bias is given by the detuning from the k-th resonance $\varepsilon_k = h\nu_q - kh\nu_d$ and the tunnel splitting is replaced by an oscillating Bessel function behavior $\Delta_k = \Delta \frac{kh\nu_d}{\varepsilon_0} J_k\left(\frac{A_d}{h\nu_d}\frac{\varepsilon_0}{h\nu_q}\right)$, where A_d is the amplitude of the driving. Furthermore, the relaxation and excitation rates are modified and depend on the sign of ε_k.

The second dressing then occurs between one of these two level systems and the fundamental resonator mode, which is expressed by the standard Hamiltonian

$$H_k = -\frac{\varepsilon_k}{2}\sigma_z + \frac{\Delta_k}{2}\sigma_x + h\nu_r a^+ a - g(a^+ + a)\sigma_z + A_p(ae^{i\omega_p t} + a^+ e^{-i\omega_p t}).$$

Here, a+ and a are the photon creation and annihilation operators for the fundamental mode, A_p and $\omega_p/2\pi$ describe amplitude and frequency of the probing signal, respectively and the coupling energy to the fundamental mode is g. Similar methods as for a simple qubit coupled to a resonator [2] can then be used to calculate the resonators transmission. We tested our method first for the resonance k=1, which corresponds to the Rabi level case. The correspondence between measurement and theory shown in Fig.1 is well, both qualitatively and quantitatively. Also for stronger driving the resonance conditions leading to Fig.2 were identified. An overlay of the results for many different k gives a good correspondence between measurement and theory, which demonstrates the value of our approach.

References

[1] J.E. Mooij, et al., Science **285**, 1036 (1999)
[2] G. Oelsner, et al., Phys. Rev. B **81**, 172505 (2010)
[3] A. Abdumalikov, et al., Phys. Rev. B **78**, 180502(R) (2008)
[4] O. Astafiev, et al., Nature **449**, 588 (2007)
[5] O. Astafiev, et al., Science **327**, 840 (2010)
[6] G. Oelsner, et al., Phys. Rev. Lett. **110**, 053602 (2013)
[7] S. Shevchenko, et al., Phys. Rev. B **89**, 184504 (2014)

Optical absorption of silicon near its band edge and at 1550 nm

Philip Pastrik, Christian Schwarz and Ronny Nawrodt

In order to construct next generation gravitational wave detectors, it will be necessary to reduce thermal noise by the use of cryogenic optics. Silicon is a promising material for the test mass as it has proven to can be produced in large size and has a low intrinsic mechanical loss [1].

However, while silicon is of great interest as being material of the test mass [2], little is known about its optical properties at cryogenic temperature.

To improve the sensitivity of the GW detector, a high light power is used. The test mass is hence exposed to irradiation with light power up to several tens of kilowatts. To minimize the heat resulting from the absorption of radiation, the used laser emits at 1550 nm due to a low optical absorption in silicon.

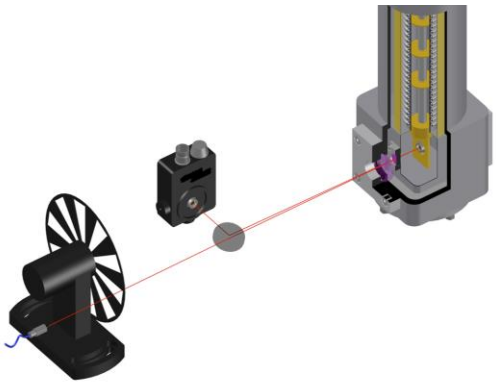

Fig. 1: *Schematic setup for measurement of the opto-electronical absorption of silicon. Monochromatic light from a monochromator passes a chopper, beam-splitter and hits a photodiode (BPX61). The reflected light is detected by a photodetector.*

Unfortunately, in the case of low absorption it is nearly impossible to determine a value for absorption by means of direct optical measurements. An alternative approach is to investigate the influence on other physical values. For example by measure the change of temperature during irradiation [3].

An alternative to study a contribution to the total absorption in silicon is to measure the conversion of light to charge carriers.

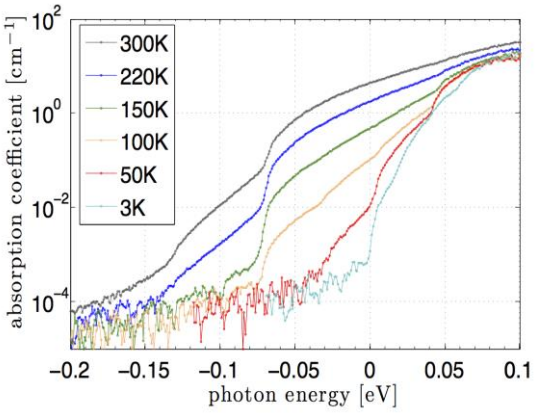

Fig. 2: *Absorption coefficient of silicon obtained from investigations of a Si photodiode in the NIR. The photon energy is given as the deviation from the band gap energy.*

Measuring the output signal of a photodiode is a simple way to detect the dependence on temperature and incidence of light. By the use of a Lock-In amplifier it was possible to measure the smallest changes of absorption. The schematic setup is given in Fig. 1. It must be kept in mind that a photodiode is an electronic component with a p-n junction; hence we need to consider not just energy levels from the intrinsic silicon, but from the dopant as well.

The measured values are summarized in Fig. 2. As long as the photon energy is larger than the band edge a strong optical

absorption occurs. As soon as the photon energy gets below the energy of the band gap absorption drops dramatically.

Silicon is an indirect semiconductor. Each photon absorption process involves a phonon emission or absorption process to fulfill the conservation of momentum. At energies above the energy gap an emission of a phonon occurs as the energy of the photon is sufficient to excite the electron over the indirect gap and the residual energy is used to create one or more phonons. As the creation of phonons does not involve thermal excitation this process is expected to be weakly temperature dependent. This is confirmed by the measured results. On the other side at photon energies below the energy gap only the absorption of a phonon during the process can fulfill the conservation of energy and momentum. Thus, the phonons of the silicon sample need to be thermally excited to support these processes. As a consequence this part of the measurement is expected to be strongly temperature dependent, as seen in Fig. 2.

The possible application of silicon optics in future gravitational wave detectors is discussed at 1550 nm which would correspond to -0.3 eV in Fig. 3. It is clear that the classical setup cannot be used to measure the opto-electronical absorption at this wavelength as the setup is limited by noise. Using a monochromator as a light source is not useful anymore. In order to gain more insight in the absorption process a tunable laser source was used to illuminate the photodiode. Here the optical power could be increased from sub-µW (as with the monochromator) to up to 5 W. Only laser powers in the range of a few 10 to 100 mW have been used to avoid an additional heating of the sample. Fig. 3 shows a first result of such a measurement. As expected the absorption of the device drops by nearly 3 orders of magnitude while cooling. Surprisingly, below 50 K the absorption increases again. At very low temperatures the absorption is getting smaller having roughly 1/10 of the initial value at room temperature.

The obtained result is similar to observations that have been done by means of calorimetric and deflection studies to measure the optical absorption [4]. The underlying mechanisms are not understood yet. First hypothesis include the absorption of neutral donor states at cryogenic temperatures. Further studies are needed and the simple technique to test the electronical absorption of a photodiode might be useful to support these activities.

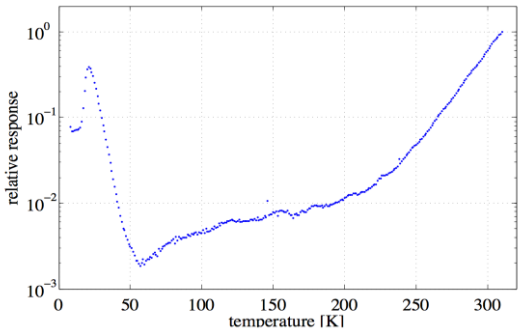

Fig. 3: *relative response of BPX61 photodiode at 1550 nm in temperature range from 10 K to 310 K.*

This work was supported by the German Science Foundation DFG under contract SFB TR7 (C9).

References

[1] C. Schwarz *et al.*, SSP **184**, 443 (2012).
[2] https://tds.ego-gw.it/ql/?c=7954
[3] J. Degallaix *et al.*, Optics Letters **38**, 2047-2049 (2013).
[4] J. Komma *et al.*, Annual Report 2014.

Measurement of the doping of silicon samples

Fabian Ritschel, Philip Pastrik and Ronny Nawrodt

The doping concentration of silicon wafers plays and important role to understand and model optical absorption mechanisms observed in silicon [1]. Silicon vendors often give a broad interval of parameters of the samples ordered. These intervals are not sufficient to test different theoretical models and their predictions. Therefore, the study of the doping concentration and the density of carriers at different temperatures is necessary.

There are different possibilities to measure the doping concentration of a silicon wafer, e.g. studying the resistivity of the sample or by means of a capacity-voltage-measurement (C-V-measurement).

The resistivity of a silicon sample can be measured by means of a 4-probe-technique. 4 metallic pads are applied to the sample and a current-voltage-measurement is done (see Fig. 1). As a contact material aluminium was used. A heat treatment at 450°C for 6 hours after deposition created an ohmic contact between the aluminium and the silicon sample. The potential distribution is given in Fig. 2 if the two outermost contacts are used to apply a current.

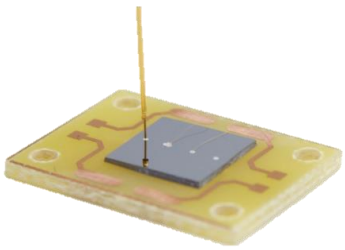

Fig. 1: *Photograph of a Si sample on a sample holder to study the resistivity in a 4-probe-geometry.*

The resistivity of the sample was studied at different temperatures. The results are given in Fig. 3. The resistivity drops from room temperature down to about 70 K and then increases again. Here the free carriers introduced by the doping process get frozen out to their ground states and thus the charge density is reduced. Below 50 K the sample had such a low resistance that no measurement was possible.

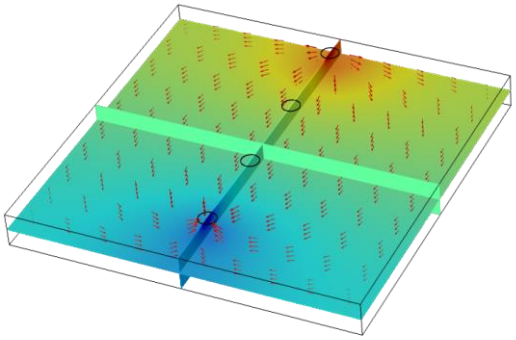

Fig. 2: *Visualization of the voltage potential caused by current flow (red arrows) through a Si sample simulated using Comsol.*

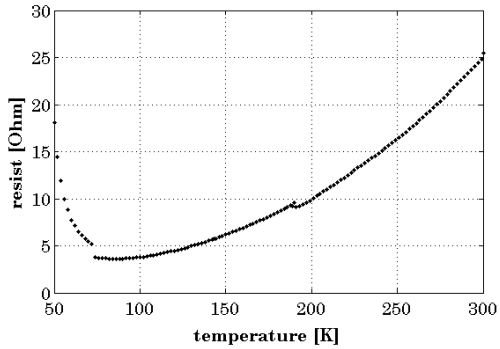

Fig. 3: *Temperature dependent resistivity of a silicon sample.*

The 4-probe-technique is measuring the integral resistivity of the sample over a larger area. In order to probe at a single position and in order to get information on the depth profile of the doping the C-V-

measurement can be used. In this method, the capacitance C of a Schottky contact at the surface of the semiconductor is measured depending on the applied bias voltage V_{ext}.

Therefore it is necessary to create a Schottky contact on top of the sample and an ohmic contact at its back to realize the measurement. While the ohmic contact has been created as described above, applying a 200 nm thick gold film created the Schottky contact. A photograph of the sample can be seen in Fig. 4.

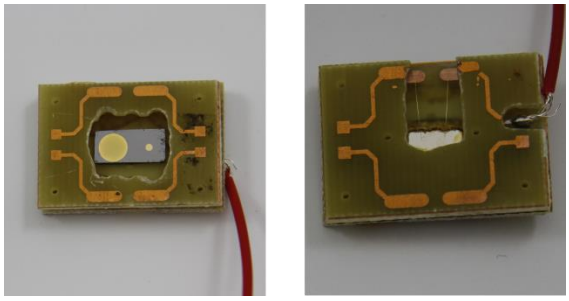

Fig. 4: *Top side gold contact (left) and bottom side aluminum layer (right).*

The electric contact on the backside has been realized by gold bonding. For the top side contact, a spring-loaded gold tip was attached to the gold spot.

The measured capacity of the Schottky contact in reverse bias depends on the bias voltage as follows [2]:

$$\frac{1}{C^2} = \frac{2\left(V_{bi} - V_{ext} - \frac{kT}{e}\right)}{eN_D\,\epsilon_S}$$

For a doped sample, the slope of the $1/C^2$ - curve returns the doping concentration. In case of homogeneous doping, it shows a linear relation [2].

A set of wafers with an assigned resistivity of 1-5 Ωcm has been tested. The results are represented in Fig. 5.

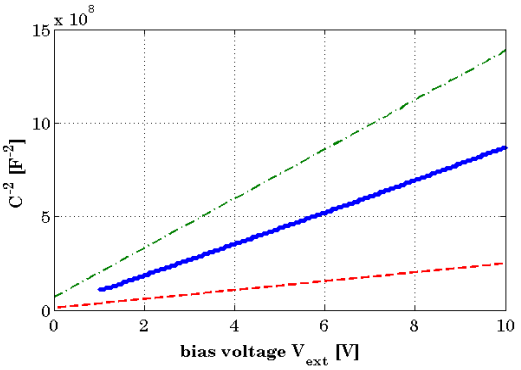

Fig. 5: *4 mm diameter gold contact on silicon. Dash-dotted line: 1 Ωcm; dashed line: 5 Ωcm. Crosses: measured values.*

The slope of the measured values represents to a resistivity of (3.1±0.2) Ωcm.

This work has been supported by the BMBF under contract 05A13SJ1.

References

[1] J. Komma *et al.*, Annual Report 2014.

[2] M. Grundmann, The Physics of Semiconductors, Springer, Berlin (2006).

Preparation and examination of F-doped Nd-1111 superconductors

Stefan Schmidt, Naoki Sumiya[1], Masashi Chihara[1], Takafumi Hatano[1], Fritz Kurth[2], Sebastian Döring, Frank Schmidl, Kazumasa Iida[2], Hiroshi Ikuta[1], and Paul Seidel

[1] *Department of Crystalline Materials Science, Nagoya University, Japan*
[2] *Institute for Metallic Materials, IFW Dresden, Germany*

Oxypnictide superconductors develop the highest transition temperature amongst all bulk iron-based superconductors with a top value of 56 K at $SmO_{1-x}F_xFeAs$ [1]. Unfortunately, their preparation is rather difficult. Here we present the preparation of superconducting $NdO_{1-x}F_xFeAs$ in a two-step process (see Fig.1) using molecular beam epitaxy (MBE).

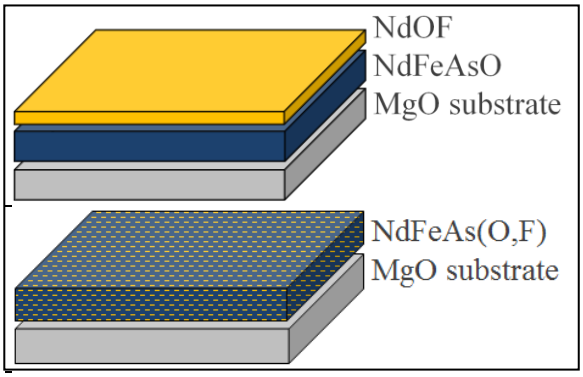

Fig. 1: Top: Sketch of the two-step deposition of undoped Nd-1111 and NdOF with the dopant F. Bottom: After flourine diffusion a NdFeAs(O,F) layer is formed.

All films were grown on MgO (100) substrates, both single crystalline and bicrystalline with a [001]-tilt. The bicrystal substrates were used to form and investigate grain boundary junctions.

Prior to the deposition the substrate is cleaned thermally at 800 °C within the lN_2-cooled MBE chamber with a rest pressure of 1.3 10^{-6} Pa. The Effusion cells are gradually heated up to 905 °C (NdF_3 cell), 1020 °C (Fe), 252 °C (As), and 735 °C (Ga). The Ga source is used as a fluoride getter to control the fluoride vs. neodymium ratio. The substrate is rotated slowly within an oxygen flux during the deposition (t_1 = 90 min). The resulting growth rate can be approximated to 100 nm per hour. The crystalline quality can be supervised by reflection high energy electron diffraction (RHEED), see Fig.2 during the whole deposition. After growing the undoped Nd-1111 layer the NdF_3 effusion cell shutter is left open while the other ones are closed. That way a second thin film is grown in oxygen flux resulting in the NdOF stoichiometry (t_2 = 30 min). Since the substrate and the Nd-1111 layer are still heated, a great amount of fluorine diffuses from the topmost layer into the base layer to substitute oxygen forming a crystal lattice of $NdO_{1-x}F_xFeAs$ with a T_c of about 45 K [2].

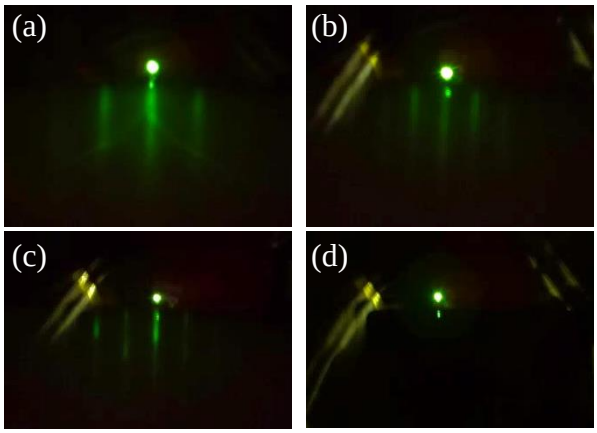

Fig. 2: RHEED patterns of the two-step MBE deposition: a) pure substrate, b) halfway into the Nd-1111 growth, c) shortly after the start of NdOF growth, d) after the whole deposition process.

Former works showed that the Ga flux used as F getter in the first deposition step is needed to get a superconducting thin film [2]. Without Ga flux the F content in the base layer would be too high to form crystalline Nd-1111. Skipping the second step has also been found to be crucial because otherwise the level of F doping

would not suffice to form a superconducting layer. Interestingly, the F content within the Nd-1111 is almost homogeneous after the final deposition step despite that the dopant is injected solely from the top, see cross-sectional Scanning Tunneling Electron Microscopy (STEM) pictures in ref. [3].

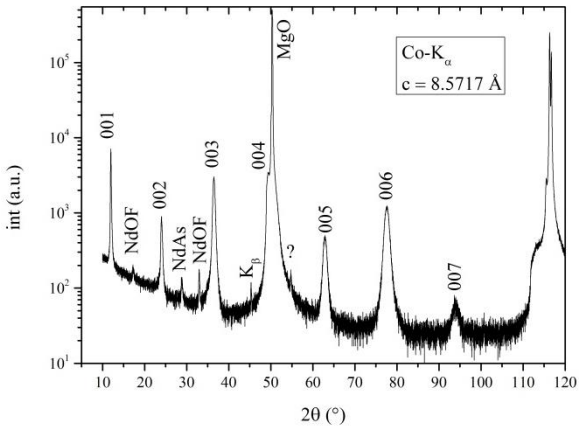

Fig. 3: Out-of-plane XRD profile of a complete Nd-1111/NdOF system. The peaks are indicated with (00*l*) reflections of Nd-1111 or foreign phases, respectively.

X-ray diffraction (XRD) measurements of the final system reveal foreign phases of NdAs and NdOF. The latter phase does not occur when leaving out the second deposition step as a comparison growth study suggested.

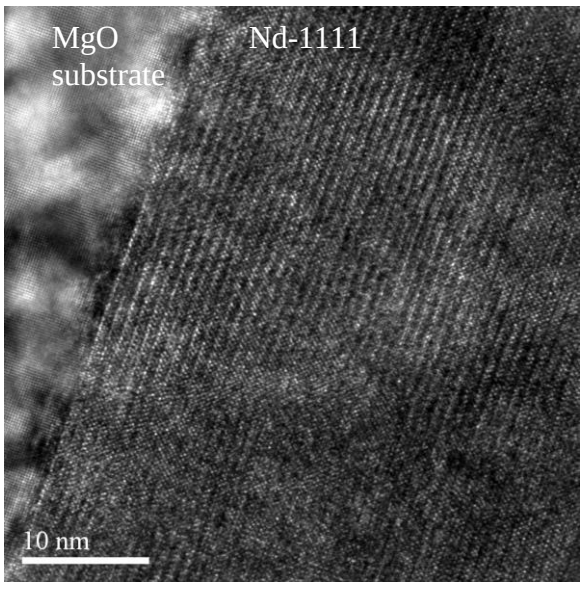

Fig. 4: STEM image of the MgO substrate (left) and the Nd-1111 layer (right). Nearly no disturbance region is formed at the interface.

Azimuthal ϕ-scans indicate an epitaxial growth of Nd-1111 on MgO [2], which is particularly important for future grain boundary junction investigations of samples deposited on MgO bicrystals. The interface between the substrate and the pnictide thin film is shown in Fig. 4.

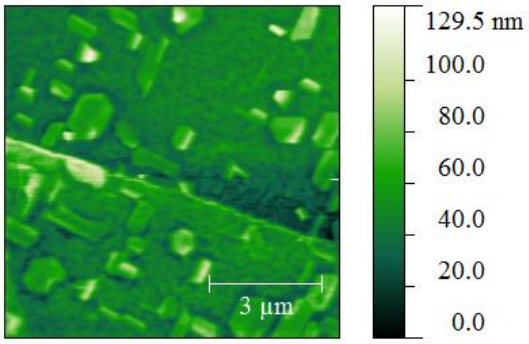

Fig. 5: AFM image of the Nd-1111/NdOF stack surface. The edge in the middle of the picture shows a step resulting from ion beam etching experiments.

Unfortunately, this kind of thin film deposition is not suitable for junction experiments along the c-axis of the superconductor because of its surface properties. Contrary to the sketch shown in Fig. 1 the NdOF deposition may form islands rather than complete layers. This growth mode is indicated by the spotty RHEED pattern (see Figs. 2c, 2d). A surface analysis by Atomic Force Microscopy (AFM) shows partly facetted and oriented islands, see Fig. 5. Future investigation will be needed to verify those islands to be NdOF. However, the deposition of pure Nd-1111 without NdOF layer delivered rather flat surfaces.

References

[1] Z.-A. Ren, W. Lu, J. Yang, W. Yi, X.-L. Shen, Z.-C. Li, G.-C. Che, X.-L. Dong, L.-L. Sun, F. Zhou, Z.-X. Zhao, *Chin. Phys. Lett. 25* (2008), 2215–2216

[2] T. Kawaguchi, H. Uemura, T Ohno, M. Tabuchi, T Ujihara, Y. Takeda, H. Ikuta, *Appl. Phys. Express 4* (2011), 083102

[3] K. Iida, F. Kurth, M. Chihara, N. Sumiya, V. Grinenko, A. Ichinose, I. Tsukada, J. Hänisch, V. Matias, T. Hatano, B. Holzapfel, H. Ikuta, *Appl. Phys. Lett. 105* (2014), 172602

Minimization of flux-trapping in SQUID magnetometers during cool-down

Thomas Schönau

M. Schmelz, V. Zakosarenko, R. Stolz and H.-G. Meyer
Leibniz-Institute of Photonic Technology, PO Box 100239, D-07702 Jena, Germany

We are currently developing a LTS SQUID-based setup that allows the absolute measurement of the magnetic field vector in magnetically unshielded environment [1]. To maintain the system's accuracy even after thermal cycling, it is important to avoid flux-trapping in the superconducting structures during cool-down to 4.2K, since this would affect the offset of the measured magnetic field. Several publications address the theory of flux-trapping in narrow superconducting strips and conclude that flux is only trapped if the magnetic field during cool-down exceeds a critical value $B_c = c\,\Phi_0/w^2$ [2]. Here, w is the width of the strip line and c is a constant between $\pi/4$ and 1.65, depending on the theory taken into account. Throughout this work, $c = 1.65$ is chosen since this value is best reasoned and experimentally verified. Based on this theory, we reduced the linewidth in our designs to be at maximum 5 µm near the SQUID and 6 µm in the bond pad, corresponding to a critical field of $B_c \approx 130\ \mu T$ and $90\ \mu T$. Both values are far beyond the Earth's magnetic field of about 50 µT. As we found, it is important even to limit the width of structures far away from the SQUID, since the magnetic moment of vortices in thin strips increases with the linewidth w [3]. Furthermore, closed superconducting loops are avoided throughout the whole chip design including the bond pads, which are shaped like a comb. To verify the expectations, we performed a measurement as following. A homogeneous background field is applied to the SQUID, which is immersed in liquid helium and shortly heated over its transition temperature (bias or feedback currents are disabled). After reaching equilibrium temperature, the background field is slowly ramped down

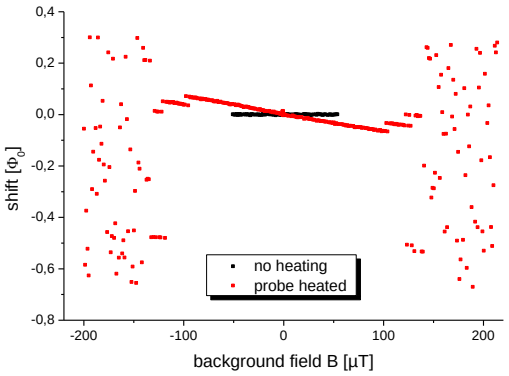

Fig. 1: *Shift of the SQUID's flux-voltage characteristic due to cool-down in a magnetic background field.*

and the flux-voltage characteristic of the SQUID is read out. For $B > 100\ \mu T$ steps occur as expected from theory. But a quasi-continuous linear dependency remains even for arbitrarily low magnetic field strengths. The origin of this effect is yet unknown but must be related to the superconducting phase transition, since it appears only if the probe is heated. Due to the described design improvements, the linear slope could be reduced about two orders of magnitude compared to previous chip designs.

The author likes to thank his supervisor Prof. Paul Seidel and his colleagues Dr. R. Stolz, Dr. V. Zakosarenko and Dr. M. Schmelz.

References

[1] Schönau T et al., 2013 *Supercond. Sci. Technol.* **26** 035013

[2] Kuit K et al., J 2008 *Phys. Rev. B* **77** 134504

[3] Pearl J 1966 *J. Appl. Phys.* **37** 4139

Geometrical Sputtering Effects in Ion Irradiated Au Nanoparticles

H. Holland-Moritz, C. Borschel and C. Ronning

Nanostructures can easily be fabricated by various techniques, which usually work at or near the thermal equilibrium. This might limit several desired properties of the material. Ion beam irradiation, a non-equilibrium method, is a widely used subsequent approach to tune the properties of materials and structures. One effect, when irradiating structures by ion beams, is sputtering. Sputtering is significantly enhanced in nanostructures compared to bulk, which can influence i.e. doping profiles and concentrations [1]. Simulations were performed with the Monte Carlo (MC) code *iradina* [2] in order to investigate the sputtering effects on various nanogeometries. Simulations of spherical, cylindrical and cubic structures were performed for different impact points from the center to the rim and the sputter yields were analyzed. The diameters of spherical and cylindrical structure as well as the edge length of the cube were 50 nm. As an ion species, Ar^+ ions with an energy of 100 keV were used.

Figure 1 shows the sputter yield plotted over the impact point on the structure. One can notice that the spherical structure (red) shows a larger yield than the cylindrical geometry (blue), which is larger compared to the cubic structure (green). The sputter yield has its smallest value for central impact and increases with the impact points moving towards the structure's rim. The slope is significantly smaller for the cubic structure. The maximum of the sputter yield is for peripheral impacts. To understand this behavior, one has to consider the intersection area of the

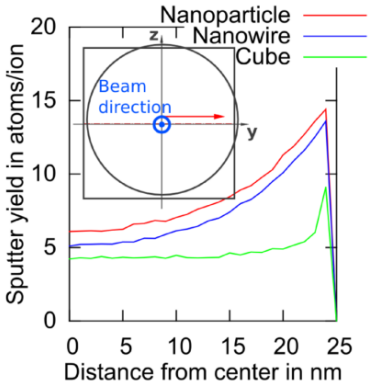

Fig. 1: *Sputter yield of nanogeometries over ion impact point. The inset shows the simulation principle. Taken from [4].*

damage cascade with the structure's surface. For central impacts, this intersection area is small, depending on the structure size and ion energy. For shifting the impact point towards the rim, the intersection area increases. Since this area depends on the structure's curvature [3], higher curvatures show a larger sputter yield. Since a cube shows no curvature at all, here the sputter yield is lower compared to sphere or cylinder. The sphere is curved in two dimensions compared to the cylinder with curvature only in one dimension, which explains the larger sphere sputter yield.

In this work, it was shown that the sputter yield strongly depends on the shape of the nanostructure. The reason is the increased intersection area of the damage cascade with curved surfaces.

References

[1] Johannes *et al., J. Phys. D:* **47**, 394003 (2014).
[2] Borschel *et al., Nucl Instrum. Meth. B* **269,** 2133 (2011)
[3] Nietiadi *et al., Appl. Phys. Lett.* **103**, 113108 (2013).
[4] A. Johannes *et al.*, Semincond. Sci. Tech., (2015) (accepted).

Thermo-refractive coefficient of sapphire from 10 to 410 Kelvin

Brian Seyfarth, Christian Schwarz, Julius Komma, Gerd Hofmann, Daniel Heinert and Ronny Nawrodt

Sapphire has low intrinsic mechanical [1] and optical [2] losses in the cryogenic temperature regime below 30 K and is thus suited as an optical material for interferometric gravitational wave detectors [3] like KAGRA or ET. Operating at cryogenic temperatures reduces thermal noise due to low temperatures as well as low mechanical losses.

Due to the cryogenic temperatures lots of material parameters change significantly. In transmissive optics the optical path is of importance which is affected by length changes as well as changes in the refractive index. Length changes are connected to temperature fluctuations by means of the well-known coefficient of thermal expansion α, whereas the change of refractive index is coupled to temperatures changes via the thermo-refractive index β. While the coefficient of thermal expansion is well studied, the thermos-refractive index is not well known for sapphire and silicon at cryogenic temperatures.

In order to measure the thermo-refractive index of sapphire an interferometric measuring method is used [4, 5] and adapted to a sapphire sample. A cylindrical sapphire sample forms a Fabry-Perot etalon using the Fresnel reflection R of the sapphire itself. A Helium-Neon-laser having a wavelength of λ= 632.8 nm and a fiber-Laser with λ = 1550 nm is used for optical studies. The thermally induced change of the optical path length consists of the change of the length nα and the refractive index β and induces a change in phase:

$$\frac{d\theta}{dT} = \frac{2\pi d}{\lambda}(n\alpha + \beta)$$

of the transmitted respectively reflected laser power. The reflected laser power is monitored by means of a photodiode and is given by:

$$I_r = \frac{I_0}{1 + (F\ \sin(\theta)^2)^{-1}}$$

with F being the Finesse $F = \frac{4R}{(1-R)^2}$. A typical measured signal is shown in Fig. 1.

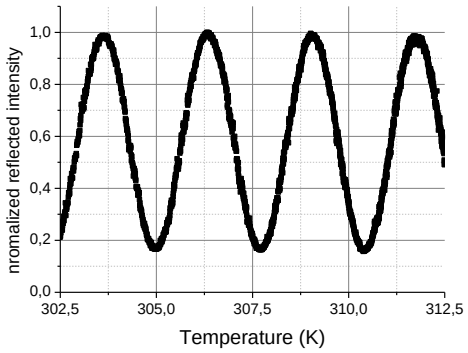

Fig. 1: *Measured signal over temperature in high temperature regime.*

In the high temperature regime the change of the refractive index was determined by measuring the period of the oscillations with temperature. The experimental results for high temperatures are shown in Fig. 2.

Below 80 K (632.8 nm) respectively 100 K (1550 nm), the change of the phase per temperature interval was too small for direct measurement of the period length, so it was necessary to fit the data to the signal to determine the thermo-refractive coefficient. An example for the fit of measured data is shown in Fig. 3.

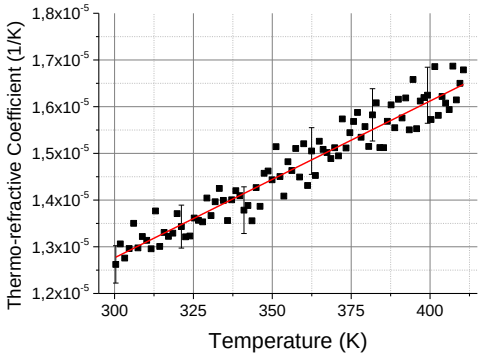

Fig. 2: *Thermo-refractive coefficient of sapphire for high temperature regime, measured at a 5 mm thick sapphire sample using a 632.8 nm Laser.*

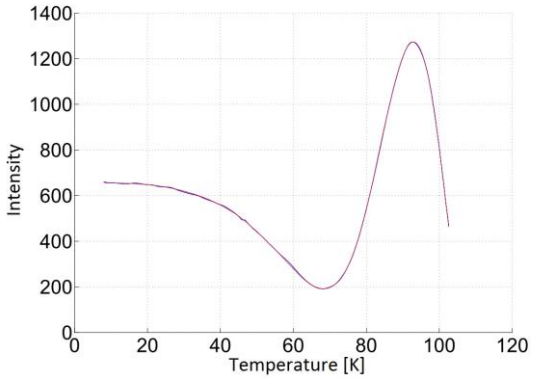

Fig. 3: *Measured signal (red) and fit (blue) over temperature in cryogenic temperature regime.*

With this experimental setup and analysis, it was possible to measure a minimal change of the refractive index of 4×10^{-9} 1/K at 8 K. The obtained values are summarized in Fig. 4. The measured values of $(7 \pm 3) \times 10^{-8}$ 1/K (632.8 nm) respectively $(1.6 \pm 0.8) \times 10^{-7}$ 1/K (1550 nm) at 40 K and $(1.27 \pm 0.04) \times 10^{-5}$ K^{-1} (632.8 nm) respectively $(1.12 \pm 0.14) \times 10^{-7}$ (1550 nm) at 300 K are in good agreement with values estimated by other groups [6].

Based on these experimental values it is now possible to determine thermo-refractive as well as thermos-optic noise in components for future GW detectors. Furthermore, the thermo-refractive coefficient is crucial to estimate thermal lensing effects.

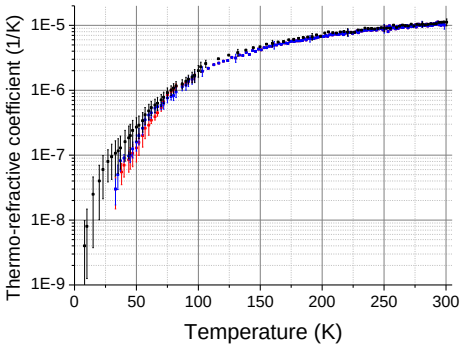

Fig. 4: *Thermo-refractive coefficient of sapphire for low temperature regime, measured at a 13 mm thick sapphire sample, using a 632.8 nm Laser (red and blue in figure) and 1550 nm (black).*

This work was supported by the DFG under contract SFB Transregio 7.

References

[1] V. B. Braginsky *et al.:* Systems with Small Dissipation, The University of Chicago Press, (1985).
[2] D. Blair *et al.*, Opt. Mat. **8**, 233-236 (1997).
[3] T, Tomaru *et al.*, Phys. Lett. **283**, 81-84 (2001).
[4] B. Seyfarth, Messung des thermo-optischen Koeffizienten von Saphir von 10 bis 410 Kelvin, Bachelorarbeit, (2014).
[5] J. Komma *et al.*, Appl. Phys. Lett. **101**, 041905 (2012).
[6] T. Tomaru *et al.*, Class, Quant.Grav. **19**, 2045 (2002).

Peculiarities of phase dynamics of two parallel stacks of coupled Josephson junctions

Yu. M. Shukrinov [a,b], I. R. Rahmonov [a,c], A. Plecenik [d], P. Seidel, E. Il'ichev [e,f] and W. Nawrocki [g]

[a]*BLTP, Joint Institute for Nuclear Research, Dubna, Moscow Region, 141980, Russia*
[b]*Dubna International University for Nature, Society and Man, Dubna, 141980, Russia*
[c]*Umarov Physical Technical Institute, TAS, Dushanbe, 734063 Tajikistan*
[d]*Department of Experimental Physics, Comenius University, Bratislava, Slovakia*
[e]*Leibniz Institute of Photonic Technology, PO Box 100239, D-07702 Jena, Germany*
[f]*Novosibirsk State Technical University, 20 Karl Marx Avenue, 630092 Novosibirsk, Russia*
[g]*Poznan University of Technology, Poznan, Poland*

A strongly anisotropic high-T_c superconductor (HTSC) forms a natural stack of coupled Josephson junctions (JJs) and shows the intrinsic Josephson effect [1]. For some applications, particularly, for high power terahertz emission [2,3] it is interesting to consider the circuits which consist of two stacks of coupled JJs connected in parallel shown in Fig.1.

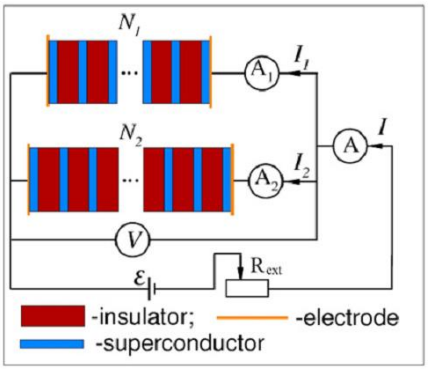

Fig. 1: *Scheme of parallel connections of two stacks with N_1 and N_2 JJs. Here voltmeter V shows the voltage in the stacks, amperemeters A_1 and A_2 shows the current value through the first and second JJs stack, respectively [4].*

In the simplest case $N_1 = N_2 = 1$, this is the well-known superconducting quantum interference device (DC-SQUID). The main advantage of these devices based on HTSC is a possibility to operate at liquid nitrogen temperature (77K) in comparison with the traditional SQUIDs operating at liquid helium temperature (4.2K). However, a direct use of these stacks faces a problem of intensive branching of their current voltage characteristics leading to the complexity of an analysis of the data and preventing their application for magnetometry. So, a great challenge is to develop the principles and methods to exclude such switching of JJs and remove the main barrier on the way of creation of reliable SQUIDs based on this type of stacks.

This report based on the results of simulation of phase dynamics of two parallel stacks of JJs, which is published in Ref [4]. To clarify the physics of switching between different states, we study the system with a small number of JJs in the stacks. In comparison to the well-known capacitively coupled Josephson junction (CCJJ) model [5] we use the model with a diffusion current (CCJJ+DC model) [6]. We have demonstrated that taking into account the diffusion current makes it possible to escape the branching of IV-characteristics with an equal number of JJs in the stacks. We clearly show the switching mechanism by analysis of diffusion current and IV-characteristics of all JJs in both stacks. The comparison of the results for CCJJ and CCJJ+DC models

stresses the importance of diffusion current in the switching processes.

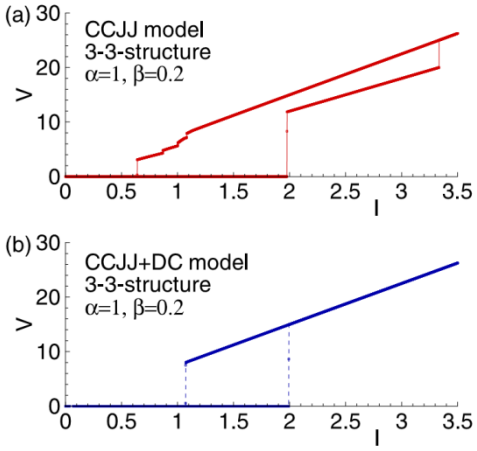

Fig. 2: *(a) One loop IV-characteristics of the 3–3- structure in CCJJ model. (b) The same for CCJJ+DC model [4].*

It was demonstrated in [7] that the diffusion current plays an important role in suppressing branching in the IV-characteristics of the single stack of coupled JJs. We consider that in our case of two parallel stacks the absence of branching in the IV-characteristics has the same origin: it is an effect of the diffusion current. To test this idea we simulate the IV-characteristics of parallel stacks in the framework of the CCJJ model that does not include a diffusion current and compare with the results of the CCJJ+DC model with the same parameters of the system. The results of simulations for the 3–3-structure are presented in Fig.2. To make features more pronounced we simulated the IV-characteristics at α =1, where α is coupling parameter.

We see the branching of the IV-characteristic in the CCJJ model around the critical current and in the hysteretic region. However, the IV-characteristic of the CCJJ+DC model with the diffusion current demonstrates a collective behavior of JJs, i.e., without transitions to any rotating and oscillating states.

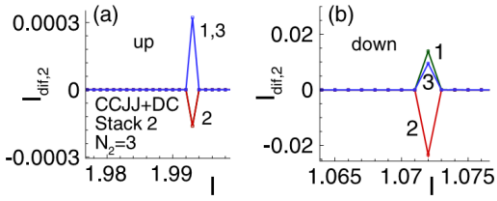

Fig. 3: *(a) Diffusion current around Ic of the 3–3-structure in the CCJJ+DC model. (b) The same in the hysteretic region [4].*

The question then arises what suppresses such transition in this model. The answer can be found in figure 3. The diffusion current changes its direction along the stack making the intermediate states unstable and forcing the system transit to the final state.[7] The behavior of the diffusion current around the critical value I_c is shown in Fig.3(a). We see that at the transition point the first and third JJs have positive I_{dif} but the second one has negative value, i.e. opposite direction. The same features are observed in the hysteretic region presented in Fig.3(b). The diffusion current in the first stack reflects this behavior.

References

[1] R. Kleiner, F. Steinmeyer, G. Kunkel and P. Müller, Phys. Rev. Lett. **68,** 2394 (1992).

[2] T.M. Benseman, K.E. Gray, A.E. Koshelev, W.-K. Kwok, U. Welp, H. Minami, K.Kadowaki and T. Yamamoto Appl.Phys.Lett. **103,** 022602 (2013).

[3] Gross B et al. Phys. Rev. B **88,** 014524 (2013).

[4] Yu. M. Shukrinov, I.R. Rahmonov, A. Plecenik, P. Seidel, E. Il'ichev and W. Nawrocki Supercond. Sci. Technol. **27,** 124007 (2014).

[5] T. Koyama and M. Tachiki, Phys. Rev. B **54,** 16183 (1996).

[6] Yu. M. Shukrinov, F. Mahfouzi and P. Seidel Physica C **449,** 62 (2006).

[7] Yu. M. Shukrinov and I. R. Rahmonov, JETP **115,** 289 (2012).

Optimization of the measurement of absorption in Silicon

Malte Siems, Julius Komma, Gerd Hofmann, Christian Schwarz, Daniel Heinert and Ronny Nawrodt

In current gravitational wave detectors like LIGO [1] and GEO600 [2] the material used for the test masses is fused silica. In order to improve the sensitivity in coming generations of detectors, operation at low temperatures is planned. It has been shown, that the noise will not decrease with temperature in fused silica as the mechanical losses rise considerably [3].

Crystalline silicon is a good option as it has the desired characteristics at low temperatures and is available in quantities large enough due to the demand from the semiconductor industry.

An important aspect is the heating due to the absorption of laser radiation. Measuring the initial and transmitted power does not provide the necessary sensitivity to measure the optical absorption of silicon. That is why a calorimetric setup is used.

In order to allow a swift change of samples, a small continuous flow cryostat from CRYOVAC is used. The sample is irradiated with a 5 W cw fiber laser from NKT Photonics. The resulting rise in temperature is measured and the absorption can be calculated.

One source for deviation in this setup is scattered light hitting the temperature sensor. This problem is more apparent when using a fused silica sample, as the thermal conductivity is much lower than in silicon [4] as can be seen in Fig. 1.The heat which is caused by the laser beam hitting the center of the disk has to reach the sensor which is located at the mantle of the sample. The three pictures of a calculation seen in Fig. 2 show the heat distribution in

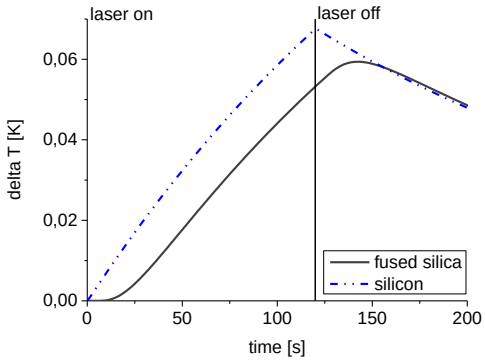

Fig. 1: *Heating curve of fused silica and silicon. The heat reaches the sensor much faster in silicon resulting in an almost instantaneous temperature rise.*

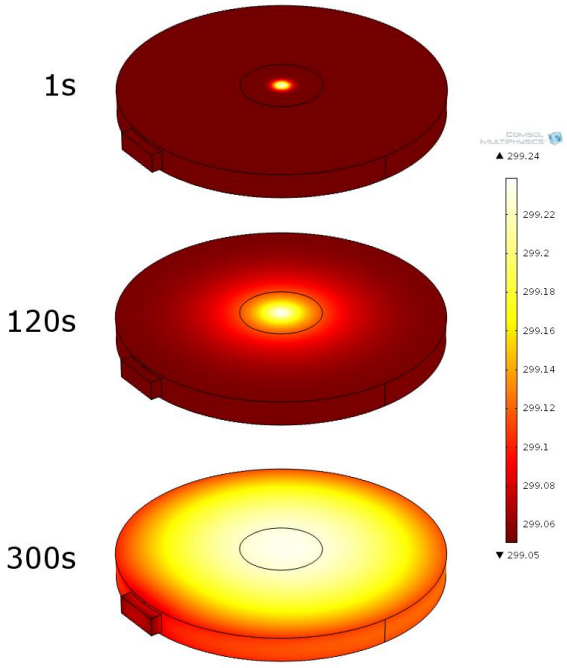

Fig. 2: *Simulation of the heat distribution in a fused silica sample (1" by 2 mm) irradiated by a 2 W laser beam and 600 ppm absorption.*

a 1" by 2 mm fused silica disk which is irradiated by a 2 W laser for 120 s. In Fig. 3 the rise in temperature of a fused silica sample when irradiated with a laser is compared to when electrically heated.

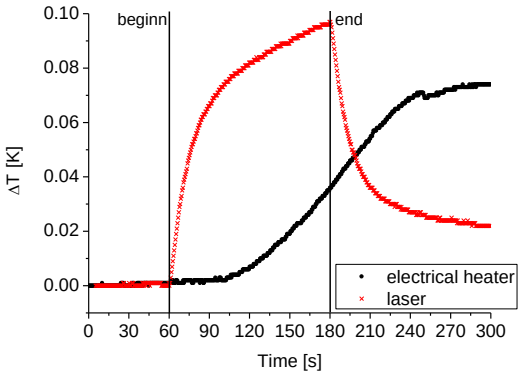

Fig. 3: *Heating curves of a fused silica sample irradiated with a laser or heated electrically.*

The heater is located at the mantle with the same distance to the sensor as the laser beam. One can see that the increase in temperature is almost instantaneous with the laser while the heat from the electric heater takes a longer time to reach the sensor. This means that some light is directly hitting and so heating the sensor.

In order to reduce the amount of scattered light sets of apertures are added. To show their effect the profile of the beam is determined. An optical fiber with a diameter of 500 µm is moved across the beam and the power transmitted through the fiber is recorded. The resulting graph is shown in Fig. 4. The red line represents a perfect Gaussian power distribution. Especially towards the sides the measured power deviates from this ideal beam shape. With the added apertures the power 4 mm from the center could be reduced by two orders of magnitude. With this and other optimizations it was possible to measure absorption in the order of tens of ppm.

In a sample of silicon from MicroChemicals with a specific resistance of 1-10 Ωcm and 500 µm thickness we determined the total absorption to be 880 ppm. Using a deflection method the group around A. Bell in Glasgow measured

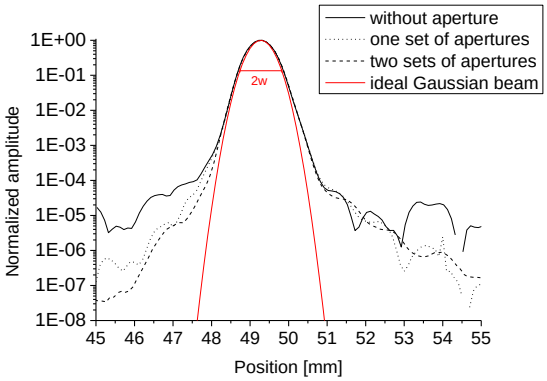

Fig. 4: *Beam profile of the laser measured used an optical fiber.*

600 ppm absorption at a sample from the same silicon crystal.

Using the dependence of the absorption on the conductivity described by J. Degallaix [5] a value between 210 ppm and 2100 ppm is to be expected for the 1-10 Ωcm range.

Over all, our method offers the possibility to measure low absorption of silicon at 1550 nm. On top of that it will be possible to do so over a wide range of temperatures reaching from 4 K to 300 K.

This work was supported by the DFG under contract SFB Transregio 7.

References

[1] A. Abramovici *et al.*, Science. **17**, 325-333 (1992).
[2] H. Grote for the LIGO Scientific Collaboration, Class. Quant. Grav. **27**, 084003 (2010).
[3] C. Schwarz *et al.*, Proceedings of ICEC22-ICMC2008. The Korea Institute of Applied Superconductivity and Cryogenics, (2009).
[4] J. Franc *et al.*, ET document ET 09021, (2009).
[5] J. Degallaix *et al.*, *Optics Letters.* **38**, 2047-2049 (2013).

Quality management of measuring equipment – First step: Time and frequency

Volker Tympel

The description of observational error in daily university physics is mostly a lock into the data sheet of the measurement device and an error calculation based on first derivations. So in reality we can handle small random errors and we can only hope that the original manufacture calibration is still acceptable. For the manufacturer is it imperative to accept and follow the rules of the ISO-9001 quality management system. The point 7.6 – Control of monitoring and measuring equipment – sais: "The organization shall determine the monitoring and measurement to be undertaken and the monitoring and measuring equipment needed to provide evidence of conformity of product to determined requirements."[1] That means a quality management system of measuring equipment has to include a clear and continuous path to a national metrology institute, mostly via accredited laboratories.

Because the ISO 9001 standard was written by engineers and quality professionals from large industries a reinterpretation for university environment was started at the end of the 90s [2]. At present the interpretation has been generally accepted. Universities of applied science started early with an ISO-9001- accrediting (FH Hannover in 2004). Technical universities like TU Chemnitz (2007) followed later. Also old and venerable universities like Tubingen and Jena have ISO-9001- certified medical institutions and clinics.

At the end it is a question of money to cover the cost of a certified quality management system which includes the cost for a periodical certified calibration of important measurement equipment. Without a doubt measurement devices with valid stickers from accredited calibration service will be the standard in physical instituted of universities someday. But it is also possible to reduce the real absolute observational error and to improve the accuracy und trueness of our measurement results in these days.

For example frequency measurement is important for the correct determination of Shapiro steps of Josephson junction. Therefore time and frequency measurement are basics of a standard volt. Time and frequency are relative easy to handle.

For instance, having a time pulse of one second, an electronic counter and a tunable frequency generator, we can tune the generator to a standard frequency like 10 MHz. A simple system can consist of a HAMEG HM8021-3 1,6 GHz counter, a HP 33120A 15 MHz function generator and a GPS receiver module like ET-102 with one pulse per second output (1PPS) [Fig. 1]. Thereby it is possible to use the GPS time basis of over 100 atomic clocks. A typical time jitter of the GPS receiver is in the order of 50 ns [3]. Using the ten second integration time mode of the HM8021-3 counter we can achieve a 10 MHz reference frequency with accuracy in the order of 10^{-8} – mostly limited by resolution of the function generator and its temperature stability. Now we can test the GPS based reference system and check the HM8021-3 frequency counters of the so-called Elektronik-Praktikum of the Institute of Solid

State Physics. The measurement of the 1PPS Time Mark shows absolute observational errors up to $2 \cdot 10^{-6}$ for systems without any calibration in the last 15 years. With the 10 MHz frequency of our tuned HP 33120A on the input of the HM8021-3 counter and a defined button combination it is possible to start an automatic calibration procedure to correct the internal oscillator of the counter. One day after that calibration we have an absolute observational error less than 10^{-7} [Fig. 2]. The manual recommends one calibration every 6 months.

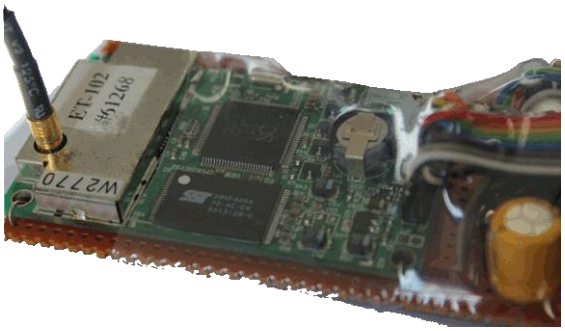

Fig. 1: *ET-102 GPS Receiver engine board with 1PPS Time Mark output.*

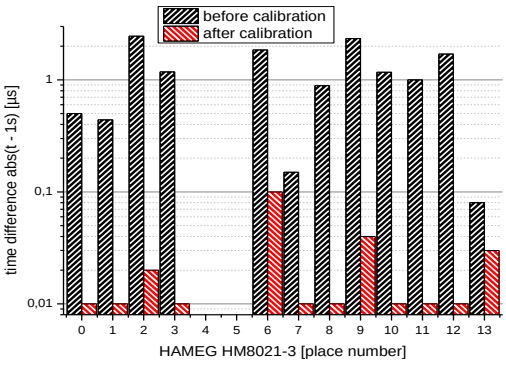

Fig. 2: *Measurement of the 1PPS Time Mark before and after calibration (places 0–9 1 day, places 10–13 3 months) of 12 HAMEG HM8021-3 systems.*

The HP 83751B is a frequency generator for the range from 2 to 20 GHz and optimal to investigate Shapiro steps. Unfortunately the uncalibrated generator has an absolute observational error of $4 \cdot 10^{-6}$. But it is possible to enhance the performance via an external 10 MHz reference frequency.

State of the art is a frequency standard with a frequency-locked loop (FLL) using the atomic resonance property of Rubidium (^{87}Rb) to control the frequency of a quartz crystal [Fig. 3]. Rubidium frequency standards are commercially available, inexpensive and having an accuracy of 10^{-9} is not a problem. Using the so-called C-field (magnetic field) adjustment and an even better reference source for the calibration 10^{-10} or better is also possible [4].

Fig. 3: *Open Datum LPRO 10 MHz Rubidium oscillator for time and frequency reference with the so-called Rubidium physics package.*

References

[1] ISO 9001:2008(E), Quality management systems - Requirements: Fourth edition 2008-11-15.

[2] S. Karapetrovic *et al.*, ISO 9001 Quality System: An Interpretation for the University, *Int. J. Engng Ed.* Vol. 14, 105-118, No. 2, (1998).

[3] P.J. Mumford, Relative timing characteristics of the one pulse per second (1PPS) output pulse of three GPS receivers, presented at SatNav 2003, download 2014-12-20: *www.gmat.unsw.edu.au/snap/publications/mumford_2003a.pdf*.

[4] Datum, LPRO Rubidium Oscillator for Time & Frequency Reference - User's guide and integration guidelines, (2000).

Processing of Ba-122 single crystals for fabrication of Josephson junctions

Noor Hasan, Sebastian Döring, Stefan Schmidt, Volker Tympel, Frank Schmidl, Paul Seidel, Thomas Wolf [1]

[1] *Institute of Solid State Physics, Karlsruhe Institute of Technology, D-76021 Karlsruhe*

The new material class of pnictide superconductors has very promising properties regarding its applicability in superconducting electronics. Josephson junctions are an excellent tool to investigate these properties systematically. To fabricate junctions on single crystals of $Ba(Fe_{1-x}Co_x)_2As_2$ with x=0.065, which were produced with a self-flux method [1,2], we have to investigate several issues like the surface structure and the etching rate of the crystal. We used both undoped and Co-doped single crystals of $BaFe_2As_2$.

Thin film technologies require high quality surfaces; therefore we use chemical- mechanical polishing (CMP) in order to reach a RMS roughness of less than 5nm. The scanning electron microscopy (SEM) image in Fig.1a obtained for a crystal as grown shows obvious irregularities. These make it necessary to apply a polishing method for these materials. The surface after polishing can be seen in the Fig.1b, where the flattened areas of the surface are indicated by white frames. A RMS roughness of 3.3nm was measured by AFM. Further details of the polishing procedure can be found in Ref. [3].

"Electron backscatter diffraction (EBSD) is a powerful tool in the crystallographic characterization of materials. In EBSD, the local resolution of the focused electron beam in a scanning electron microscope is utilized to observe Kikuchi patterns of electrons backscattered from spatially confined sample regions." as it is stated in Ref. [4]. The SEM micrograph and its EBSD analysis for five different locations of a doped crystal are illustrated in Fig.2. It shows that the crystal orientations which can be indicated by three Euler Angles (21°, 178°, 12°) with a deviation of less than 2°, illustrated in the white frame on the left. The crystallographic axes of doped crystals refer to a tetragonal crystal system, like in undoped ones. A SEM image with EBSD analysis of an undoped crystal is reported by Ref. [3].

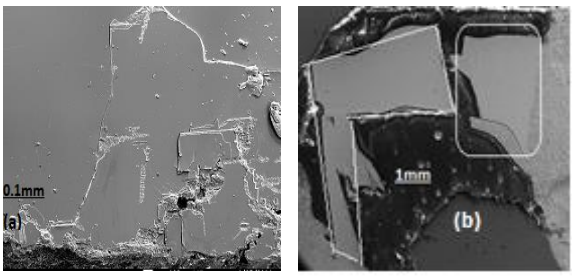

Fig.1: *SEM image obtained from doped crystal. (a) Unprocessed surface (b) polished surface with flattened areas within the white frames.*

The respective Kikuchi bands for both doped and undoped samples are shown in Fig.3.The Kikuchi bands, which are shown for a polished sample in Fig.3a; show a high quality pattern in the investigated region. The crystal lattice in the investigated region should ideally be strain-free and relatively clean from contamination or thick oxide layers so that the diffraction pattern will occur. If these conditions are not met, the resulting EBSD patterns will have a poor quality or they will be diffuse as can be seen in

Fig.3b (2, 4, and 5) in the case of doped crystals. They show a locally lower image quality of Kikuchi-patterns, which may be caused by degradation in the atmosphere or an inhomogeneous polishing process.

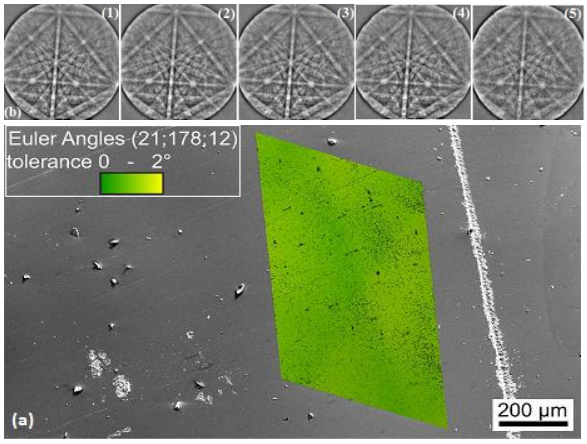

Fig.2: *(a) SEM image for the unprocessed surface of a doped crystal. (b): Kikuchi patterns obtained from its surface at five different locations.*

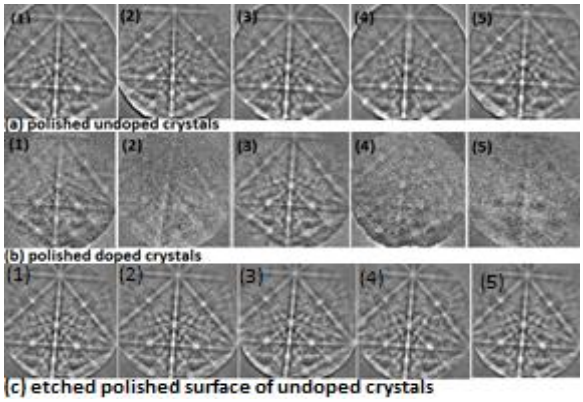

Fig. 3: *Kikuchi patterns obtained on five different positions (1 to 5) on differently treated (a,b,c) crystal surfaces.*

In contrast, Fig.3b (1,3) displays that the crystal structure is not significantly distorted everywhere. That may be the case because its surface is comparatively free from any of the disturbances mentioned above. To remove such degradation on the surface an additional process of ion beam etching can be introduced. In Ref. [5] the authors show that ion etching has advantages regarding surface properties of several materials. Etching polished samples can be an effective tool to achieve better surface properties. Fig.3c shows that a subsequent etching step may enhance the surface quality and thus may enhance the EBSD-patterns quality compared to the ones in Fig.3a. In addition to the cleaning, ion beam etching is one of the main tools for sample preparation in thin film technology. The samples are treated by using an Ar ion beam (beam voltage=500V, acceleration voltage=100V, current density=0.9mA/cm^2) for both the cleaning and the etching process. On a CMP-polished surface of the single crystal the etching rate was determined to be about 25nm/min using the parameters mentioned above. Since dealing with the doped crystals is identical to the undoped ones, we may apply the results we obtained from EBSD-patterns of an undoped crystal surface to doped crystals. That lets us assume that the surface quality of the doped samples most probably will be improved after a subsequent etching step. If this assumption proves to be correct we may be able to use doped single crystals for junction fabrication in the near future.

We thank the EC (project IRON-SEA), the DFG (SPP 1458), and the DAAD for financial support.

References

[1] F. Hardy *et. al*., Phys. Rev. B **81**, 060501(2010).
[2] F. Hardy *et. al*., EPL **91**, 47008 (2010).
[3] D. Reifert *et. al*., Supercond. Sci. Technol. **27** 085003 (2014).
[4] A. Winkelmann *et. al.*, Ultramicroscopy **110** 190–194 (2010).
[5] Z. Radi, *et. al*., IEEE- International Conference on Nanotechnology, 1-3 (2014).

Ultra-low-temperature chemistry inside superfluid helium nanodroplets

Serge A. Krasnokutski, Friedrich Huisken, and Cornelia Jäger

Helium nanodroplets are produced by supersonic expansions of gaseous He into a vacuum chamber. The superfluid helium drops, having a temperature of 0.37 K, can pick up atoms and molecules that can form bigger complexes in the He droplets. Thus, they provide unique experimental opportunities to study chemical reactions and properties of isolated radicals at this low temperature. Reactions inside superfluid helium droplets resemble the reactions occurring on the surface of cold dust grains in the interstellar medium (ISM). In order to understand the chemistry occurring in the ISM, we studied the reactivity of Fe and C atoms inside the droplets.

The reactivity of Fe atoms was studied by mass spectrometry and resonant two-photon ionization (R2PI) technique [1]. R2PI spectroscopy was used to monitor the number of Fe atoms as a function of the pressure of the second reactant (Fig. 1). The studies demonstrated the complete reaction between the reactants in the time scale of the experiment (~500 μs). Mass spectrometry was used to monitor the products of the chemical reaction. The comparison of experimental results with the findings of quantum chemical calculations (b3lyp/6-311g+[d,p]) allowed to predict the molecular structure (Fig. 1) and the bonding energies of the products. It was found that iron atoms prefer the formation of weakly bound adducts and exclude the formation of structures, where the iron atom is inserted into an existing molecular bond of the reaction partner. It follows that these reactions should not proceed in the gas phase at low temperature because there is no possibility for the formed adducts to release the binding energy.

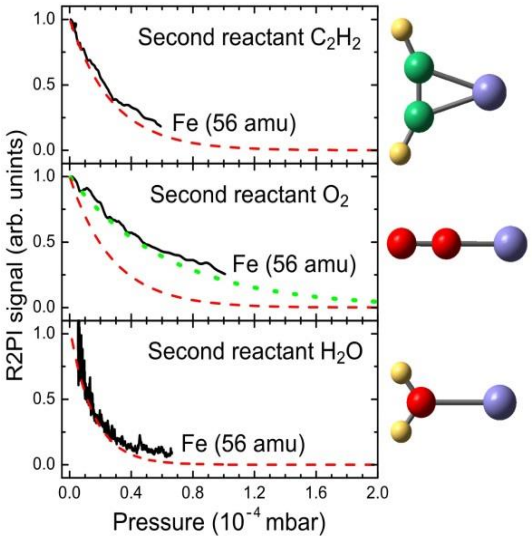

Fig. 1: *R2PI signals for Fe atoms recorded at $\lambda_{exc.}$ = 299 nm as a function of the pressure of the second reactant in the pick-up cell. The red lines represent the number of helium droplets, which do not contain the second reactant. The green curve in the middle frame also gives the number of helium droplets without a second reactant, but assuming a reduced pick-up cross-section for O_2 (2.3 times smaller than the geometrical cross-section of the droplet).*

The results suggest only a weak bonding of iron atoms to the surface of carbonaceous or icy interstellar dust grains. Therefore, we can expect that physisorbed iron atoms can be easily desorbed from the surface of such dust grains upon UV irradiation or other excitation. For the Fe + O_2 reaction, the stabilization of the linear intermediate FeOO was observed. Finally, it was found that the reaction products could easily be dissociated upon excitation. This was demonstrated by the efficient fragmentation of the FeC_2H_2 complex and the complete dissociation of the FeO_2 complex after the charge transfer from He^+.

To study the reactivity of carbon atoms we developed a simple and clean source of low-energy atomic carbon [2]. The source exclusively emits carbon atoms with a very small amount of impurities. The generated carbon atoms have low translation energy and are therefore well suited for the incorporation into nanosized helium droplets using pick-up techniques.

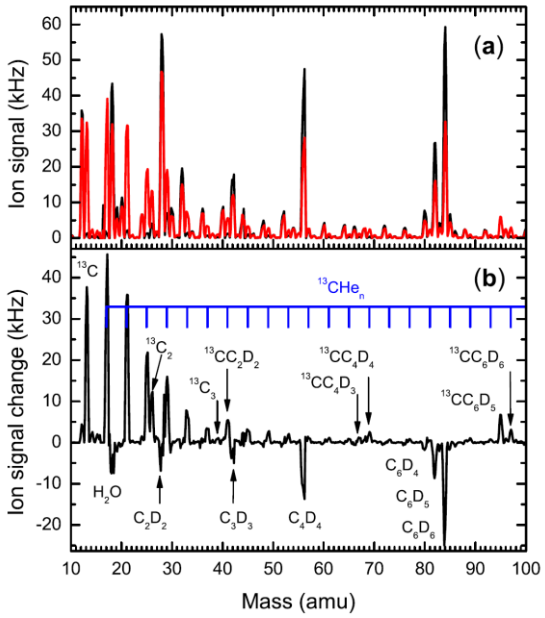

Fig. 2: *(a) Mass spectra of He droplets doped with carbon atoms followed by benzene (red) and with benzene molecules alone (black). The difference spectrum (red–black) is given in (b).*

We studied the reaction of carbon atoms with benzene by mass spectrometry and calorimetric techniques [3]. Figure 2 shows the mass spectra obtained when the He droplets were doped by C_6D_6 (black curve) and by C_6D_6 and ^{13}C (red curve). The panel (b) presents the differential mass spectrum that was obtained by subtracting the black spectrum from the red one.

This differential mass spectrum shows the effect of ^{13}C incorporation into helium droplets doped by C_6D_6. Negative peaks are due to reactants which were consumed in the reaction while positive peaks belong to species associated with the carbon incorporation, i.e., the incorporated carbon atoms, newly formed complexes between carbon ions and He atoms and, finally, the products of the chemical reaction between C_6D_6 and ^{13}C. The calorimetry studies rely on the measurement of the sizes of He droplets before and after the reaction. As the evaporation of each He atom takes about 5 cm^{-1} of energy, it becomes possible to measure the energy released in the reactions between single pair of reactants.

The reaction between the two species was found to have no barrier in the entrance channel. The calorimetric measurement revealed a considerable amount of energy being released in the reaction. Both mass spectrometric and calorimetric studies demonstrated the stabilization of the intermediate product (C_7D_6) of the comparable reaction in the gas phase. Based on the comparison of reaction energies obtained in the present study and in previous quantum chemical computations, the formation of a seven-membered carbon ring was demonstrated. Such barrierless reaction between benzene molecules and atomic carbon, which belongs to the four most abundant species in the ISM, is of great interest for the discussion of the stability of PAHs in the ISM. Therefore, the present studies will be extended to reactions of atomic carbon with small and larger PAHs. Such studies are expected to yield valuable information enabling us to predict the structure and size of those PAH molecules, which may reach a pronounced abundance in the ISM, as a result of their chemical stability.

References

[1] S. A. Krasnokutski and F. Huisken, J. Phys. Chem. A **118**, 2612 (2014).

[2] S. A. Krasnokutski and F. Huisken, Appl. Phys. Lett. **105**, 113506 (2014).

[3] S. A. Krasnokutski and F. Huisken, J. Chem. Phys. **141**, 214306 (2014).

Formation of silicate grains at cryogenic temperatures

Gaël Rouillé, Serge A. Krasnokutski, Cornelia Jäger, and Thomas Henning

Melinda Krebsz, Hungarian Academy of Sciences, Budapest

Silicate grains represent the main constituent of cosmic dust. In the interstellar medium (ISM), the destruction rate of the grains in diverse processes is estimated to be faster than their production rate by stars [1]. However, in the ISM, their mass amount is observed to be steady. Consequently, it has been proposed that silicate grains may grow in the ISM by means of chemical reactions between adsorbed gas-phase substances. The growth mechanism and the associated chemical reactions would take place in spite of the low temperatures of 10–100 K that prevail in the various interstellar regions. Our group has started an experimental study of the formation and growth of silicate dust grains at cryogenic temperatures [2].

In the first step of our study, gas-phase precursors of silicates were produced under vacuum by the laser vaporization of solid targets. For our first experiments, two amorphous materials were used as the targets, Mg_2SiO_4 and $Mg_{0.4}Fe_{0.6}SiO_3$. The gas-phase species produced by this means were deposited along with Ne atoms in excess onto a KBr substrate kept at ~6 K. They were thus isolated in an inert medium at a cryogenic temperature, allowing us to analyze them using both UV/vis absorption spectroscopy and Fourier transform IR (FTIR) spectroscopy. The atomic species Mg and Fe were observed at UV wavelengths. Atomic Si, however, was not found. Three molecules were identified by FTIR spectroscopy: SiO, O_3, and O_4^+. Others were tentatively reported: SiO_2, SiO_3, FeO, and OFeO.

The second step of each experiment consisted in annealing and evaporating the Ne matrix by elevating its temperature progressively from 6 to 13 K. After the evaporation of the Ne atoms, the substrate being brought back to ~6 K, FTIR spectra were measured again. A weak, broad absorption band could be observed at ~10 μm in the experiment with the Mg_2SiO_4 target (Fig. 1). Such a feature was not seen at this stage when using the $Mg_{0.4}Fe_{0.6}SiO_3$ target. The conjunction of a low signal-to-noise ratio with the presence of H_2O ice formed during the annealing and evaporation of the Ne matrix motivated measurements at room temperature. In the absence of H_2O ice, a broad absorption band appeared at ~10 μm (1000 cm^{-1}) in both experiments. Such a band is a typical feature in the IR spectra of solid silicates.

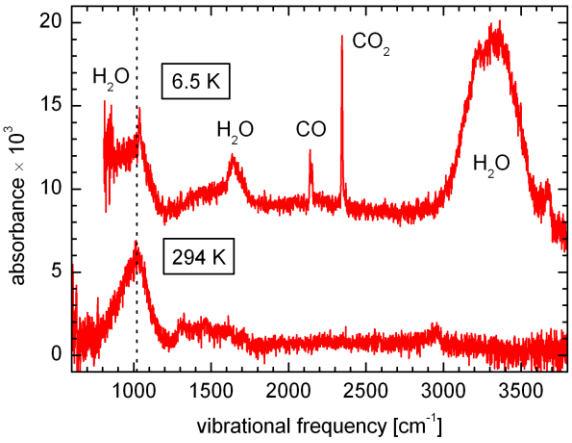

Fig. 1: *Infrared absorption spectrum of the condensate obtained in the experiment with the Mg_2SiO_4 target. The spectrum was measured at 6.5 K after evaporation of the Ne matrix and at 294 K after removal of the water ice and other impurities.*

Its position and its shape vary noticeably depending on the composition, polymerization degree, and structure of the silicate.

As expected from the IR absorption spectra, a solid condensate was found on the substrate after both experiments. The last step was the analysis of these condensates. Structural and elemental analyses were performed by high-resolution transmission electron microscopy (HRTEM) and by energy dispersive X-ray spectroscopy (EDX). The HRTEM micrographs showed micrometer-sized fluffy aggregates of grains which had a diameter of 5 to 10 nm (Fig. 2). The material of the grains appeared to be amorphous and homogeneous in structure. The elemental compositions determined by EDX were $MgSiO_{2.8}$ and $Mg_{0.3}Fe_{0.9}SiO_{3.6}$ for the condensates obtained with the Mg_2SiO_4 and $Mg_{0.4}Fe_{0.6}SiO_3$ targets, respectively.

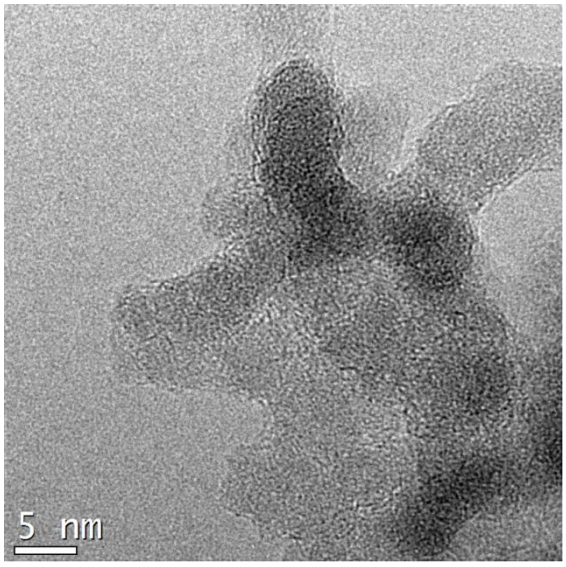

Fig. 2: *HRTEM micrograph showing the nanometer-sized grains that compose the $Mg_{0.3}Fe_{0.9}SiO_{3.6}$ condensate. The structure of the material appears to be amorphous.*

Finally, we compared the IR absorption spectra of the silicate grains synthesized in our experiments with that of interstellar silicates [3] (Fig. 3). We found that the spectrum of the synthetic amorphous Mg silicate matched the spectrum of the interstellar grains. This result is in agreement with the conclusions of previous experimental and theoretical studies on silicates [4, 5].

Thus we demonstrated for the first time the formation of solid silicate materials at temperatures relevant to the ISM and we showed that their spectrum can be favorably compared with that of interstellar grains. Our study supports the hypothesis that silicate grains can grow in the ISM.

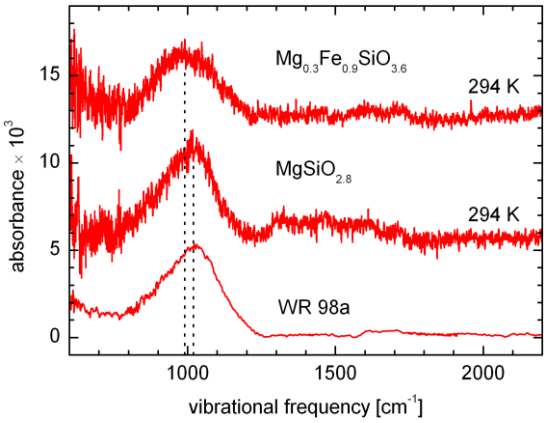

Fig. 3: *Comparison of the IR absorption spectra of the synthetic amorphous silicates with the absorption spectrum of interstellar silicates observed against the WR 98a star.*

References

[1] B.T. Draine, in Cosmic Dust – Near and Far, ASP Conf. Ser. **414**, 453-472 (2009).

[2] G. Rouillé *et al.*, Faraday Discuss. **168**, 449-460 (2014).

[3] J.E. Chiar & A.G.G.M. Tielens, Astrophys. J. **637**, 774-785 (2006).

[4] F. Kemper *et al.*, Astrophys. J. **609**, 826-837 (2004); Astrophys. J. **633**, 534 (2005).

[5] M. Min *et al.*, Astronom. Astrophys., **462**, 667-676 (2007).